

## ABSTRACT

### INCOHERENT SCATTER STUDY OF DYNAMICS IN THE IONOSPHERE E- AND F-REGION AT ARECIBO

by Yun Gong

This thesis reports the investigation of the dynamics and associated phenomena occurring in the ionospheric E- and F-region heights above Arecibo. The observational data was derived with an incoherent scatter radar (ISR) from Arecibo Observatory, Puerto Rico. The thesis focuses primarily on two aspects. One is to study the atmospheric tidal and planetary waves. This is the first time that dual-beam ISR has been used for E- and F-region tidal and planetary wave studies. The vertical structures of the observed tidal and planetary waves are analyzed rigorously. This study is the first to report the existence and possible excitation mechanism of a terdiurnal tide in the F-region at low latitude. The second aspect is to give a more complete explanation of the midnight collapse phenomenon. The F-region electric field, ambipolar diffusion, and tidal components in the meridional wind all play a role in causing the midnight collapse at Arecibo.

INCOHERENT SCATTER STUDY OF DYNAMICS IN THE IONOSPHERE E- AND  
F-REGION AT ARECIBO

A Thesis

Submitted to the  
Faculty of Miami University  
in partial fulfilment of  
the requirements for the degree of  
Master of Science in Computational Science and Engineering  
Department of Electrical and Computer Engineering

by

Yun Gong

Miami University

Oxford, Ohio

2012

Advisor \_\_\_\_\_  
Qihou Zhou

Reader \_\_\_\_\_  
Jade Y. Morton

Reader \_\_\_\_\_  
Dmitriy Garmatyuk

# TABLE OF CONTENTS

LIST OF TABLES .....	v
LIST OF FIGURES .....	vi
ACKNOWLEDGEMENTS .....	ix
CHAPTER 1 INTRODUCTION .....	1
1.1 Introduction of the Ionosphere .....	1
1.1.1 Vertical Structure of the Ionosphere .....	1
1.1.2 Wind Shear Theory and Ion Motion .....	4
1.1.3 The Ionosphere Measurement Techniques .....	8
1.2 Introduction of Incoherent Scatter Radar .....	9
1.2.1 ISR Equation and Cross Section .....	10
1.2.2 ISR Power Spectrum .....	13
1.2.3 Arecibo ISR .....	15
1.2.4 ISRs in United States .....	17
1.3 Organization of the Thesis .....	20
CHAPTER 2 INCOHERENT SCATTER RADAR DATA ANALYSIS .....	22
2.1 Derivation of Vector Velocity .....	22
2.2 Derivation of Neutral Winds .....	27
2.2.1 Derivation of E-Region Neutral Winds .....	28
2.2.2 Derivation of F-region Meridional Wind .....	30
2.3. Constrained Fitting .....	32

CHAPTER 3	ANALYSIS OF LOWER-FREQUENCY TIDAL AND QUASI-2 DAY PLANETARY WAVES AT ARECIBO .....	35
3.1	Introduction of Tidal Waves .....	35
3.2	Power Spectral Density Analysis .....	37
3.2.1	Periodograms of F-region Meridional Wind.....	38
3.2.2	Periodograms of E-region Neutral Winds.....	40
3.3	Results and Discussion of Diurnal Tide.....	43
3.4	Results and Discussion of Semidiurnal Tide.....	48
3.5	Introduction of Planetary Waves.....	54
3.6	Results of Quasi-2 Day Planetary Wave .....	55
3.7	Summary and Conclusion .....	56
CHAPTER 4	ANALYSIS OF HIGHER-FREQUENCY TIDAL WAVES AT ARECIBO .....	58
4.1	Introduction of Terdiurnal Tide.....	58
4.2	Results and Discussion of Terdiurnal Tide .....	59
4.3	Summary and Conclusion .....	66
4.4	Results and Discussion of 6-hour Tide .....	67
CHAPTER 5	MIDNIGHT IONOSPHERE COLLAPSE AT ARECIBO AND ITS RELATIONSHIP TO THE NEUTRAL WIND, ELECTRIC FIELD, AND AMBIPOLAR DIFFUSION .....	70
5.1	Introduction .....	70
5.2	Data Presentation.....	71
5.2.1	Electron Density Distribution at Arecibo .....	71
5.2.2	HmF2, NmF2 and $V_z$ .....	74
5.2.3	Components of Vertical Motion .....	77
5.3	Discussion .....	80

5.3.1	What mechanism is most responsible for the midnight collapse? .....	80
5.3.2	Which tidal components are most important for midnight collapse? .....	81
5.3.3	Considerations from other periods.....	84
5.4	Summary and Conclusion .....	87
CHAPTER 6 CONCLUSIONS AND FUTURE STUDIES.....		89
6.1	Conclusions .....	89
6.2	Future Studies.....	91
BIBLIOGRAPHY .....		93

## LIST OF TABLES

1.1	Location of United States ISR facilities.....	18
1.2	Primary parameters of United States ISR facilities .....	19
3.1	Simultaneously fitted oscillation modes in the E- and F-regions, and different neutral wind components.....	43
5.1	Amplitude and phase results of 24-, 12-, and 6-hour components in the meridional wind during Jan. 14-18, 2010, and 24-, 12-, and 8-hour components during Jan. 18-23, 2010 at 268 km, respectively.....	82

# LIST OF FIGURES

1.1	Electron concentration profile derived by the Arecibo ISR at 12:00 LT December 4, 2002 (solid line), and at 00:00 LT December 5, 2002 (dashed line). .....	2
1.2	Electron density profile derived by Arecibo ISR during 12:03 LT December 3, to 12:00 LT December 5, 2002. ....	4
1.3	Altitude distribution of the ratio of ion-neutral collision frequency to the ion gyrofrequency at E-region heights.....	6
1.4	Schematic ISR spectrum, $f_T$ represents transmitter frequency, $\Delta f$ is the width of the spectrum, and $f_0$ is the mean Doppler shift. ....	13
1.5	An aerial view of the Arecibo ISR system ( <a href="http://www.naic.edu/public/about/photos/hires/ao001.jpg">http://www.naic.edu/public/about/photos/hires/ao001.jpg</a> ). ....	16
2.1	(a) Ratios of amplitude of $V_i(\lambda_s)$ to amplitude of $V_i$ at eastward component; (b) results of RMS at eastward component. ....	25
2.2	Same as Figure 2.1 except for the southward component. ....	27
2.3	(a) Eastward neutral wind and (b) Southward neutral wind in the geographic coordinate at E-region derived from the Arecibo ISR in the period of 12 LT Jan. 19 to 12 LT Jan. 21, 2010. ....	30
2.4	Southward neutral wind in the geomagnetic coordinate at F-region heights derived from the Arecibo ISR in the period of 12 LT Jan. 19 to 12 LT Jan. 21, 2010. ....	32
2.5	Least square fitting result (blue line) and constrained fitting result (red line) for constructed data (green circles). ....	33
3.1	Periodogram of the meridional wind during Jan. 14-23, 2010. ....	38
3.2	Periodogram of the F-region meridional wind during (top) 16 LT Jan. 14 to 07 LT Jan. 18, (bottom) 09 LT Jan. 18 to 11 LT Jan. 23, 2010.....	39
3.3	Periodogram of the E-region (top) meridional wind, (bottom) zonal wind during Jan. 14-23, 2010.....	40
3.4	Periodogram of the E-region (top) meridional wind, (bottom) zonal wind during 16 LT Jan. 14 to 07 LT Jan. 18, 2010.....	41
3.5	Same as Figure 3.4 except in the period of 09 LT Jan. 18 to 11 LT Jan. 23, 2010. .	42
3.6	(a) Amplitude, and (b) phase results of the 24-hour component for the F-region meridional wind. The red curve is the least square fitting result using 4 days' data from January 14-18, 2010. The blue curve is the average by breaking the Jan. 14-18 period into two subintervals. ....	44

3.7	(a) Amplitude, and (b) phase results of 24-hour component for the F-region meridional wind. The red curve is the least square fitting result using 5 days' data from January 18-23, 2010. The blue curve is the average by breaking the Jan. 18-23, 2010 period into three subintervals.....	45
3.8	Amplitude and phase results of 24-hour component for the E-region meridional wind during January 14-18, 2010 (a, b), and January 18-23, 2010 (c, d).....	46
3.9	Same as Figure 3.8 except for zonal component. ....	48
3.10	Same as Figure 3.6 except for semidiurnal component. ....	49
3.11	Same as Figure 3.7 except for semidiurnal component. ....	50
3.12	Same as Figure 3.8 except for semidiurnal component. ....	52
3.13	Same as Figure 3.9 except for semidiurnal component. ....	53
3.14	Same as Figure 3.6 except for quasi-2 day component. ....	56
4.1	Same as Figure 3.6 except for E-region terdiurnal tide. ....	59
4.2	Same as Figure 3.9 except for terdiurnal component. ....	61
4.3	Same as Figure 3.7 except for terdiurnal tide. ....	62
4.4	Phase and amplitude variations of terdiurnal, semidiurnal, and diurnal tide at 268 km as a function of time. The terdiurnal, semidiurnal, and diurnal tide are represented by a solid, a dashed, and a dash-dot line, respectively. The line with square symbols in represents the mean wind averaged from 185 to 233 km. Zero degree in phase corresponds to maximum southward wind occurring at 0:00 LT. ....	63
4.5	Same as Figure 3.6 except for the 6-hour component. ....	67
4.6	Phase and amplitude variations of 6-hour oscillation at 196 km as a function of time. Zero degree in phase corresponds to maximum southward wind occurring at 0:00 LT. ....	68
5.1	Arecibo height-and-time electron density distribution during 16:30 LT Jan. 14 to 11:10 LT Jan. 23, 2010. The top plot shows the $K_p$ index variation as a function of time.....	72
5.2	Arecibo height-time variation of plasma frequency (MHz) averaged within the 24-hour window, (a) four days from 16:30 LT Jan. 14 to 7:23 LT Jan. 18, 2010; (b) five days from 9:55 LT Jan. 18 to 11:10 LT Jan. 23, 2010. (The radar was not operational during 7:23-9:55 LT on Jan. 18). ....	73
5.3	Vertical ion drift at 268 km (red dots), HmF2 (blue dots), NmF2 (green dots) derived from the Arecibo dual-beam ISR during 16:30 LT Jan. 14 to 11:10 LT Jan. 23, 2010. In order to better examine the nighttime part, only local time ranging from 20:00 LT to 8:00 LT next day is presented. Solid black lines serve as demarcation of different nights. For electron density,	

	the scale of 100-200 km on the altitude axis corresponds to $0 - 5 \times 10^{11}$ electrons/m <sup>3</sup> . .....	74
5.4	Average HmF2 (a), NmF2 (b) and VzF2 (c) for the nights of Jan. 14-17 (blue) and Jan. 18-22 (red). The error bars are the day-to-day variation during the averaging period. ....	76
5.5	Average $V_{z\_us}$ (a), $V_{z\_pn}$ (b) and $V_{z\_d}$ (c) for the nights of Jan. 14-17 (blue) and Jan. 18-22 (red). All the component vertical velocities are presented at HmF2 altitudes. ....	79
5.6	(a) Constructed meridional winds at 268 km during 16:00 LT Jan. 16 to 07:23 LT Jan. 18, 2010, use dc, 24-, 12-, and 6-hour components shown in red curve, dc, 24-, and 12-hour components shown in blue curve, and dc and 24-hour components shown in green curve, respectively. HmF2 is represented by black dots. (b) Same as (a) except for the period of 16:00 LT Jan. 18 to 8:00 LT Jan. 20, 2010, and using 8-hour instead of 6-hour component. ....	83
5.7	(a) Same as Figure 5.3 except for the period of 12:00 LT Dec. 3 to 12:00 LT Dec. 5, 2002, and vertical ion drift is at an altitude of 293 km. (b) NmF2 during 12:00 LT Dec. 3 to 12:00 LT Dec. 5, 2002. ....	85
5.8	Ion vertical drift contributed from perpendicular northward ion drift (blue dots), and meridional wind (red dots) at 293 km in the period of 12:00 LT Dec. 3 to 12:00 LT Dec. 5, 2002. In order to better examine the nighttime part, only a local time range from 20:00 LT to next day 8:00 LT are presented. Solid black lines are served as demarcation of different nights.....	85

## ACKNOWLEDGEMENTS

This thesis would not have been possible without the guidance and help of many people. First and foremost, I would like to state my sincere gratitude to my advisor, Prof. Qihou Zhou, who brought me into studying the fascinating ionosphere, and guided me from the very beginning of this thesis. Throughout the research work, he provided me constant encouragement and supported me in various ways. His broad knowledge and scientific perspective have been and will continue to inspire and enrich my growth as a researcher and future scientist. I am profoundly indebted to him more than he knows.

I want to particularly thank Prof. Jade Morton and Dr. Dmitriy Garmatyuk, who along with Prof. Zhou comprised my thesis committee. I am grateful to Prof. Morton for her advice, encouragement, and especially for her constructive feedback which helped me improve my presentation skills. Her rigorous work ethic will always be an inspiration to me. The Morton family's hospitality will always be remembered. I am thankful to Dr. Garmatyuk for his constructive comments on this thesis. I gratefully acknowledge all my committee members for their precious time to review my thesis and participate in the defense.

My special thanks go to Prof. Shaodong Zhang for his valuable advice on my research. I have benefited greatly from every discussion with Prof. Zhang. His enthusiasm in research has been and will continue to be inspiring.

I gratefully thank Prof. Chunming Huang for her encouragement and constructive discussions. Her warmth and hospitality will always be cherished. I am also thankful to Dr. Xianchang Yue for his advice.

Many thanks go to Mr. Lyndon Pearson and Mr. Julio Santana III. I am grateful for their time to proofread my thesis and their constructive comments on my thesis. I would also like to thank my office mates, Mr. Travis Bufler, Mr. Xiaolei Mao, Miss Jie Pan, Mr. Jason Pennington, Dr. Lei Zhang, and Mr. Zheng Ji, for their help in many ways.

It is my desire to express deep appreciation to Dr. Zhou's family for their helpfulness and hospitality during my stay in Oxford.

Words fail me to express my appreciation to my girlfriend, Miss Wenjuan Xiong, for her dedication, love, and persistent confidence in me. I also want to thank my family members for all of their support. In particular, I gratefully acknowledge my father, Mr. Chao Gong, for his unconditional love and endless support.

Finally, I would like to thank all of the other individuals who helped me in completing my thesis, and to express my sincerely apology that I could not mention each of them personally.

# CHAPTER 1

## INTRODUCTION

### 1.1 Introduction of the Ionosphere

The earth's ionosphere is an upper atmospheric region where gas atoms and molecules are partially ionized due to the solar radiation. It stretches from about 60 km to a thousand kilometers, and forms the interface between the atmosphere and the magnetosphere [Schunk and Nagy, 2000]. The ionized gas in the ionosphere significantly influences the propagation of radio waves. Radio waves can be refracted or reflected while travelling through the ionosphere [Schunk and Nagy, 2000]. This section mainly focuses on three aspects to interpret the ionosphere, which are the vertical structure of the ionosphere, the wind shear theory and ion motion, and the ionospheric measurement techniques.

#### 1.1.1 Vertical Structure of the Ionosphere

The ionosphere is horizontally stratified because of the effect of gravity, and its vertical structure can be easily illustrated by an altitude distribution of electron concentration profile. A typical electron concentration profile derived by the Arecibo incoherent scatter radar (ISR) is shown in Figure 1.1.

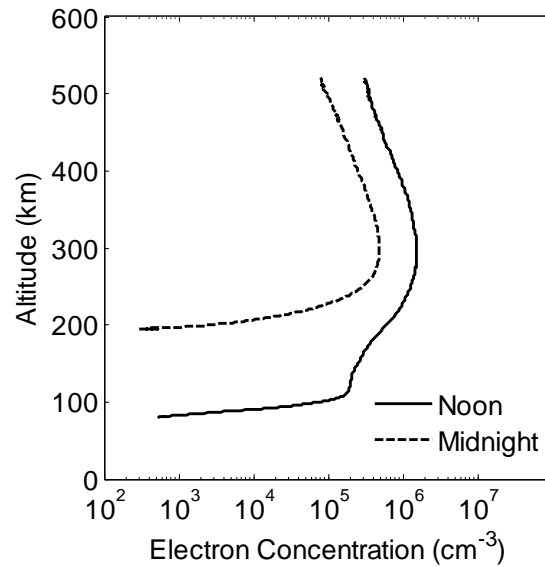


**Figure 1.1 Electron concentration profile derived by the Arecibo ISR at 12:00 LT December 4, 2002 (solid line), and at 00:00 LT December 5, 2002 (dashed line).**

As shown in Figure 1.1, two vertical distributions of electron density profiles are given, solid and dashed lines represent the vertical distribution of electron concentration at noon Dec. 4, 2002, and at midnight Dec. 5, 2002, respectively. The profiles exhibit typical vertical ionospheric structures during daytime and nighttime. The trends of electron concentration at noon and midnight are almost the same, and for both profiles, the peak intensity altitude is around 300 km. The formation of vertical ionospheric structure is due to the combined effects of the ionization and chemical recombination processes. The ionization process refers to incoming solar ultraviolet (UV) and X-ray radiations dislodging an electron from an atom or molecule, and forming an ion-electron pair. The chemical recombination is the reverse process of the ionization, which refers to chemical reactions between ions and electrons to form neutral molecules or atoms. The different chemical recombinations can be quantitatively determined by recombination rates. The recombination rate is a very important factor that restricts the peak electron density [Kelley, 2008]. Since neutral gas density decreases exponentially at higher altitudes, the strength of ionization is attenuated because of the thin gas density at higher altitudes. At the lower altitudes, on the one hand, the solar energy is attenuated as it penetrates through

the ionosphere. Chemical recombination is dominant at lower altitudes because large neutral density increases the ion-neutral collision frequency. Therefore, a large amount of ionized gas exists at the altitude range from 80 to 500 km. The difference between the two profiles in Figure 1.1 is that the electron concentration at midnight is much less than that at noon. The reason is that during the daytime, large amounts of plasma are generated in the ionosphere due to the strong solar radiation, while during the nighttime, the production of plasma is limited because of the weak ionization.

Based on the intensity of electron concentration, the main ionosphere can be vertically divided into three regions. The altitude range of 60 km to 90 km is termed the D-region. Because of the low altitudes, the ionization level at the D-region is very low, and the collision between neutral gas and plasma are intense. Hence, the electron concentration is very small. The ion composition in the D-region largely consists of  $\text{NO}^+$  and  $\text{O}_2^+$ , which are ionized by X-rays from  $\text{N}_2$  and  $\text{O}_2$ . In addition, due to effect of meteor ablation, heavy long lifetime atomic ions such as  $\text{Fe}^+$  and  $\text{Mg}^+$  are deposited at the top of the D-region.

The 90 km to 150 km above the D-region is designated as the E-region. Primary ionization processes occurring in the E-region are  $\text{O}_2$ ,  $\text{N}_2$ , and  $\text{O}$  absorbing radiations from X-rays and UV forming  $\text{O}$ ,  $\text{O}_2^+$  and  $\text{N}_2^+$ . Subsequent chemical reactions convert those ions into  $\text{NO}^+$  and  $\text{O}_2^+$ . Figure 1.2 shows time-range-electron concentration plot derived by the Arecibo ISR in the period of December 3-5, 2002. The peak intensity is around  $3 \times 10^5 \text{ cm}^{-3}$ . During the nighttime, due to lower rate of production and short lifetime of  $\text{NO}^+$  and  $\text{O}_2^+$ , the electron concentration decreases rapidly. In this scenario, the ISR cannot derive reliable data during the nighttime at E-region heights.

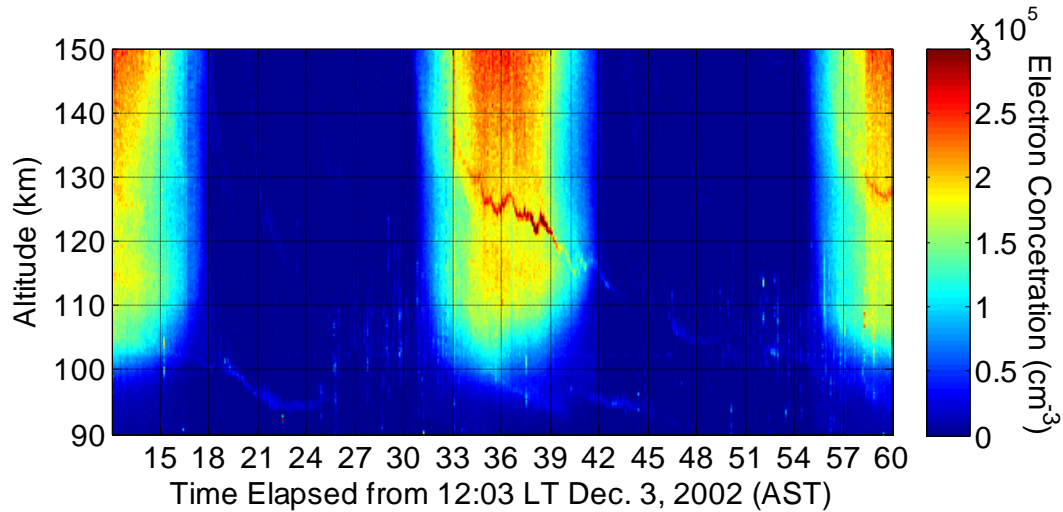


**Figure 1.2 Electron density profile derived by Arecibo ISR during 12:03 LT December 3, to 12:00 LT December 5, 2002.**

The altitude range of 150 km to 500 km is named the F-region. During daytime, the F-region is usually divided into the F1 and F2 layers. The altitude range for the F1 and F2 layers are 150 km to 210 km, and 210 km to 500 km, respectively. The F2 layer is the main area that affects the propagation of radio waves because of its higher electron concentration and whole day appearance. The electron density in the F-region varies from  $10^5$  to  $10^6$   $\text{cm}^{-3}$ . As shown in Figure 1.1, the peak density occurs at F-region, and is denoted as NmF2. An altitude where NmF2 takes place is denoted as HmF2. NmF2 and HmF2 are the two important parameters used to describe the morphology of the F-region electron concentration. The dominant ion species in the F-region is largely  $\text{O}^+$ , and its concentration is close to  $10^6$   $\text{cm}^{-3}$  at around 250 km. A detailed illustration of ion compositions in D-, E-, and F-regions are given in Figure 1.2 and Figure 1.8 of the book by Kelley [2008]. Above the F-region is termed the topside ionosphere.

### 1.1.2 Wind Shear Theory and Ion Motion

By closely examining the nighttime part shown in Figure 1.2, we can observe thin layers, which are called sporadic-E (Es) layers. The formation mechanism and the ion

concentration of the Es layer have been studied for several decades [e.g., *Whitehead*, 1961, 1989; *Macleod*, 1965; *Philbrick et al.*, 1973; *Mathews and Bekeny*, 1979; *Carter and Forbes*, 1999; *Zhou et al.*, 2005, 2008]. At present, the wind shear theory is widely regarded as an accurate and plausible explanation of Es layers. The basic theory is based on the zonal wind system driven by gravity waves or tidal components in the E-region. Due to effect of the geomagnetic field, the eastward winds push ions upward, while the westward winds blow ions downward. These vertical shears accumulate ions and form a thin layer with intense ionization [*Mathews* 1998]. The primary component in the Es layer is atomic ions of  $\text{Fe}^+$  and  $\text{Mg}^+$ , which have a long lifetime and originally come from deposition of meteor ablation [*Philbrick et al.* 1973]. *Macleod* [1965] presented an ion motion theory at E-region. This theory is based on an assumption that at each altitude the collision force and geomagnetic force acting on the ions are balanced. This theory provides a guideline of E-region ion motion, and it is essential for understanding the wind shear mechanism. The ion motion theory described below largely follows the derivation of *Macleod* [1965].

By only considering the collision, electric, and geomagnetic force on the ions, the equation of motion can be written as below [*Dungey* 1958],

$$\frac{d\mathbf{V}_+}{dt} = \nu_{in} (\mathbf{U} - \mathbf{V}_+) + \frac{e}{m_+} (\mathbf{V}_+ \times \mathbf{B}) + \frac{e}{m_+} \mathbf{E} \quad (1.1)$$

where  $e$ ,  $m_+$  are the charge and mass;  $\mathbf{V}_+$  is ion drift velocity;  $\mathbf{U}$  is neutral wind velocity;  $\nu_{in}$  is the ion-neutral collision frequency;  $\mathbf{B}$  is the local geomagnetic field, and  $\mathbf{E}$  is the local electric field. If the acceleration is very small, the above equation can be rewritten as,

$$\mathbf{V}_+ = \frac{1}{1 + \rho^2} \left[ \rho^2 \left( \mathbf{U} + \frac{e}{m_+ \nu_{in}} \mathbf{E} \right) + \rho \left( \mathbf{U} + \frac{e}{m_+ \nu_{in}} \mathbf{E} \right) \times \boldsymbol{\Gamma} + (\mathbf{U} \cdot \boldsymbol{\Gamma}) \boldsymbol{\Gamma} \right] \quad (1.2)$$

Where  $\boldsymbol{\Gamma}$  is the unit vector along  $\mathbf{B}$ ,  $\mathbf{B} = B_0 \boldsymbol{\Gamma}$ ,  $\rho$  is the ratio of ion-neutral collision frequency to the ion gyrofrequency, which is given by,

$$\rho = \frac{m_+ v_{in}}{e B_0} \quad (1.3)$$

As shown in Eq. 1.2, the ion drift has components parallel or perpendicular to the neutral wind, electric field and geomagnetic field. The ion drift is very sensitive to the  $\rho$  term. The formula to calculate the  $\rho$  term at Arecibo is given by Zhou *et al.*, 2011, as,

$$\rho = e^{\frac{Z_0 - Z}{9.4} [ 1 - 0.023(Z - Z_0) + 3 \cdot 10^{-4} (Z - Z_0)^2 + 4.3 \cdot 10^{-6} (Z - Z_0)^3 ]} \quad (1.4)$$

where  $Z_0$  is 123.7 km. Based on Eq. 1.4, the E-region altitude distribution of the ratio of collision frequency to the gyrofrequency is computed and shown in Figure 1.3.

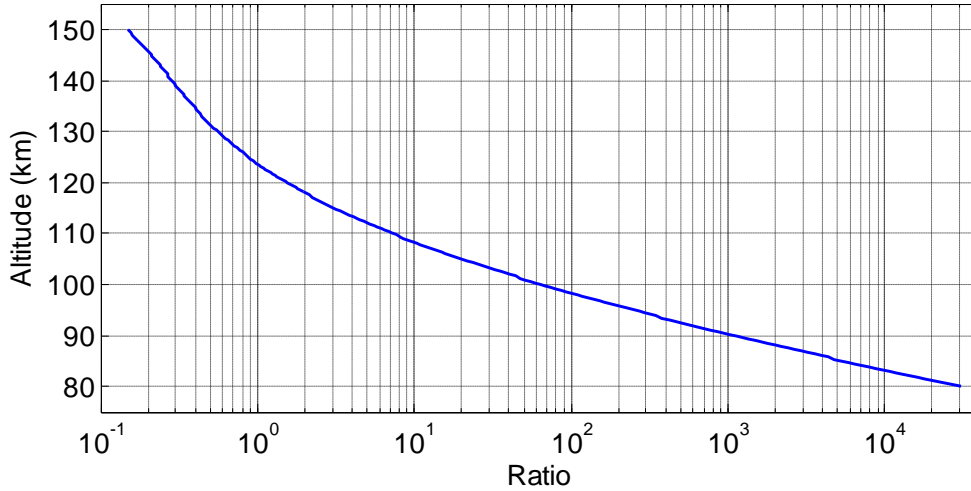


**Figure 1.3 Altitude distribution of the ratio of ion-neutral collision frequency to the ion gyrofrequency at E-region heights.**

As shown in Figure 1.3, below 95 km, where the ratio is much larger than 1, the collision force is dominant. The ions are dragged along the motion of the neutral particles. The ion drift velocity  $\mathbf{V}_+$  is approximately determined by,

$$\mathbf{V}_+ \approx \mathbf{U} + \frac{e}{m_+ v_{in}} \mathbf{E} \approx \mathbf{U} \quad (1.5)$$

Above 140 km, since the ratio is much smaller than 1, the geomagnetic force is dominant. The ions are driven by the neutral wind moving along the geomagnetic field line. The ion drift velocity is given by,

$$\mathbf{V}_+ \approx (\mathbf{U} \cdot \boldsymbol{\Gamma}) \boldsymbol{\Gamma} \quad (1.6)$$

In the altitude range of 95 to 140 km, the collision and geomagnetic force are balanced. All the three terms shown in the Eq. 1.2 contribute to the ion motion, while the second term contributes more to the ion motion than the other two. The direction of ion drift contributed from the second term is perpendicular to a plane formed by the neutral wind, the electric field, and geomagnetic field.

In order to reveal the ion motion in different directions, three orthogonal vector ion drifts are derived by decomposing Eq. 1.2 into the following equations,

$$V_s = \frac{1}{1+\rho^2} \left[ (\rho^2 + \cos^2 I) \left( U_s + \frac{e}{m_+ v_{in}} E_s \right) - \rho \sin I \left( U_e + \frac{e}{m_+ v_{in}} E_e \right) + \sin I \cos I \left( U_z + \frac{e}{m_+ v_{in}} E_z \right) \right] \quad (1.7)$$

$$V_e = \frac{1}{1+\rho^2} \left[ \rho \sin I \left( U_s + \frac{e}{m_+ v_{in}} E_s \right) + \rho^2 \left( U_e + \frac{e}{m_+ v_{in}} E_e \right) - \rho \cos I \left( U_z + \frac{e}{m_+ v_{in}} E_z \right) \right] \quad (1.8)$$

$$V_z = \frac{1}{1+\rho^2} \left[ \sin I \cos I \left( U_s + \frac{e}{m_+ v_{in}} E_s \right) + \rho \cos I \left( U_e + \frac{e}{m_+ v_{in}} E_e \right) + (\rho^2 + \sin^2 I) \left( U_z + \frac{e}{m_+ v_{in}} E_z \right) \right] \quad (1.9)$$

where  $U_s$ ,  $U_e$ , and  $U_z$  are the neutral wind velocity in southward, eastward, and vertical directions, respectively;  $E_s$ ,  $E_e$ , and  $E_z$  are the local electric field in southward, eastward, and vertical directions, respectively;  $I$  is the dip angle. Since the vertical motion of neutral wind is orders of magnitude less than the horizontal components,  $U_z$  is neglected

in this thesis. In addition, since the geomagnetic field is largely equi-potential, the electric field components have the following relation,

$$\frac{E_s}{E_z} = \frac{-\sin I}{\cos I} \quad (1.10)$$

Thus, the vertical ion drift can be rewritten as,

$$V_z = \frac{\cos I}{1 + \rho^2} \left[ U_s \sin I + \rho U_e + \frac{E_e}{B_0} + \frac{E_z}{B_0 \cos I} \right] \quad (1.11)$$

As shown in Eq. 1.11, the vertical ion motion depends on the horizontal neutral wind velocities and the electric field. Compared to the electric field, tidal and gravity waves in the neutral winds can cause larger short term variability. It is highly possible that neutral winds driven by the tidal and gravity waves control the vertical motion of ions first moving downward then upward to form a thin layer in the E-region. However, there is a necessary condition for wind shear mechanism to be effective. The average ion vertical motion should be much larger than the downward phase velocity of the waves. The detailed description of wind shear theory can be found in *Zhou* [1991] and *Mathews* [1998].

### 1.1.3 The Ionosphere Measurement Techniques

The observational investigation of the ionosphere could be traced back to almost a century ago. In 1925, *Breit and Tuve* invented the ionosonde, a device that measures the plasma frequency by vertically transmitting high frequency pulses into the ionosphere and then analyzing the received echoes. A year after the invention, they used an ionosonde to study echoes from the ionosphere [*Breit and Tuve*, 1926]. For a long time the ionosonde was the most important and fundamental device to detect the plasma frequency at E- and F-regions. Early observations of the ionosphere were based on the coherent reflection of radio waves at frequencies below 20 MHz. In the late 1950's, due to the application of new techniques, such as rocket- and satellite-borne instruments and incoherent scatter radars, understanding of the ionosphere had been greatly advanced.

The Langmuir probe which is mounted on a rocket can provide in situ measurement of the electron density, electric field, and electron temperature. The ion drift meter carried on a satellite is capable of measuring the ion radial drift velocity. In 1958, *Gordon* came up the idea of building a powerful radar to detect the weak incoherent scatter power from free electrons in the ionosphere [*Gordon* 1958]. Just after *Gordon's* publication, *Bowles* conducted the first incoherent scatter radar experiment in Peru and proved the feasibility of detecting the weak incoherent scatter power. The parameters of *Bowles'* radar system are 40.92 MHz operating frequency, 4 to 6 MW peak pulse power, and 50 to 150  $\mu$ s pulse duration [*Bowles* 1958]. From the experiment, *Bowles* successfully derived the electron concentration in the altitude range from 100 km to 800 km. Aside from electron concentration, the echo from the incoherent scatter return contains other essential information about the ionosphere, such as line-of-sight ion drift, ion temperature, and electron temperature. After the 1950's, more and more instrumented satellites have been launched for ionosphere measurements. For instance, the CHALLENGING Mini-Satellite Payload (CHAMP) launched in July, 2000, provides a 10 years' temporal variation of the geomagnetic field. In the meantime, ground-based radio detecting systems have been upgraded as well. For example, Arecibo Observatory built a dual-beam system in 2001. This new system significantly improved the capability of measuring ionospheric vector drifts. With the development of measurement techniques, the mystic veil of the ionosphere is gradually revealed.

## **1.2 Introduction of Incoherent Scatter Radar**

An incoherent scatter radar (ISR) is a radar that detects the power from plasma in the ionosphere due to random thermal fluctuations. The total scattering power in an ISR is the sum of the power from individual scatters. The return power collected from each altitude is proportional to the electron concentration. The width of ISR power spectrum is related to the thermal fluctuation. Four important ionospheric parameters, electron density, line-of-sight velocity, electron temperature, and ratio of ion temperature to electron temperature can be directly derived from the ISR power spectrum. Other useful

parameters such as electric field and neutral wind can be further deduced. ISR is one of the most powerful instruments to observe the ionosphere. In this section, the basic ISR range equation and spectrum are described. In addition, the Arecibo ISR system and other ISR facilities in the United States are reviewed.

### 1.2.1 ISR Equation and Cross Section

Radar equation provides the relationship between the received power and the transmitted power, scattering cross section, and other radar system parameters. It is a deterministic model which can be used for fundamental system design and analysis [Richards 2005]. The ISR equation and cross section shown in this section mainly follow derivations by Mathew [1986] and Zhou [1991].

Assuming the isotropic transmitted power is  $P_T$ ; the antenna power gain is  $G(\theta, \phi)$ , where  $\theta$  is measured from the beam central axis and  $\phi$  is the corresponding azimuth angle. The peak transmitted power density at range  $R$  in the far field is,

$$F_i(\theta, \phi) = \frac{P_T L G(\theta, \phi)}{4\pi R^2} \quad (1.12)$$

where  $L (\leq 1)$  is the system transmitting efficiency. When the transmitted radio wave penetrates the ionosphere, some of the power is backscattered toward the radar. Assuming the transmitted and received antenna are the same, the backscattered power density at the receiver per unit scattering volume per Hertz is,

$$F_s(\theta, \phi) = \frac{F_i(\theta, \phi) \sigma(R, \omega)}{4\pi R^2} \quad (1.13)$$

where  $\sigma(R, \omega)$  is the differential backscatter cross section at range  $R$  and frequency  $\omega$ . Let  $A_e(\theta, \phi)$  be the ratio of the power density received by an antenna to the power incident on the antenna. This ratio is termed the effective aperture, which is a fictional area that reflected the capacity of an antenna system to convert incident energy flux into power. The effective aperture is related to the antenna gain through the following equation,

$$A_e(\theta, \phi) = \frac{\lambda^2}{4\pi} G(\theta, \phi) \quad (1.14)$$

where  $\lambda$  is the radar wavelength. Thus, the backscattered power received per unit scattering volume per Hertz by an antenna is,

$$P_s(\theta, \phi, R, \omega) = \frac{P_T L \lambda^2 G^2(\theta, \phi) \sigma(R, \omega)}{64\pi^3 R^4} \quad (1.15)$$

If the effect of radio waves attenuated by the atmosphere is ignored, Eq. 1.15 represents a basic form of simple point target radar equation, where the only undetermined term is the radar cross section. In order to derive the basic form of ISR equation, the radar cross section needs further investigation.

Based on *Gordon's* hypothesis [*Gordon*, 1958], if the wavelength of transmitted radio wave is sufficiently small, signals scattered by multiple electrons due to random thermal fluctuation can be regarded as uncorrected. Thus, the total power received by the ISR is the summation of the power from individual scatters. The Doppler width in received power spectrum is related to the electrons random thermal fluctuation. However, the first experiment made by *Bowles* [1958] found that the Doppler width in the returned power spectrum is very small compared with the Doppler width calculated by *Gordon's* hypothesis. The experiment reveals that the received power is not due to the electrons random thermal fluctuation but due to the plasma random thermal fluctuation. The ions in plasma will introduce some degree of time coherence. Therefore, a frequency dependable term  $\sigma_n(\omega)$  is introduced in the cross section, and the ISR cross section is given by,

$$\sigma(R, \omega) = N_{e0}(R) 4\pi r_e^2 \sigma_n(\omega) \quad (1.16)$$

where  $N_{e0}(R)$  is the steady electron concentration at range  $R$ ;  $r_e$  is the radius of an electron;  $\sigma_n(\omega)$  is the normalized scattering coefficient per electron per Hertz.

The derivation of  $\sigma_n(\omega)$  has been studied and introduced by various authors [e.g., *Bekefi* 1966; *Farely* 1966; *Mathews* 1986; *Zhou* 1991]. In order to fulfill the condition of incoherent scatter, the radar should transmit radio waves with wavelength less than the Debye length,  $\lambda_D$ , which is given by,

$$\lambda_D = 69m_e \sqrt{\frac{T_e}{N_e}} \quad (1.17)$$

where  $m_e$ ,  $T_e$ , and  $N_e$  are the electron mass, temperature, and concentration, respectively. However, if the probing wavelength is less than the Debye length, the received power spectrum would be too wide. The energy in each sampled frequency is hard to be detected by present radar systems. Therefore, the ISR is not performing a purely incoherent scattering detection. Although the scattering pattern of the plasma in the ionosphere is complicated, the total scattering cross section is derived, and given by [Buneman 1962; Farely 1966],

$$\sigma_n = \frac{\alpha_e^2}{1 + \alpha_e^2} + \frac{1}{(1 + \alpha_e^2)(1 + \frac{T_e}{T_i} + \alpha_e^2)} \quad (1.18)$$

where  $\alpha_e^2 = \frac{4\pi\lambda_D}{\lambda}$  (1.19)

This expression has ignored the negative ions in the plasma. The accuracy of this formula is very good when  $1 \leq T_e/T_i \leq 3$ .

Assuming the differential volume of  $0.5c\tau R^2 \sin\theta d\theta d\phi$  is illuminated by the radar beam with  $\tau$  the pulse length and  $c$  the speed of light, the received backscatter power per Hertz is given by,

$$P_s(R, \omega) = \frac{P_T L N_e(R) \sigma_n(R, \omega) c \tau \lambda^2 r_e^2}{16\pi R^2} \int_0^\pi G^2(\theta) \sin\theta d\theta \quad (1.20)$$

By assuming of azimuth symmetry for  $G(\theta, \phi)$  while performing the integration, the above equation is expressed as,

$$P_s(R, \omega) = \frac{K_{sys} P_T N_e(R) \sigma_n(R, \omega)}{R^2} \quad (1.21)$$

where  $K_{sys} = \frac{Lc\tau\lambda^2 r_e^2}{16\pi} \int_0^\pi G^2(\theta) \sin\theta d\theta$  (1.22)

is a radar system constant. Eq. 1.21 exhibits the basic expression of the ISR range equation. As shown in Eq. 1.21, the received power is proportional to the radar cross section, and electron concentration. Unlike the point target equation shown in Eq. 1.15, the power collected by an ISR is inversely proportional to  $R^2$ . The reason is that plasma in the ionosphere is a volume filled scatterer. At any one instant, a radar resolution cell increases as  $R^2$ .

### 1.2.2 ISR Power Spectrum

Although the ISR can only measure the power spectrum, the incoherent scatter spectrum contains the most essential information about the ionosphere, such as electron density, line-of-sight ion drifts, ion temperature, and electron temperature. A schematic ISR spectrum free from noise is shown in Figure 1.4. The horizontal axis represents frequencies and the vertical axis represents power.

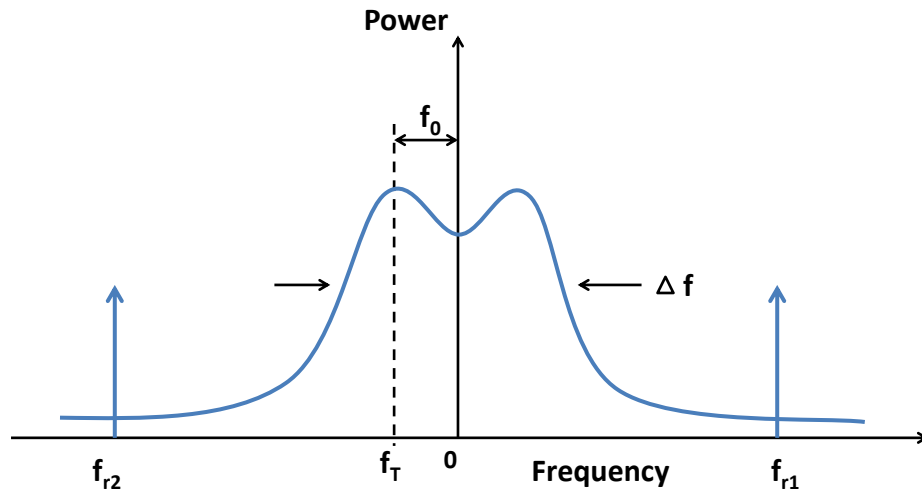


**Figure 1.4 Schematic ISR spectrum,  $f_T$  represents transmitter frequency,  $\Delta f$  is the width of the spectrum, and  $f_0$  is the mean Doppler shift.**

As shown in Figure 1.4, the power spectrum contains two parts. One is the spectrum centered at middle, which is referred to as ion line. The shape of the ion line is determined by various ionospheric parameters, such as a ratio of electron temperature to ion temperature, ion drift velocity, and ion composition. The area underneath the ion line spectrum represents the total power, which is proportional to the plasma density. A shift between the center of the spectrum and the transmitter frequency indicated as  $f_0$  in Figure 1.4 is the mean Doppler shift, which provides the line-of-sight collective motion of the plasma. The width of the spectrum denoted as  $\Delta f$  in Figure 1.4 is a reflection of the ion temperature.

The other part of the spectrum is located very close to the plasma frequency and is termed as plasma line. Since the essential information of the plasma line is only contained at the location of peak resonance frequencies, not in the shape of power spectrum, two vertical lines instead of the shape of spectrum are shown in Figure 1.5 to represent the plasma line. In Figure 1.5,  $f_{r1}$  and  $f_{r2}$  represent the up- and down-shifted plasma line, respectively. The relation between plasma resonance frequency and the plasma frequency is derived by [Yngvesson and Perkins, 1968], and it given by,

$$f_r^2 = f_p^2 + \frac{12k_b T_e}{\lambda^2 m_e} + f_c^2 \sin^2 \alpha \quad (1.23)$$

where

$$f_c = \frac{1}{2\pi} \frac{eB_0}{m_e c} \quad (1.24)$$

$f_c$  is the electron gyrofrequency;  $f_r$ , and  $f_p$  are the resonance frequency, and plasma frequency, respectively;  $k_b$  is the Boltzmann constant;  $\alpha$  is the angle between radar beam and the magnetic field line. Eq. 1.23 manifests that the plasma frequency is a function of resonance frequency, electron temperature, and the magnetic field.

The plasma frequency and the electron concentration have a good approximate relationship, which is given by,

$$f_p \approx 9000 \sqrt{N_e} \quad (1.25)$$

where the unit for  $f_p$ , and  $N_e$  is in Hertz, and reciprocal cubic centimeters, respectively. Thus, if the electron temperature is known, the electron concentration can be derived from the plasma line as well. As a matter of fact, from the experimental ISR power spectrum, the electron concentration derived from plasma line is more accurate than that obtained from ion line. The reason is that the stochastic variation in the spectrum makes accurate determination of electron density very difficult, while location of the peak resonance frequency in the plasma line is deterministic.

In the ISR power spectrum, the locations of up- and down-shifted plasma resonance frequencies are not perfectly symmetric. It has been revealed that this subtle asymmetry is dependent on the electron temperature, currents, photoelectrons and other possible effects by various authors [*Bauer et al.*, 1976; *Showen*, 1979; *Hagfors and Lehtinen*, 1981; *Behnke and Ganguly*, 1986]. The difference of that asymmetry is hard to measure, because it requires high frequency resolution. *Nicolls et al.* [2006] presented the first derivation of high resolution electron temperature using the asymmetry of two resonant frequencies at Arecibo. Aside from the location of the resonant frequencies, the corresponding power intensity of the resonant frequencies also provides useful information, such as the concentration of photoelectrons.

In summary, by performing a nonlinear fitting to the ion line spectrum, various ionospheric parameters including: line-of-sight ion drift, electron density, ion temperature, electron temperature, and ion-neutral collision frequency can be obtained [*Zhou et al.*, 1997b]. The plasma line can provide more accurate electron concentration and electron temperature information. Additional atmospheric and ionospheric parameters, such as the electric field, and neutral wind velocity can be derived indirectly.

### **1.2.3 Arecibo ISR**

In 1958, the same year *Gordon* published his initial idea on incoherent scattering, he successfully secured funding to build a very powerful ISR at Arecibo (18 °N, 67 °W), Puerto Rico, where the natural Karst terrain with large limestone sinkholes provides a

perfect spot for the world's largest single-dish radio telescope with a diameter of 305 meters. An aerial view of the Arecibo ISR system is shown in Figure 1.5.



**Figure 1.5 An aerial view of the Arecibo ISR system**  
(<http://www.naic.edu/public/about/photos/hires/ao001.jpg>).

Three giant pillars hang the waveguide, transmitting and receiving electronics, and the servo-system in the sky. The antenna is a spherical reflector and the effective antenna aperture is  $41.7 \text{ dB/m}^2$ . The peak power of the Arecibo ISR system is 2.5 MW, and it operates at 430 MHz frequency. Since its operation in 1963, the Arecibo ISR has been the most powerful radar in the world. In 1974, Arecibo became a national center and opened its door to scientists pursuing radio astronomy, radar astronomy as well as space science on a competitive basis.

The purpose of using ISR in this thesis is to derive the ionospheric parameters such as ion drifts and electron concentration. Since the radar can only derive the radial velocity in the radar beam direction, the radar beam has to sweep 90 or 360 degrees during the observation to obtain the radial velocities in different directions. Then, three

orthogonal vector velocities can be derived from those line-of-sight velocities either through nonlinear least square fittings or other methods. A detailed conversion method is described in Chapter 2. The height resolution is very crucial if the dynamics to be studied have small scale vertical variation. However, the pulse duration has to be large enough so that the transmitted power can detect the weak incoherent scattering of electrons. The Arecibo ISR usually transmits signals with 52  $\mu$ s pulse packet duration to obtain electron concentration. If the transmitted pulse with duration of 52  $\mu$ s is uncoded, the range resolution corresponding to that pulse is 7.8 km. Such height resolution is insufficient for studying tidal and planetary waves at E-region. In order to have better range resolution, the transmitted pulses are encoded with the Barker coding technique [Ioannidies and Farley, 1972]. The Barker codes are one of the most important biphasic codes in radar technique. The characteristic of the barker codes is that the side-lobes of auto-correlation function at non-zero lags contain values of +1 and -1 only. At present, there are only eight barker codes, and the largest length of barker code is 13. In 1972, Ioannidies and Farley reported that they achieved a height resolution of 900 m while maintaining the same power as the uncoded long pulse. In 1986, Sulzer presented a coded long-pulse technique which improved height resolution to 300 m. The raw range resolution of Arecibo dual-beam ISR data used in this thesis is 300 m. For specific Arecibo ISR data taking procedures please refer to Sulzer [1988], and Zhou [1991].

#### **1.2.4 ISRs in United States**

ISR is a very important and powerful instrument which is capable of measuring many fundamental atmospheric and ionospheric parameters. Aside from study of the ionosphere, ISR can also be applied to astronomy study. There are five ISR facilities supported by the United States, and their locations, and primary radar parameters are listed in Table 1.1, and Table 1.2, respectively.

**Table 1.1 Location of United States ISR facilities**

Facility	Affiliation	Location	Latitude	Longitude
Jicamarca Radar Observatory	Cornell University	Lima, Peru	11.95 °S	76.87 °W
Arecibo Observatory	Stanford Research Institute International	Arecibo, Puerto Rico	18.3 °N	66.8 °W
Millstone Hill Observatory	Massachusetts Institute of Technology	Westford, Mass., U. S.	42.6 °N	71.5 °W
The Sondrestrom Research Facilities	Stanford Research Institute International, Denmark's Meteorological Institute	Sondrestrom, Greenland	67 °N	51 °W
Advanced Modular Incoherent Scatter Radar (AMISR)	Stanford Research Institute International	Poker Flat, Alaska, U. S.	65 °N	147 °W
		Resolute Bay, Nunavut, Canada	74 °N	94 °W

**Table 1.2 Primary parameters of United States ISR facilities**

Facility	Antenna	Operating Frequency (MHz)	Peak Power (MW)
Jicamarca Radar Observatory	Array of 18432 dipole elements	49.92	4
Arecibo Observatory	305 m spherical reflector	430	2.5
Millstone Hill Observatory	68 m parabola	440	2.5
	48 m parabola		
The Sondrestrom Research Facilities	32 m fully steerable	1290	3.5
AMISR	128 block-like panels	430 - 450	2

As seen from Table 1.1, only Jicamarca Radar Observatory is located in the Southern Hemisphere, and the other ISR facilities are scattered at the low, middle, or high latitudes in the Northern Hemisphere. ISR facilities located at different latitudes form a network and provide a more complete picture of the upper atmosphere. In 1958, the Defense Advanced Research Project Office began construction of the Arecibo ISR. As shown in Table 1.2, the Arecibo and Jicamarca ISR have the largest collecting area. The Arecibo ISR is most sensitive radar in the world because of the combination of operating wavelength, effective aperture and transmitter power. Among those five ISR facilities, Arecibo Observatory is the only one that is capable of performing plasma line studies. In 1961, the second ISR facility, Jicamarca Observatory was constructed by the National Bureau of Standards near Lima, Peru. Due to the unique equatorial geometry,

the radar beam can point perpendicular to the magnetic field. By configuring radar beam this way, the Jicamarca ISR has ability to derive very accurate line-of-sight drift velocities with the error within the order of 0.5 m/s. In 1963, the Millstone Hill zenith antenna was built up by Lincoln Laboratories, Massachusetts Institute of Technology, at a site near Boston, MA. In 1971, the Chatanika radar moved from Stanford University to a new location near Fairbanks, Alaska, and eleven years later, it moved again and has operated till now at Sondrestrom, Greenland. The AMISR facility is the newest ISR facility, which is constructed in 2004, and consists of three radar faces. Construction of the first two radar faces at Poker Flat, Alaska, United State, and Resolute Bay, Nunavut, Canada, are complete and the radars has been in operation since March of 2007, and August of 2009, respectively. Location of the third radar face has not been determined yet. The AMISR radar system is the first phased-array, solid-state, and reconfigurable ISR.

In the future, we believe the cost of constructing and maintaining ISRs will be reduced so that more ISRs will be built. These radars will provide even longer observational time. The large amounts of data collected from ISRs at different sites enable us to study the characteristics of the ionosphere at different longitudes, latitudes, and seasons. As the number of ISRs continues to grow, we will have a better and better understanding of the ionosphere.

### **1.3 Organization of the Thesis**

The purpose of this thesis is to study the dynamics at E- and F-region heights above Arecibo, using observational data obtained from the Arecibo dual-beam ISR during Jan. 14-23, 2010 and Dec. 3-5, 2002. The dynamics studied in this thesis are mainly related to tidal and planetary waves and nighttime vertical F-layer motion. Brief introductions of the earth's ionosphere and the ISR system are presented in the above sections. Chapter 2 mainly discusses the data processing methods used in this thesis. It describes the derivation of essential ionospheric and atmospheric parameters from the line-of-sight velocities, ion and electron temperature, and electron concentration directly measured by the Arecibo ISR. Additionally, a description of constrained fitting method is

presented in Chapter 2. Due to lack of ionization in the E-region during nighttime, ISR cannot derive reliable data. The constrained fitting method is designed to relieve the nocturnal data gap problem. In Chapter 3, diurnal and semidiurnal tides, and quasi-2 day planetary wave are analyzed in the altitude range from 90 km to 350 km above Arecibo. The short term variabilities of tidal and planetary waves are examined. The vertical structures of those waves are studied. The core parts of this thesis are Chapters 4 and 5. Chapter 4 presents an analysis of terdiurnal and quad-diurnal tides observed in the F-region at low latitude. This is the first time short-period tides have been studied in F-region heights at low latitude. The most significant conclusion drawn from the analysis is that the F-region terdiurnal tide is not likely excited by nonlinear interaction between lower-frequency tides or diurnal tide and gravity waves. Chapter 5 reports a prominent phenomenon, a rapid drop of F-layer peak height around midnight (midnight collapse) observed at Arecibo, and investigates its relationship to the neutral wind, electric field, and ambipolar diffusion. The investigation shows that the process of the midnight collapse consists of three stages, which are preconditioning, initial descent and sustained descent. The neutral wind, electric field, and ambipolar diffusion all play an important role in the process of midnight collapse. Conclusions of the thesis and future studies are summarized in Chapter 6.

## CHAPTER 2

# INCOHERENT SCATTER RADAR DATA ANALYSIS

In this thesis, two periods of dual-beam ISR data have been used to study the dynamics occurring in the ionosphere above Arecibo. In the first period, the observation was carried out from 16:30 LT Jan. 14 to 11:10 LT Jan. 23, 2010 using the dual-beam ISR at the Arecibo Observatory, Puerto Rico (18.3 °N, 66.7 °W). For this experiment, the Linefeed was pointing at zenith continuously, while the Gregorian feed rotated in the azimuth direction at a fixed 15 degrees zenith angle during the observation. In the second period, the experiment was conducted during 12:03 LT Dec. 3 to 12:00 LT Dec. 5, 2002. In this experiment, the Linefeed and Gregorian feed were both pointed at a 15 degrees zenith angle, and rotated continuously during the observation. Directly measured ionospheric parameters relevant to the present study include: line-of-sight (LOS) velocity, ion and electron temperature, and electron density. A detailed description of the ISR measurement technique is found in *Zhou et al.* [1997b] and *Zhou and Sulzer* [1997c]. In order to study the dynamics, the derivation of vector drifts and neutral winds are necessary. This chapter describes the derivation of the three orthogonal vector ion drifts and the neutral winds at E- and F-region heights.

### 2.1 Derivation of Vector Velocity

An ISR can achieve fine time and height resolution in the LOS direction. However, we are more interested in the velocities in three orthogonal directions other than the radial directions directly provided by an ISR. A technique developed by *Hagfors and Behnke* [1974] could transform the LOS velocity to vector velocity, based on the assumption of a constant vector field in every full cycle of rotation, typically in 15 minutes. This assumption may not adequately represent the variations in the vector velocities. More recently, *Sulzer et al.* [2005] described a linear regularization technique to improve the time resolution of the derived vector velocity. This method relaxed the old

method's restrictive assumption. The only assumption needed is that vector velocities vary linearly between time steps. The linear regularization method shown in this section largely follows derivations by *Press et al.* [1992] and *Sulzer et al.* [2005].

Each LOS measurement can be transformed to a set of three orthogonal components in matrix form described below,

$$\begin{bmatrix} V_{LOS}^{(1)} \\ V_{LOS}^{(2)} \end{bmatrix} = \begin{bmatrix} -\cos \varphi \sin \theta^{(1)} & \sin \varphi \cos \theta^{(1)} & \cos \theta^{(1)} \\ -\cos \varphi \sin \theta^{(2)} & \sin \varphi \cos \theta^{(2)} & \cos \theta^{(2)} \end{bmatrix} \begin{bmatrix} V_x \\ V_y \\ V_z \end{bmatrix} \quad (2.1)$$

where,  $\theta$  is the zenith angle,  $\varphi$  is the azimuth,  $V_{LOS}$  is LOS velocity, superscript  $^{(1)}$ , and  $^{(2)}$  represent two radar beams, and  $[V_x \ V_y \ V_z]^T$  are the unknown vector components in the south, east, and upward directions, respectively.

The above equation can be notated as  $b = A \cdot V$ . Eq. 2.1 can be solved by using least square fitting method. However, the solution is not unique, because matrix  $A$  has fewer rows than columns. The linear regularization method can make the solution unique by adding extra information. The extra information applied in this thesis is an assumption that the variation of vector drifts between time steps is smooth. An additional matrix enters into the Eq. 2.1 based on the assumption.

The new equation can be rewritten as,

$$(A^T A + \lambda_s H) V = A^T b \quad (2.2)$$

where,  $\lambda_s$  is a smooth parameter. Matrix  $H$  used here is given by *Sulzer et al.* [2005]. Detailed description of matrix  $H$  is found at *Press et al.* [1992] and *Sulzer et al.* [2005].

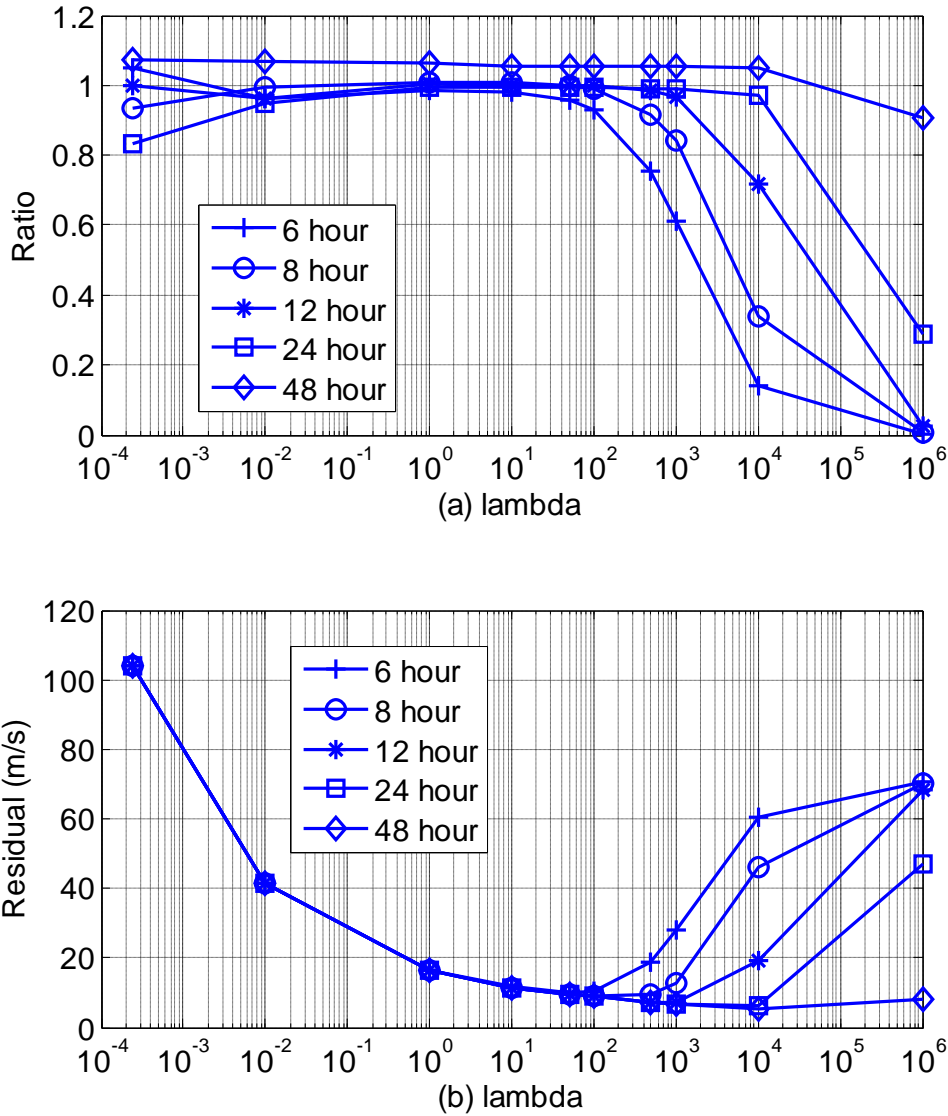
Unlike the matrix  $H$ , information about how to choose an appropriate value of  $\lambda_s$  is limited. *Press et al.* [1992] only provides a suitable starting guess formula which is shown below,

$$\lambda_s = \text{Tr}(A^T A) / \text{Tr}(H) \quad (2.3)$$

where  $Tr$  represents the trace of a matrix. *Sulzer et al.* [2005] performed a simulation to derive a reasonable  $\lambda_s$  in a more general way. In this thesis, one of aims is to investigate tidal and planetary waves. The linear regularization method should not influence the raw information of tidal and planetary waves that lie in the line-of-sight velocities. Based on the goal of the thesis, we largely adopted the simulation scheme reported by *Sulzer et al.* [2005] to obtain a reasonable value of  $\lambda_s$ . The procedures of the simulation are described in the following. Firstly, three orthogonal vector velocities are generated ( $V_i$ ). For each orthogonal component, five sets of the velocities are synthesized by using one harmonic component with the typical tidal and planetary wave's periods of 6-, 8-, 12-, 24-, or 48-hour, respectively. (Detailed introduction of tidal and planetary waves are described in Chapter 3.) Then, these vector velocities are transformed to LOS velocities under the same condition as the observational ISR data. That is, the radar beam rotates continuously and accomplishes a full cycle every 15 minutes while the beam points 15 degrees off zenith. Additionally, random noise is added into the LOS velocities to make synthesized data more realistic. Then, these constructed LOS velocities are converted to three orthogonal vector velocities ( $V_i(\lambda_s)$ ) by applying the linear regularization method. Since the results are dependent on  $\lambda_s$ , the next step is to repeat the conversion many times, and for each time, different values of  $\lambda_s$  will be chosen. The last step is to choose an optimal value of  $\lambda_s$  from the simulation results. Two standards for choosing a reasonable value of  $\lambda_s$  are applied here. First of all, since  $\lambda_s$  is a smoothing parameter, the value of  $\lambda_s$  cannot be too large to over smooth the data. Otherwise, parts of information from the raw data will be lost. In order to evaluate the smoothing effect that  $\lambda_s$  has on the velocities, the ratio of vector velocities' amplitude derived from simulation to the vector velocities' amplitude generated at the beginning of the simulation is calculated, and the ratios are shown in Figure 2.1 (a) and Figure 2.2 (a) for eastward and southward components, respectively. If the ratio is less than 0.8, the data is considered as over-smoothed, and the corresponding  $\lambda_s$  is regarded as unacceptable. Second of all, for each set of vector velocities derived by a specific value of  $\lambda_s$ , the root mean square (RMS) residual between these velocities ( $V_i(\lambda_s)$ ) and early synthetic vector velocities ( $V_i$ ) is calculated using the formula below,

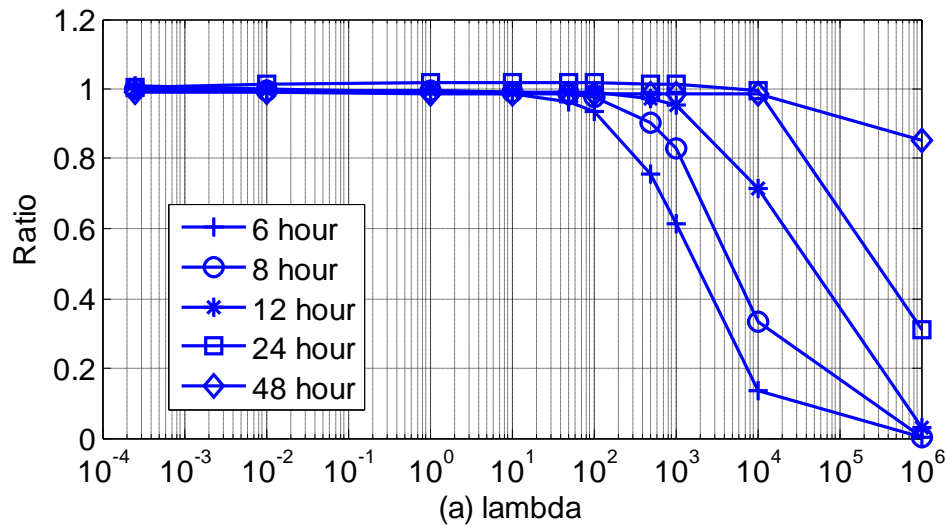
$$\gamma(\lambda_s) = \sqrt{\frac{\sum_{i=1}^n (V_i - V_i(\lambda_s))^2}{n}} \quad (2.4)$$

where  $n$  is the number of data points used in the simulation. The large RMS represents the large error occurred after the conversion. The RMS results are shown in Figure 2.1(b) and Figure 2.2(b) for eastward and southward components, respectively.



**Figure 2.1 (a) Ratios of amplitude of  $V_i(\lambda_s)$  to amplitude of  $V_i$  at eastward component; (b) results of RMS at eastward component.**

In Figure 2.1, the horizontal axis represents the value of  $\lambda_s$  used in the simulation. The minimum value of  $\lambda_s$  used in the simulation is the result of Eq. 2.3, which is the initial trial suggested by [Press *et al.* 1992], and the value is close to  $10^{-4}$ . In order to ensure the linear regularization method works well for all the velocity components, equal weight is added to each component while we examined the results. As shown in Figure 2.1(a), when  $\lambda_s$  is less or equal than  $10^{-2}$ , the ratio of 48- and 6-hour components are larger than 1, because the adopted  $\lambda_s$  cannot handle the random error in the synthesis data. When  $\lambda_s$  larger than  $10^2$ , the ratio of higher-frequency tidal components are less than 0.8, which is considered to be over-smoothed. Hence, only values of  $\lambda_s$  that fall in the range of  $10^{-2}$  to  $10^2$  are selected based on Figure 2.1(a). In Figure 2.1(b), for all the velocity components, the minimum residual for all the components occurs at when  $\lambda_s$  equals to 100. Combining the conclusions derived from Figure 2.1,  $\lambda_s$  equals to 100 seems to be a reasonable choice for the eastward component. However, the decision for choosing the optimum  $\lambda_s$  should be made based on the results of eastward and southward directions together.



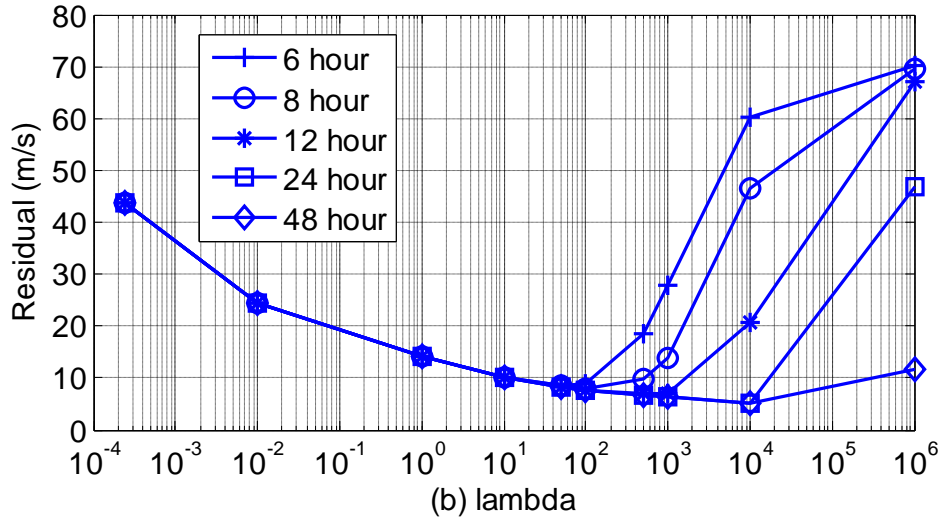


**Figure 2.2** Same as Figure 2.1 except for the southward component.

As shown in Figure 2.2(a), unlike the eastward component, all the values of  $\lambda_s$  less than  $10^2$  are not over-smoothing the data. In Figure 2.2(b), as the same with the eastward component, the minimum residual for all periods is obtained when  $\lambda_s$  is  $10^2$  as well. Hence,  $\lambda_s$  equals to  $10^2$  is also a good choice for southward component. According to the simulation results from both the eastward and southward components, the value of  $\lambda_s$  as  $10^2$  is chosen in this study to implement the linear regularization method.

## 2.2 Derivation of Neutral Winds

Since one of the goals of this thesis is to study the atmospheric tidal and planetary waves in the E- and F-regions, other than vector ion drifts, the derivation of neutral wind velocities are necessary as well. The conversion from ion vector velocities to neutral winds is introduced in this section.

### 2.2.1 Derivation of E-Region Neutral Winds

Assuming the acceleration term on the left side of the ion momentum equation (Eq. 1.1) is very small, neutral winds and ion drifts are coupled at E-region due to the effects of ion-neutral collision, electric and geomagnetic field, which is expressed as [e.g., Zhou *et al.*, 1997b],

$$\frac{e}{m_+ \nu_{in}} (\mathbf{V}_+ \times \mathbf{B} + \mathbf{E}) = \mathbf{V}_+ - \mathbf{U} \quad (2.5)$$

Since vertical neutral wind is very small compared to the horizontal winds, the upward wind is neglected in this study. Resolving Eq. 2.5 into the meridional (positive southward) and zonal (positive eastward) directions in the geomagnetic coordinate yields [e.g., Harper *et al.*, 1976; Zhou *et al.*, 1997b],

$$U_s = V_s + V_z \tan I \quad (2.6)$$

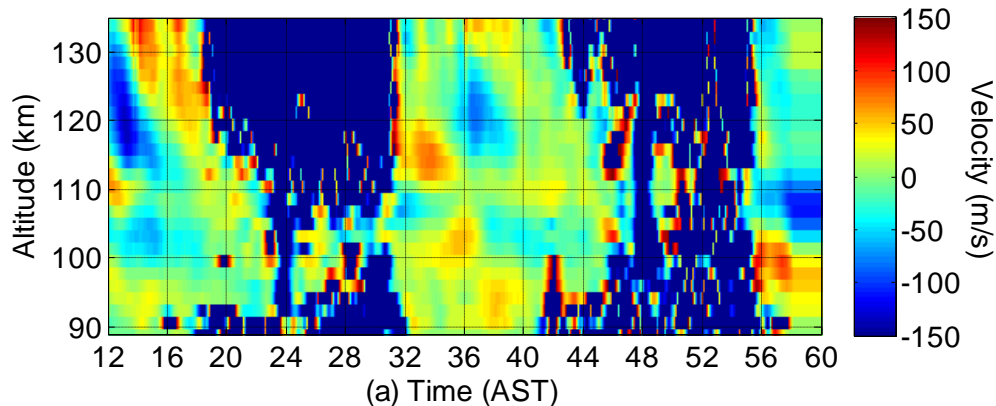
$$U_e = V_e - \frac{1}{\rho} (V_s \sin I - V_z \cos I + \frac{E_e}{B_0}) \quad (2.7)$$

where subscripts,  $s$ ,  $e$ , and  $z$ , represent southward, eastward, and upward components, respectively. Further,  $B_0$  and  $E_e$  are the magnitude of the magnetic field, and electric field in the eastward direction, respectively. The value of  $\rho$  is computed by using the Eq. 1.4. The value  $I$  and  $B_0$  are about  $45^\circ$  and 0.34 G, respectively. The intensity of eastward electric field can be measured by the F-region ion drift in the northward and perpendicular to the magnetic field line direction [Zhou *et al.*, 1997b]. Since the declination angle is about  $11^\circ$  to the west at Arecibo [Zhou *et al.*, 1997b], the relation between geographic coordinates ( $x$ ,  $y$ ,  $z$ ) and geomagnetic coordinates ( $x'$ ,  $y'$ ,  $z'$ ) are given by [e.g., Harper *et al.*, 1976],

$$\begin{aligned} V_x' &= V_x \cos 11^\circ + V_y \sin 11^\circ \\ V_y' &= -V_x \sin 11^\circ + V_y \cos 11^\circ \\ V_z' &= V_z \end{aligned} \quad (2.8)$$

where  $x$ ,  $y$ , and  $z$  represent the southward, eastward, and upward directions. Using the relationship shown in Eq. 2.8, Eq. 2.6 and Eq. 2.7 can be easily transformed into geographical coordinates. However, as seen from Eq. 2.6 and 2.7, unlike the southward wind, the eastward wind cannot be directly derived from the ion drifts, which also depends on  $\rho$  and the electric field.  $\rho$  is further dependent on the ratio of ion-neutral collision frequency to ion gyrofrequency. The ion drift velocity is about the same as the neutral wind velocity below  $\sim 110$  km because of strong ion-neutral coupling ( $\rho$  is very large, as shown in Figure 1.3). Above 110 km, the coupling of the zonal wind and the ion drift depends on both the ion-neutral collision frequency and the electric field. The error in zonal wind is typically too large to be useful above 135 km where the ion gyrofrequency is much larger than the ion-neutral collision frequency [Zhou *et al.*, 1997b]. As shown in Figure 1.3, the value of  $\rho$  is very small above 135 km, which means the error in the eastward wind will be amplified dramatically by a factor of  $1/\rho$ . Therefore, above 135 km, the quality of the derived neutral wind in the zonal component is not reliable. Since the eastward wind is only available below 135 km, the upper altitude boundary of eastward and southward winds in the geographical coordinate is 135 km. For this reason, the zonal and meridional wind components can be converted at the E-region, while at the F-region only the meridional wind in the geomagnetic coordinate can be obtained.

The eastward and southward winds in the geographical coordinate at the E-region heights in the period of Jan. 19-21, 2010 are shown in Figure 2.3, respectively.



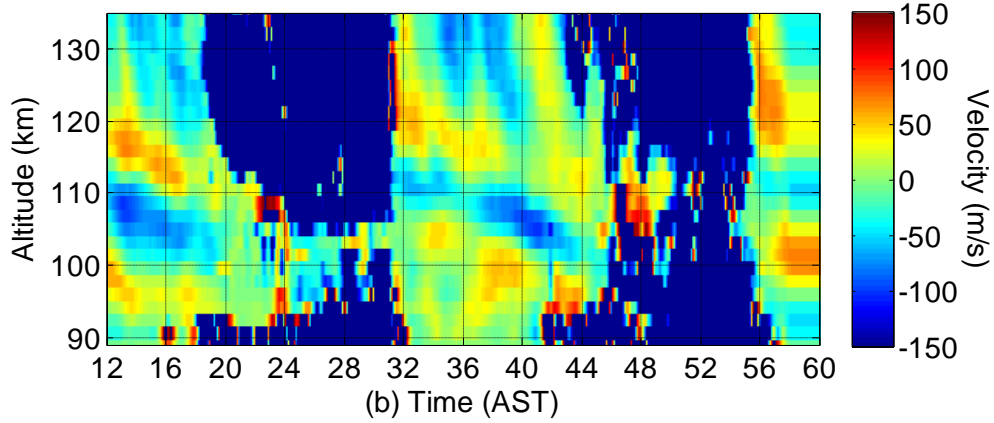


**Figure 2.3 (a) Eastward neutral wind and (b) Southward neutral wind in the geographic coordinate at E-region derived from the Arecibo ISR in the period of 12 LT Jan. 19 to 12 LT Jan. 21, 2010.**

As shown in Figure 2.3, for both neutral wind components, there are large data gaps during the nighttime at almost all altitudes, except at around 100 km. The reason is that the signal to noise ratio (SNR) of the received ISR power is extremely low due to weak ionization during the night, while at about 100 km, presence of the Sporadic E layers increased the plasma concentration which enhanced the SNR so that reliable data is available.

### 2.2.2 Derivation of F-region Meridional Wind

The meridional wind (southward positive) in the geomagnetic coordinate is derived from the following standard equation [e.g., *Buonsanto and Witasse, 1999*],

$$u_s = (v_{ap} - v_d) \sec I \quad (2.9)$$

where  $v_{ap}$  is the anti-parallel ion drift,  $I$  denotes the dip angle, and  $v_d$  is the diffusion velocity (positive upward). The diffusion velocity can be computed from the following equation [e.g., *Aponte et al., 2005*],

$$v_d = -D_a \frac{T_p}{T_r} \sin I \left( \frac{1}{n_e} \frac{dn_e}{dz} + \frac{1}{T_p} \frac{dT_p}{dz} + \frac{0.36}{T_r} \frac{dT_r}{dz} + \frac{1}{H_p} \right) \quad (2.10)$$

where  $D_a = \frac{2k_b T_i}{m_i v_{in}}$  is the ambipolar diffusion coefficient;  $n_e$  is electron density. Further,

$$T_p = (T_i + T_e)/2, \quad T_r = (T_i + T_n)/2, \quad \text{and} \quad H_p = \frac{2k_b T_p}{m_i g}$$

neutral temperature, respectively.  $T_i$ ,  $T_e$  and  $n_e$  are directly measured by the ISR. Diffusion velocity has only a weak dependence on  $T_n$ , which is derived from the MSIS-E-90 atmosphere model. On the other hand,  $v_d$  highly depends on the ion-neutral collision frequency, which is not known very accurately. At F-region heights, the dominant ion composition is largely  $O^+$ . For the  $O^+$  collision frequency, the following equation as described by *Buonsanto and Witasse* [1999] is used,

$$v_{in} = \frac{k_b \{0.3T_r^{0.5} (1 - 0.135 \log \frac{T_r}{1000})^2 [O] + 6.9[N_2] + 6.7[O_2]\}}{519.6 \times 10^{16} m_{O^+}} \quad (2.11)$$

where  $m_{O^+}$  is the  $O^+$  ion mass in atomic mass unit;  $[O]$ ,  $[N_2]$ , and  $[O_2]$  are neutral number densities in  $\text{cm}^{-3}$ . The values of those densities are adopted from the MSIS-E-90 atmosphere model. The southward wind calculated by the method described above is shown in Figure 2.4.

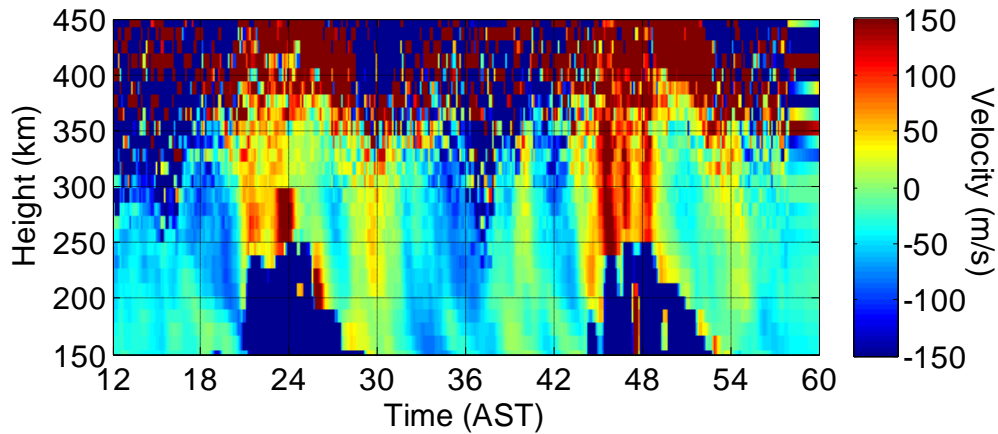


**Figure 2.4 Southward neutral wind in the geomagnetic coordinate at F-region heights derived from the Arecibo ISR in the period of 12 LT Jan. 19 to 12 LT Jan. 21, 2010.**

As shown in Figure 2.4, the derived velocity above 350 km has a relatively large error because the ambipolar coefficient is large in this region, and any inaccuracy in measurements is greatly amplified. The only difference between Eq. 2.6 and Eq. 2.9 is that Eq. 2.9 includes the diffusion term  $v_d$ . At lower E-region, the diffusion velocity is negligible, while at higher altitudes, the diffusion term becomes important. Please be aware again that the F-region neutral wind discussed in this thesis is merely the meridional component in the geomagnetic coordinate because the error in zonal wind is typically too large to be useful above 135 km.

### **2.3. Constrained Fitting**

Because of low ionization at nighttime E-region non-auroral latitudes, ISR data contains large data gaps. The lack of nighttime data in the E-region results makes it difficult to obtain accurate harmonic fittings, especially those of the diurnal and semidiurnal components in the neutral winds. As discussed in *Zhou et al.* [1997a], one problem is that the fitting results are often not realistic for the nighttime period when there is no data available. This can be illustrated by the following simulation.

The simulation begins by constructing a velocity data using two harmonic components and one DC term with random error. Due to the limitation of ISR during the nighttime, only 12 hours (from 7-hour to 19-hour, grey area in Figure 2.5) of this synthetic data is available for performing the least squares fitting (LSF). The fitting result is shown by a blue curve in Figure 2.5.

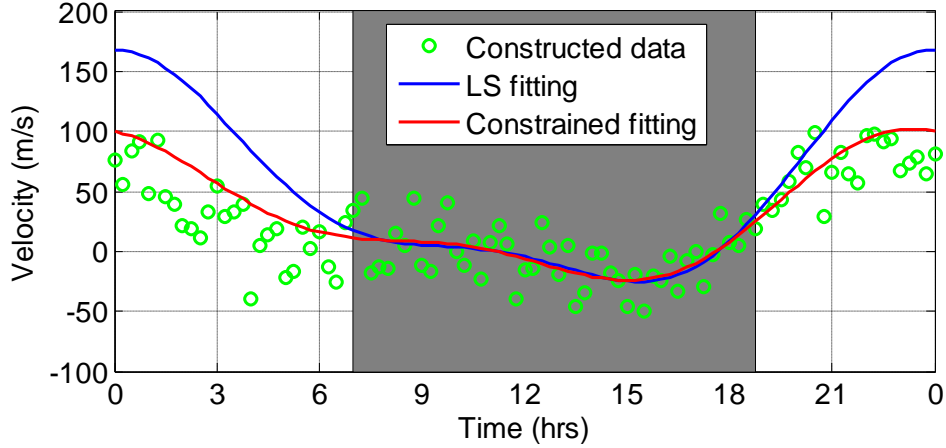


**Figure 2.5 Least square fitting result (blue line) and constrained fitting result (red line) for constructed data (green circles).**

The LSF method shows reasonable fitting result in the time range from 7-hour to 19-hour, while at other hours (the white area shown in Figure 2.5), the fitting result is obviously larger than the constructed data. To alleviate this issue, a limit on the minimum and maximum values during the night is imposed. Although reliable nocturnal data are not available from the ISR measurement, we at least know that nighttime neutral wind velocity cannot go beyond a certain value, for example, 200 m/s in the E-region. Therefore, a physical constraint is added into least square method. Instead of minimizing the least square error of the daytime data, we fit the harmonic components to minimize the following error function,

$$f_{err} = \frac{1}{N} \sum_{i=1}^N [F_{day}(i) - y(i)]^2 \left( 1 + \frac{1}{M} \sum_{j=1}^M \left| \frac{F_{night}(j)}{V_{max}} \right|^\beta \right) \quad (2.12)$$

In the above equation,  $F_{day}$  and  $F_{night}$  are the composite of the fitted results sampled during day and night, respectively, while  $y$  is the daytime measurement.  $V_{max}$  is the maximum value imposed, which is chosen to be 100 m/s in the simulation. The choice of  $\beta$  needs to make the second term in the parenthesis much larger than one when  $F_{night}(j)$  for any  $j$  is larger than  $V_{max}$ , and negligible otherwise. The exact value of  $\beta$  is not important, as long as it is much larger than 1. The value of  $\beta$  used in the constrained

fitting (CF) is 100. The CF result is shown in Figure 2.5 as a red curve. As we can see from the CF results, at the non-data part (white area shown in Figure 2.5), the CF result is closer to the constructed data than the LSF result. This implies that the CF method drastically improves the accuracy of the fitting parameters whenever  $F_{night}$  becomes larger than  $V_{max}$ . Moreover, during the daytime, the CF result is as good as the LSF result, which means the CF method will not influence the result when the data quality is good.

# CHAPTER 3

## ANALYSIS OF LOWER-FREQUENCY TIDAL AND QUASI-2 DAY PLANETARY WAVES AT ARECIBO

### 3.1 Introduction of Tidal Waves

Atmosphere tidal waves are large scale atmospheric fluctuations, which are primarily excited by solar heating of the atmosphere. Since the atmosphere is heated only during the day and differently at different altitudes, the uneven heating will generate a tidal wave with periods related to a solar day. Periods of 24- (diurnal) and 12-hour (semidiurnal) tides (lower-frequency tides) are frequently observed and studied for a long time. These tides have large horizontal amplitudes, and significantly influence energy transportation in the atmosphere. In addition, 8- (terdiurnal) and 6-hour (quad-diurnal) tides (higher-frequency tides) are observed as well with smaller amplitudes [e.g., *Tong et al.*, 1988; *Morton et al.*, 1993; *Zhou et al.*, 1997a, *Smith et al.*, 2004]. Based on different propagation mechanisms, atmospheric tides can be divided into two subsets, migrating tides and non-migrating tides. Migrating tidal components propagate with the same pace as the apparent motion of the sun, which means local time variations of migrating tidal components are independent of longitude. Let  $s$  and  $n$  denote zonal wavenumber and subharmonic of a solar day, respectively, the migrating tidal components are westward propagating tides with  $n = -s$ . The sign of  $s$  represents the direction of wave propagation (positive eastward). On the contrary, non-migrating tidal components have not the same local time variation at different longitudes. In other words, non-migrating tides propagate westward with different speed as the apparent motion of the sun, they propagate eastward, or they are standing oscillations.

Because density decreases with increasing altitude in the atmosphere, amplitudes of tidal components excited from lower altitudes are increased while they are propagating upward. Hence, amplitude of tidal components generated at a lower altitude could be amplified to a great extent after they reach a higher altitude. Once those upward

propagating tides are dissipated, they will deposit their energy in higher altitudes and introduce large atmospheric variation. Likewise, downward propagating tidal components could transport energy into lower altitudes. Interactions between tidal components and gravity waves or planetary waves also could cause atmospheric variations on a local or global-scale. Since understanding the atmospheric tides is the key to understand energy transportation in the atmosphere, numerous theoretical and observational studies about the atmospheric tides have been reported. In 1970, *Chapman and Lindzen* provided a detailed review of atmosphere tidal theory. They investigated the atmospheric tidal equations and discussed the different methodologies of solving the equations. *Forbes* [1982a, 1982b] reported diurnal and semidiurnal tidal results derived from a comprehensive numerical model. He concluded that atmospheric tides are primarily generated by three excitation mechanisms, which are in-situ absorption of solar energy, ion-neutral momentum coupling, and gravitational forcing. Based upon the *Forbes'* numerical model, *Hagan et al.* [1995] introduced the Global-Scale Wave Model (GSWM). Important atmospheric parameters, such as, background winds, tidal forcing, and dissipation can be specified in the GSWM, which can provide more realistic tidal results. A tutorial about tidal and planetary waves from basic mathematics and physics principals can be found in *Forbes* [1995]. He concluded that migrating tides are mainly excited by oxygen atoms absorbing the ultraviolet radiation in the mesosphere and lower thermosphere (MLT) region. In the lower altitudes, migrating tides are primarily generated by the absorption of solar radiation by ozone in the stratosphere and water vapor in the troposphere. In 2001, *Hagan and Roble* suggested that non-migrating tides could be excited by the nonlinear interaction between the migrating tides and planetary waves based on the data obtained from thermosphere-ionosphere-mesosphere-electrodynamics general circulation model (TIME-GCM). *Hagan and Forbes* [2002] used GSWM and reported that in the troposphere, non-migrating tides are mainly excited by latent heat release. Aside from theoretical studies, considerable wind observations by satellites [e.g., *Huang and Reber*, 2003; *Wu et al.*, 2008a, 2008b; *Xu et al.*, 2009; *Iimura et al.*, 2010], VHF meter radars [e.g., *Thayaparan and Hocking*, 2002; *Lau et Al.*, 2006; *Lu et al.*, 2011], and lidars [e.g., *She et al.*, 2004; *Sherman and She*, 2006; *Li et al.*, 2009] have been made. One advantage of satellite data is that the data contains information at

different longitudes, so that migrating and non-migrating tidal modes can be separated from each other. Satellite-borne instruments for wind and temperature measurement are the most important tool to investigate migrating or non-migrating tides. All kinds of space-borne instruments and theoretical models provide a fundamental platform to study the characteristics of atmospheric tides.

Numerous observational studies about tidal waves are limited at the MLT region due to lack of effective measurement at the other regions. Above 116 km, ISR is largely the only choice for scientists to study time-varying wind or temperature profiles. Although extensive observational studies about diurnal and semidiurnal tides using ISR data have been published at Arecibo's latitude, to our knowledge, only three papers [Harper *et al.*, 1976; Harper, 1981; Zhou *et al.*, 1997a] focused on the study of atmospheric tidal components during the winter season. In this chapter, a rigorous analysis of tidal and planetary waves at E- and F-region heights during the period of January 14-23 in 2010 is presented. The combination of using a dual beam configuration, linear regularization, and constrained fitting make the results obtained here more accurate than before. Since the data is collected from a single radar station, atmospheric tides reported in this study are the combination of migrating and non-migrating tidal components.

## **3.2 Power Spectral Density Analysis**

For a given neutral wind data, the information of dominant tidal and planetary components in this data set can only be obtained after performing power spectral density analysis. In other words, power spectral density, or periodogram, gives an overview of the dominant oscillation modes. Due to the uneven temporal sampling, the Lomb-Scargle method [Lomb, 1976; Scargle, 1982; Press *et al.*, 1992] is applied in this thesis to derive the periodograms of meridional and zonal neutral wind components at E- and F-regions, respectively.

### 3.2.1 Periodograms of F-region Meridional Wind

As discussed in Chapter 2, at F-region heights, only the meridional wind in the geomagnetic coordinate can be deduced from ISR measurement. The periodogram of F-region southward wind during Jan. 14-23, 2010 is shown in Figure 3.1.

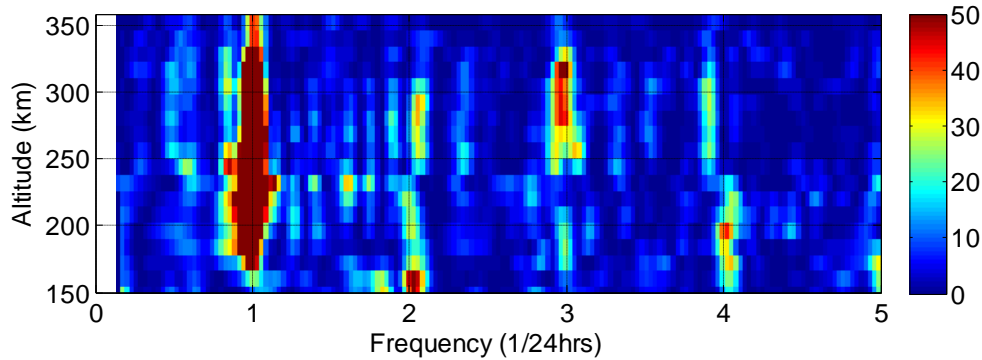


**Figure 3.1 Periodogram of the meridional wind during Jan. 14-23, 2010.**

As shown in Figure 3.1, the meridional wind exhibits strong oscillations at periods of 24-, 12-, 8-, and 6-hour, respectively. The 24-hour oscillation is the most dominant component and it is prominent at almost all altitudes. The 8-hour component becomes important above 250 km. In the altitude range from 270 to 330 km, the magnitude of the 8-hour component is comparable to that of the diurnal component and is larger than semidiurnal component. The 6-hour oscillation is strong around 200 km. In order to examine the temporal stability of dominant oscillation modes, nine days' data are separated into two sub-periods, first four days (Jan. 14-18) and last five days (Jan. 18-23), respectively. Periodograms in those two sub-periods for the F-region meridional wind are shown in Figure 3.2.

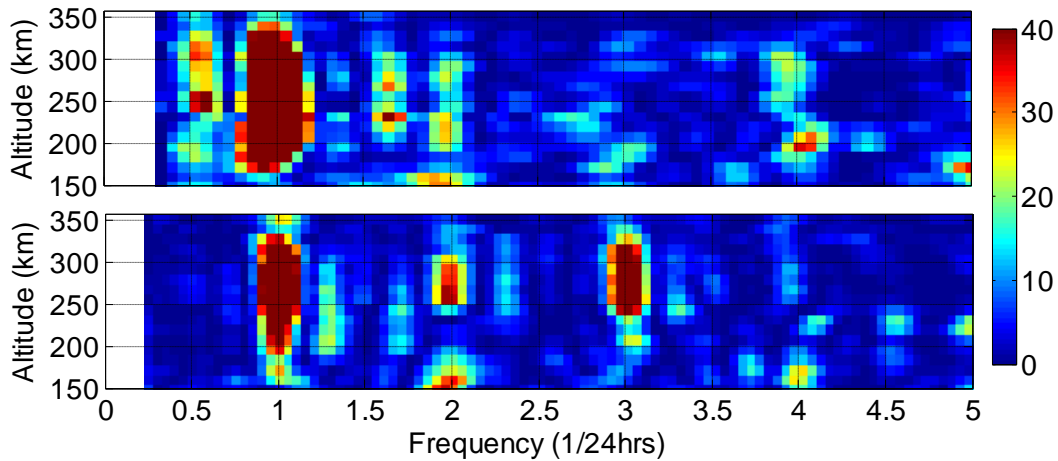


**Figure 3.2 Periodogram of the F-region meridional wind during (top) 16 LT Jan. 14 to 07 LT Jan. 18, (bottom) 09 LT Jan. 18 to 11 LT Jan. 23, 2010.**

As seen in Figure 3.2, the dominant oscillation components in the two sub-periods are not consistent. Periodogram of the first four days shows five strong oscillations which are 6-, 12-, 15-, 24-, and 40-hour, respectively. The diurnal oscillation is extremely dominant and it processes a dramatic portion of meridional wind energy. The rest energy seems to be divided equally by the other four components. Figure 3.2 (bottom) exhibits strong 8-, 12-, and 24-hour oscillations during the last five days. Compared with the periodograms of two sub-periods, the 6-, 15-, and 40-hour components only exist in the former sub-period, while the 8-hour component becomes very important in the latter sub-period. The coexistence of 15-, and 40-hour components might imply that the 15-hour component is generated by nonlinear interaction between 24-, and 40-hour oscillations. In the latter sub-period, the diurnal component is still the strongest oscillation. Although the semidiurnal component is the weakest oscillation, it becomes stronger compared with it in the first four days. The magnitude of 8-hour component is very strong above 250 km, which is comparable with 24-hour component and overwhelms the 12-hour component. Based on the periodograms shown above, the 24-hour component is the most stable and

strongest oscillation during the entire observation. The 8-hour component is very strong during the last five days.

### 3.2.2 Periodograms of E-region Neutral Winds

In the E-region, two components of neutral winds in the geographic coordinate can be deduced from ionospheric parameters measured by ISR. The periodogram of E-region meridional and zonal neutral winds during Jan. 14-23 in 2010 is shown in Figure 3.3.

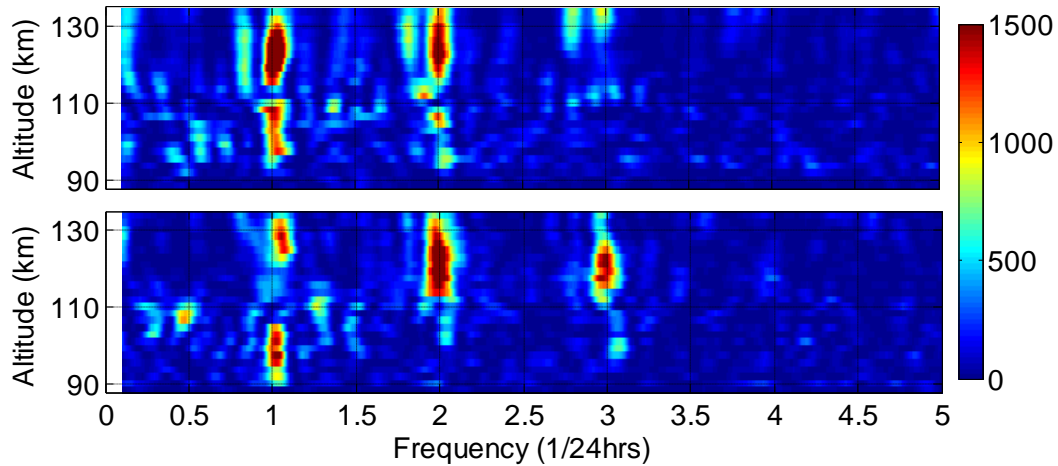


**Figure 3.3 Periodogram of the E-region (top) meridional wind, (bottom) zonal wind during Jan. 14-23, 2010.**

As shown in Figure 3.3, both meridional and zonal components show strong 24-, and 12-hour oscillations. At an altitude range of 110 km to 130 km, the 24-, and 12-hour oscillations are dominant in the meridional component, while in the zonal direction, the 12-, and 8-hour oscillations are prominent at that altitude range. Below 110 km, the 24-hour oscillation is dominant in both the meridional and zonal directions. By separating the E-region neutral winds data in the same way as performed in the F-region meridional

wind, we show the periodogram of two neutral winds components during the first four days, and last five days in Figure 3.4, and Figure 3.5, respectively.

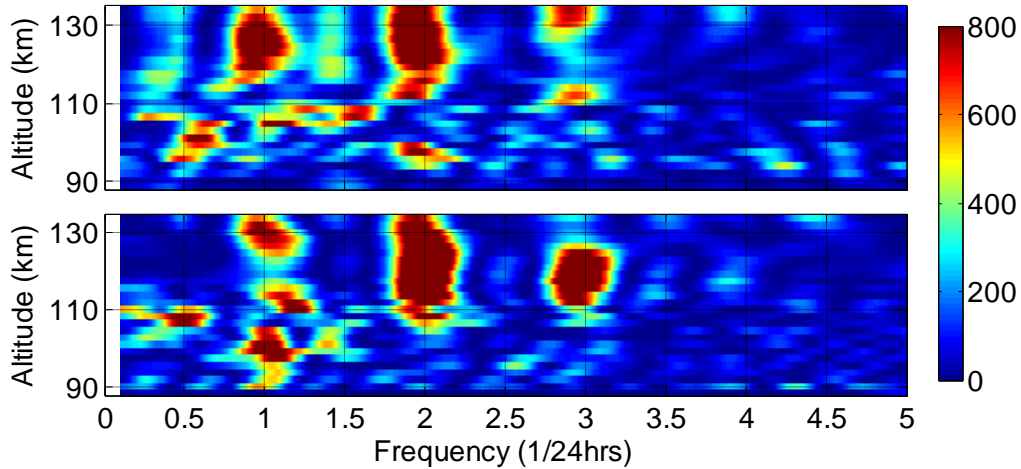


**Figure 3.4 Periodogram of the E-region (top) meridional wind, (bottom) zonal wind during 16 LT Jan. 14 to 07 LT Jan. 18, 2010.**

In Figure 3.4 (top), as the results of entire period shown in Figure 3.3 (top), the periodogram in the meridional component shows strong 24-, and 12-hour oscillations above 110 km. The 8-hour oscillation in this sub-period is exhibited to be strong above 130 km and around 110 km. In the zonal component shown in Figure 3.4 (bottom), the periodogram is consistent with the result of entire period. The semidiurnal component is dominant in both neutral winds components above 110 km.

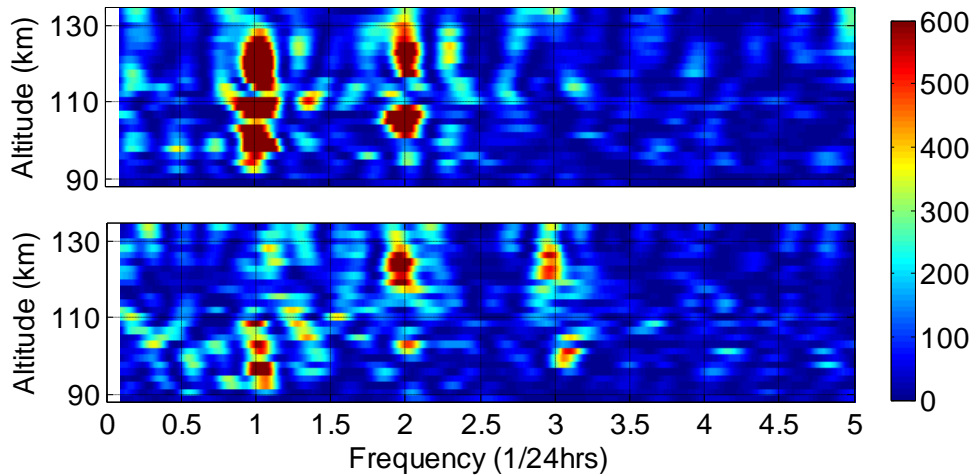


**Figure 3.5** Same as **Figure 3.4** except in the period of **09 LT Jan. 18 to 11 LT Jan. 23, 2010**.

On the contrary to the periodogram shown in **Figure 3.4** (top), the 8-hour oscillation did not appear in the meridional wind during the second sub-period. The 24- and 12- hour oscillations are the only two strong components shown in the meridional direction. As shown in **Figure 3.5** (bottom), in the zonal direction, the 12- and 8-hour oscillations are dominant above 110 km, and 24-hour oscillation dominates below 110 km.

According to the periodograms shown in this section, the dominant oscillation modes in different regions and different neutral wind components are known. Those dominant components are extracted simultaneously from the neutral winds data. A specific fitted harmonic components in different regions and wind components are listed in **Table 3.1**. The harmonic fitting results of different components are presented and discussed in the following sections.

**Table 3.1 Simultaneously fitted oscillation modes in the E- and F-regions, and different neutral wind components.**

	Meridional Wind Simultaneously fitted oscillation modes (hours)		Zonal Wind Simultaneously fitted oscillation modes (hours)	
	Jan. 14-18	Jan. 18-23	Jan. 14-18	Jan. 18-23
F-region	40,24,15,12,6	24,12,8	---	---
E-region	24,12,8	24,12	24,12,8	24,12,8

### 3.3 Results and Discussion of Diurnal Tide

Based on previous atmospheric tidal studies made at Arecibo, the diurnal tide is observed to be dominant below 110 km, and the semidiurnal tide dominates the wind field above that altitude [Harper 1979, 1981]. However, the periodogram shown in Figure 3.1 suggests that the diurnal tide is prominent in the F-region in the winter. The fitting results of 24-hour component in the meridional wind during Jan. 14-18, 2010 are shown in Figure 3.6.

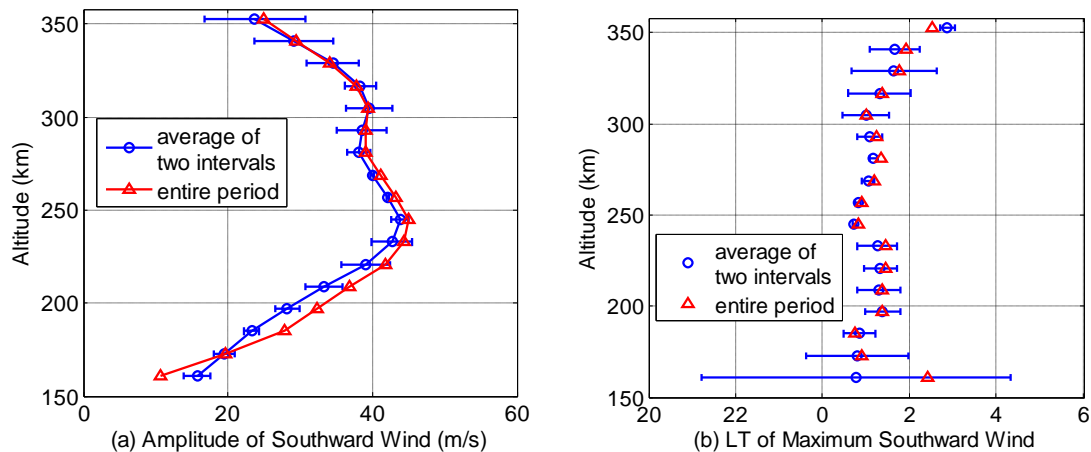


**Figure 3.6 (a) Amplitude, and (b) phase results of the 24-hour component for the F-region meridional wind. The red curve is the least square fitting result using 4 days' data from January 14-18, 2010. The blue curve is the average by breaking the Jan. 14-18 period into two subintervals.**

The red curve is the fitting result using the entire first four days' data from Jan. 14 to Jan. 18. To quantify the variability, the four days' data are separated into two subintervals. The average from the two subintervals is plotted as a blue curve and the standard deviations are plotted as error bars. This plotting scheme is applicable to all figures shown in this thesis which represent the amplitude and phase results in the period of Jan. 14-18, 2010. As shown in Figure 3.6 (a), the diurnal amplitude is prominent, which is larger than 20 m/s above 175 km, and its maximum magnitude occurs at around 245 km with a speed of 45 m/s. The amplitude results of the entire period and two averaged subintervals are very consistent. The short lengths of the error bars imply that the diurnal amplitude variation during the first four days is small. The diurnal phase result, shown in Figure 3.6 (b) is consistent and asymptotic to a constant value at altitude range from 180 to 300 km. This phase behavior may cause by the dominance of diffusion and meanwhile lack of sources of heat or momentum in the F-region [Forbes 1982a]. Below 180 km, there exhibit large phase variations, which may cause by inappreciable diurnal amplitude in the meridional wind. The harmonic fitting results of F-region diurnal tide in the meridional wind at the period of Jan. 18-23 in 2010 are shown in Figure 3.7.

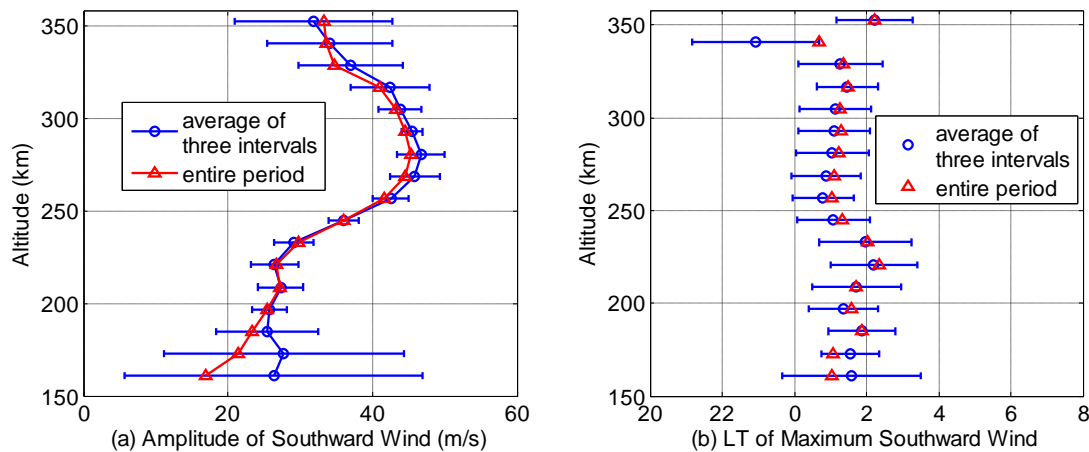
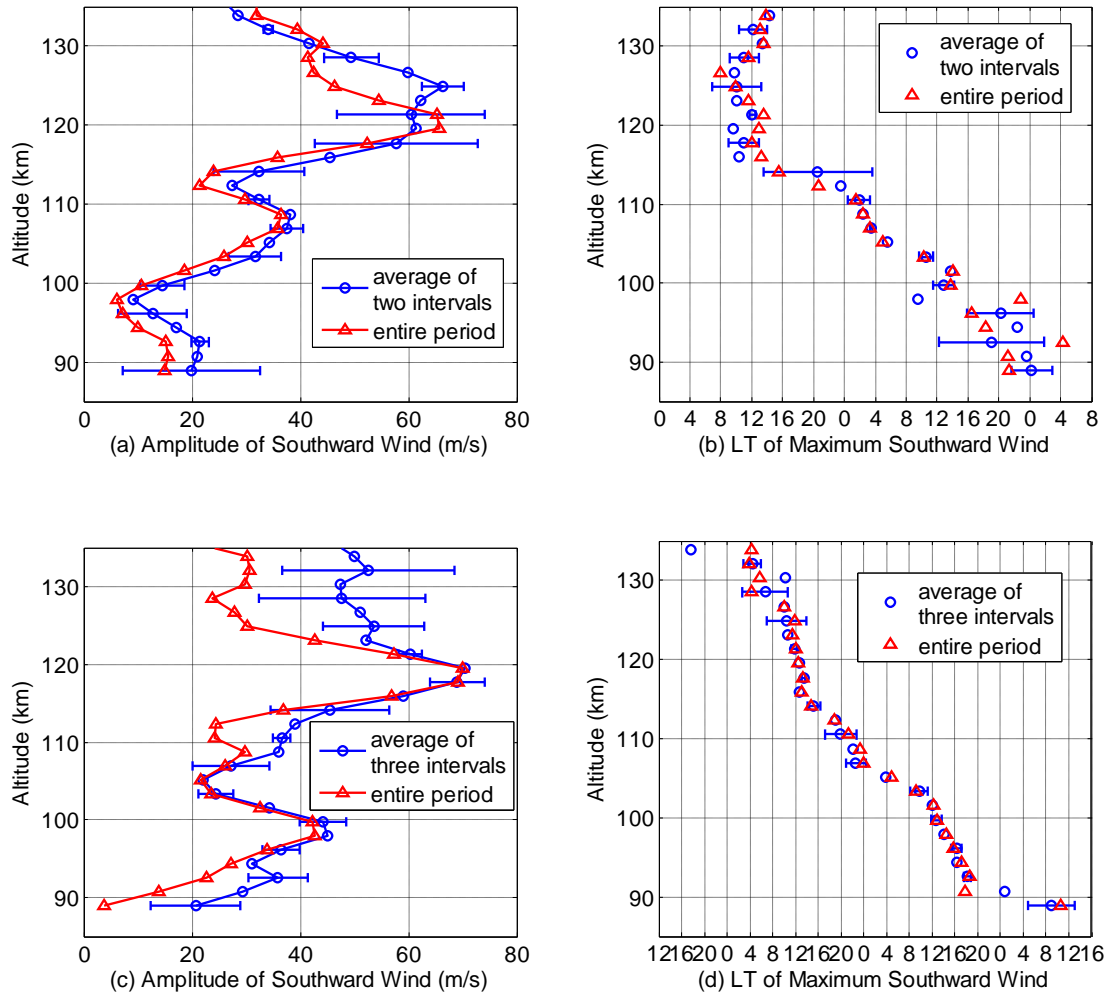


**Figure 3.7 (a) Amplitude, and (b) phase results of 24-hour component for the F-region meridional wind. The red curve is the least square fitting result using 5 days’ data from January 18-23, 2010. The blue curve is the average by breaking the Jan. 18-23, 2010 period into three subintervals.**

As in Figure 3.6, the red curve is the fitting result using 5 days’ data. The blue curve is the average, determined by dividing the 5 days into 3 subintervals and the standard deviation, as before, is shown as error bars. Likewise, the above plotting scheme is applicable to all figures shown in this thesis which represent the amplitude and phase results during Jan. 18-23, 2010. As seen from Figure 3.7, the amplitude and phase of diurnal tide in this sub-period behave similar to the previous sub-period. The only difference is that the amplitude becomes stronger above 250 km, which results in an even smoother phase variation above that height. The peak amplitude that occurred in the last five days has the same intensity trajectory shifted 30 km higher than it exhibited in the first four days. Like the previous sub-period, the phase is largely constant during the last five days. From the averaged amplitude and phase results on both sub-periods, we can see that the diurnal tide is extremely stable at the altitude range from 200 to 320 km.

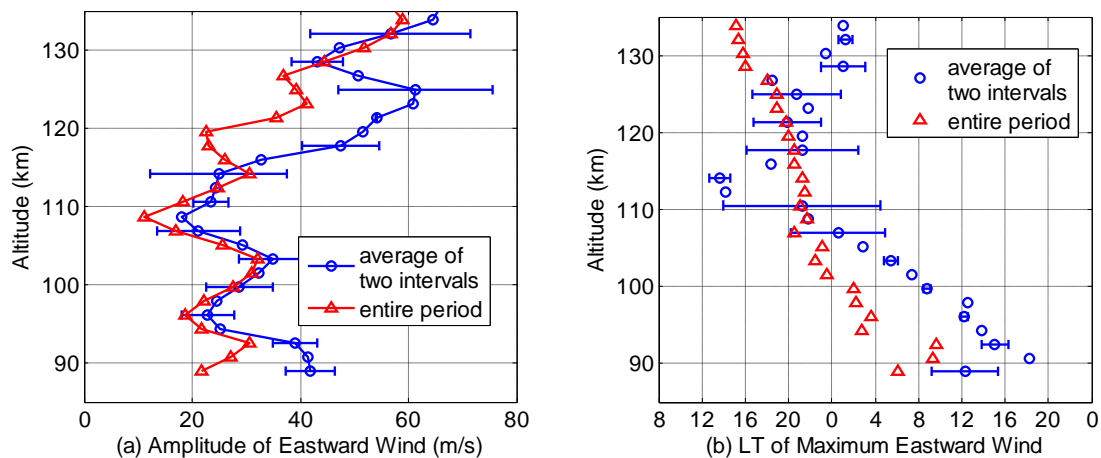
The diurnal tide is observed to be very important in the lower E-region [e.g., Mathews, 1976; Harpar, 1977]. The periodogram shown in Figure 3.3 supports that conclusion. However, the periodogram and harmonic fitting results of the diurnal

component are suspicious because of the limitation of the ISR measurement during the nighttime at E-region heights. Without nighttime data, the harmonic fitting results could be underestimated or overestimated by a factor of 2 [Zhou *et al.*, 1997a]. With the constrained fitting method, the data gap issue can be alleviated. Nevertheless, the experiment made by Zhou *et al.* [1997a] revealed that the diurnal amplitude is often underestimated when some constraints are imposed during nighttime. The amplitude and phase results of diurnal tide in the meridional wind at E-region are shown in Figure 3.8.



**Figure 3.8** Amplitude and phase results of 24-hour component for the E-region meridional wind during January 14-18, 2010 (a, b), and January 18-23, 2010 (c, d).

As shown in Figure 3.8 (a, c), the peak diurnal amplitude on both sub-periods occurs almost at the same altitude, around 120 km. The peak amplitude intensity during the first four days, and the last five days are 65 m/s, and 70 m/s, respectively. Below 110 km, the amplitude results show large difference between two sub-periods. During the first four days, the amplitude is less than 20 m/s below 100 km, and the peak amplitude below 110 km occurs at an altitude around 108 km, with magnitude of 36 m/s. In the period of last five days, the amplitude is larger than 20 m/s above 92 km, and maximum magnitude is 43 m/s occurred at 98 km. Despite the large day-to-day amplitude variation, the phase is largely consistent, especially in the regions where the amplitude is appreciable. In Figure 3.8 (b, d), the phase results on both sub-periods show two distinct regions of variation. Above 114 km, the phase in the first sub-period can consider as a constant value after ignoring the small fluctuation. In the second sub-period, the phase progresses downward with a vertical wavelength of 63 km. Between 90 km to 114 km, the phase exhibits linear variation with an estimated vertical wavelength of 24 km, and 20 km in the first and second sub-periods, respectively. The results of vertical wavelengths are consistent with the results reported by Zhou *et al.* [1997a]. Their observation is also made on January at Arecibo, and observed diurnal tide in the meridional wind with a vertical wavelength as 70 km above 110 km, and 22 km below this altitude. The amplitude and phase results of diurnal tide in the zonal wind at the E-region heights are shown in Figure 3.9.



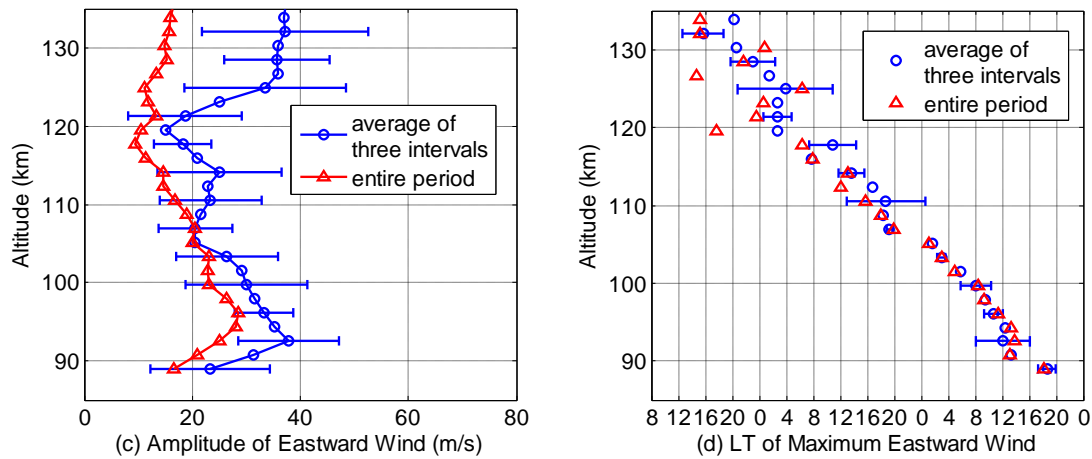


**Figure 3.9** Same as **Figure 3.8** except for zonal component.

As shown in Figure 3.9 (a, c), the amplitude results of entire period and average of subintervals have large discrepancy above 120 km in both sub-periods. It is hard to draw any conclusion based on the amplitude results above 120 km. The peak amplitude in the first and second sub-period occurs at around 103 km, and 96 km, respectively. As seen from Figure 3.9 (b), the phase results of averaged subintervals and the entire period are inconsistent, which manifests that larger phase variations occurred during the first four days. The vertical wavelength is impossible to be predicted in this sub-period. During the last five days, the phase results are largely consistent below 120 km. In this sub-period, phase shows a downward progression and vertical wavelength is estimated to be 18 km.

### 3.4 Results and Discussion of Semidiurnal Tide

The semidiurnal tide in the meridional wind at F-region heights at Arecibo has been reported by *Harper* [1977, 1979, and 1981]. He concluded that the semidiurnal tide is the strongest tidal component in the F-region at Arecibo's latitude. However, periodograms shown in Figure 3.1 and 3.2 suggest that the diurnal tide is the most dominant tidal component during the observation. The semidiurnal tide is weaker than 8-hour tide at almost all altitudes, and even weaker than 6-hour oscillation mode at some

altitudes. The amplitude and phase results of semidiurnal tide in the meridional wind during Jan. 14-18, 2010, are shown in Figure 3.10.

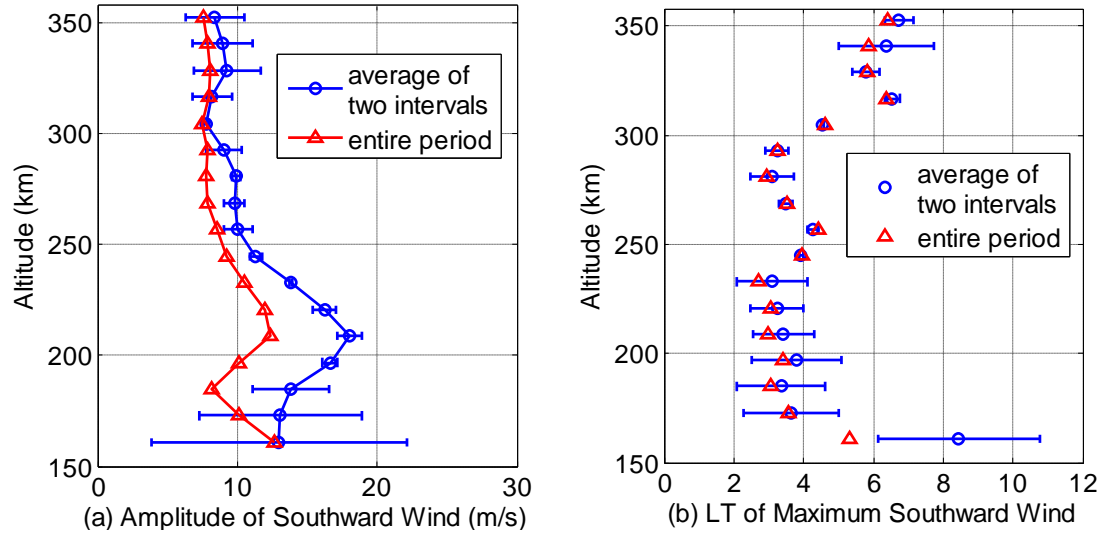


**Figure 3.10** Same as **Figure 3.6** except for semidiurnal component.

As shown in Figure 3.10 (a), the amplitude of semidiurnal component is constantly less than 10 m/s above 235 km. The maximum amplitude occurs at around 210 km with a velocity of 12 m/s. Above 310 km or below 190 km, the semidiurnal amplitude shows large day-to-day variations. In Figure 3.10 (b), the semidiurnal phase is consistent in the altitude range from 172 km to 292 km. The phase variation is within about 2 hours in that altitude range. This phase vertical structure agrees with a theoretical study reported by *Forbes* [1982b]. The harmonic fitting results of semidiurnal component for the F-region meridional wind at the period of Jan. 18-23, 2011 are shown in Figure 3.11.

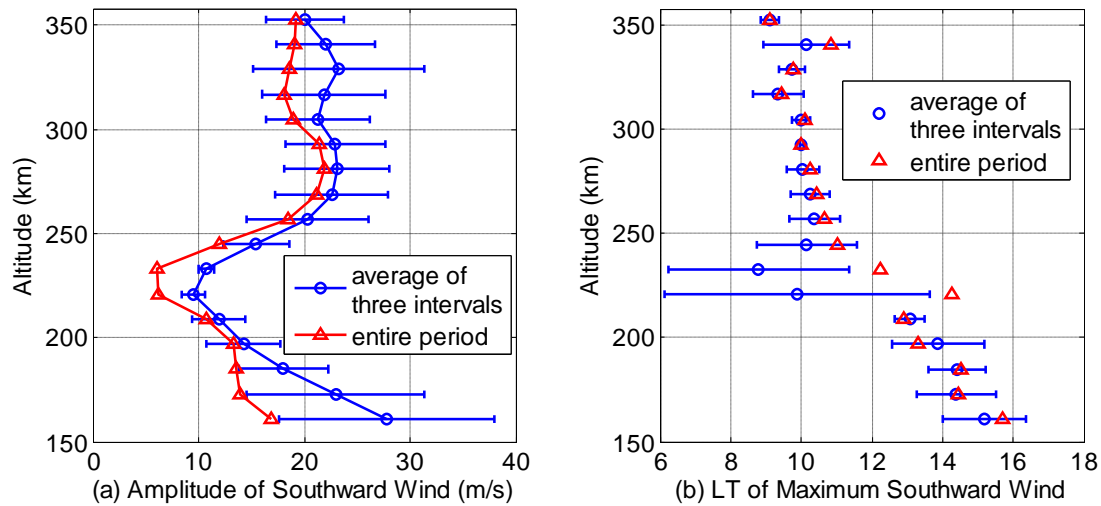
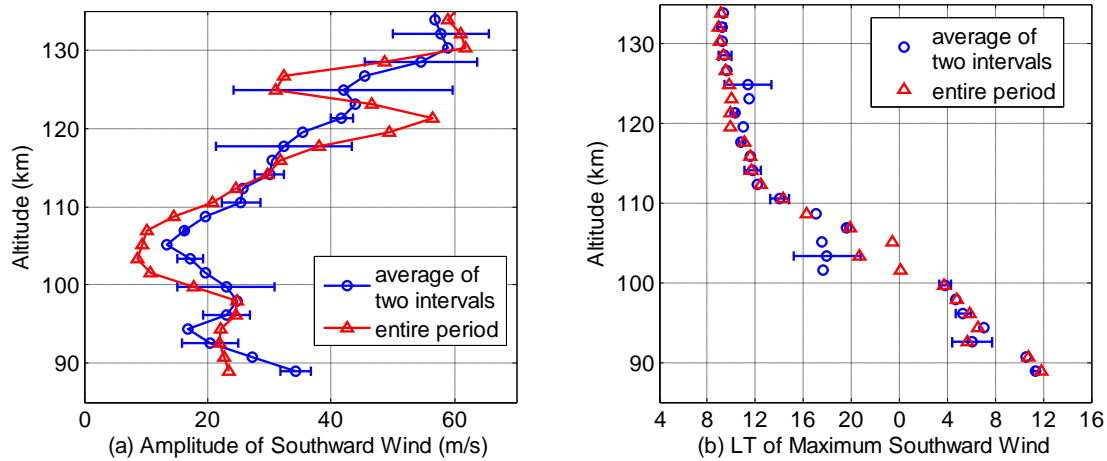


**Figure 3.11 Same as Figure 3.7 except for semidiurnal component.**

On the contrary to the previous sub-period, the semidiurnal amplitude is persistently larger than 10 m/s at almost all altitudes except at a short altitude range from 215 km to 240 km. The peak amplitude appears at about 280 km with magnitude as 22 m/s, which is almost twice larger than it in the previous sub-period. In Figure 3.11 (b), the semidiurnal phases are consistent except at the short altitude range where amplitudes are less than 6 m/s. The phase exhibits linear variation and propagates downward with an estimated vertical wavelength of 300 km. Notice that above 250 km, the behavior of semidiurnal amplitude and phase are very different between two different observational sub-periods. The amplitude of semidiurnal tide in the second sub-period is more than twice as large as it in the first sub-period. Correspondingly, the semidiurnal phase in the second sub-period is more stable than it in the second sub-period above 250 km. At altitude range from 250 km to 310 km, there seems to be 180 degrees phase shift between two sub-periods. The enhanced magnitude and half period of phase difference imply that semidiurnal oscillation gain energy in the second sub-period. There are three possible ways for the semidiurnal component to obtain energy. One is that a new semidiurnal tidal component may be generated during the last five days. The semidiurnal tide is thought to be excited by combination effects of in situ extreme ultraviolet (EUV) solar radiation absorption, momentum coupling of diurnal winds and ion drag, and propagating up tidal energy from

lower atmosphere [Forbes 1982b]. Hagan *et al.* [2001] reported a theoretic result that the phases of in situ solar driven semidiurnal tides are largely evanescent in the thermosphere. The observed semidiurnal tide during the last five days shows limited phase progression from 250 km to 310 km. It appears that the semidiurnal tide in the observation is more consistent with the first excitation mechanism, which is excited by in situ solar driven force. Since the 6-, 15-, and 40-hour components only exist during the first four days, they are dissipating along with the observation and eventually deposited their energy in the background atmosphere. Therefore, the second way for the semidiurnal tide obtained energy is to absorb from the background atmosphere deposited by those three oscillations. The third way is the combined effects of previous two ways.

Zhou *et al.* [1997a] claimed that the semidiurnal tide is the most dominant component in the altitude range from 108 km to 125 km based on the ten days' observation during January in 1993. The periodogram shown in Figure 3.3 further supports that conclusion. The harmonic fitting results of semidiurnal tide in the E-region meridional wind are shown in Figure 3.12.



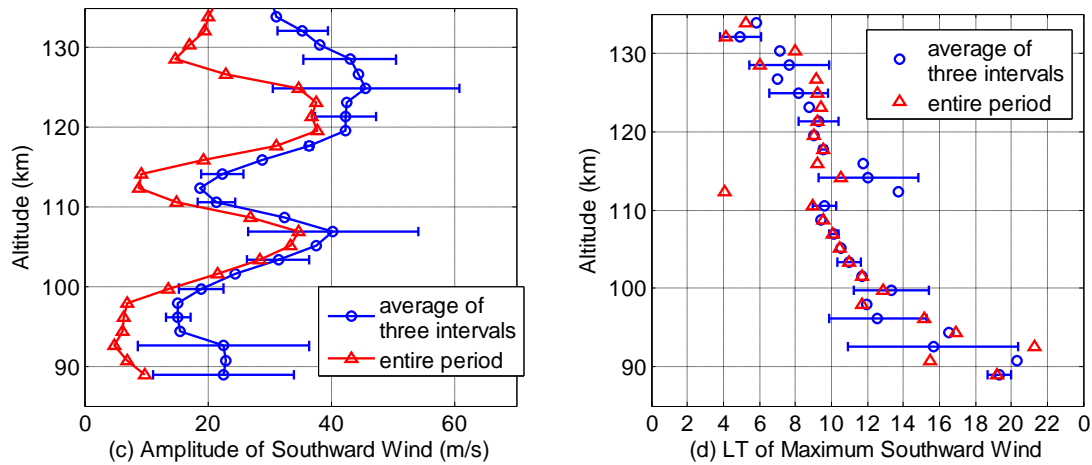


**Figure 3.12** Same as **Figure 3.8** except for semidiurnal component.

As shown in Figure 3.12 (a), the semidiurnal wind in the meridional plane is larger than 20 m/s above 110 km. The peak amplitude occurs at around 130 km with a magnitude of 62 m/s. The amplitude grows rapidly from 10 m/s at around 106 km to 56 m/s at about 121 km. Within 15 km the amplitude grows 46 m/s. This semidiurnal amplitude feature is consistent with the one reported by *Zhou et al.* [1997a]. They further suggest that this consistent increase of semidiurnal amplitude is very useful to estimate the turbopause. The turbopause is a region where eddy viscosity begins to drop sharply while molecular viscosity is about to take in charge. In the altitude range from 106 km to 121 km, the stably increased amplitude manifest that the dissipation of semidiurnal tide is limited. This further implies that the combined effects of increased molecular viscosity and rapidly dropped eddy viscosity are not adequately large to stop the wave from growing. Hence, the turbopause estimated here is around 110 km. The phase of the semidiurnal component in the first sub-period is shown in Figure 3.12 (b), which is very predictable, and can be separated into two regions based on the slopes of phase propagation. Above 112 km, the slope is very shape, and the corresponding vertical wavelength is about 68 km. below 112 km, the phase progresses linearly with an estimated vertical wavelength of 12 km. As shown in Figure 3.12 (c, d), the semidiurnal component behaves differently during the last five days. In Figure 3.12 (c), the altitude variation of semidiurnal

amplitude shows two well defined peaks. One is located at around 106 km with a velocity of 34 m/s, and the other one occurs at around 120 km with an intensity of 37 m/s. The intensity of semidiurnal amplitude is reduced compared with it in the previous sub-period. The large day-to-day variation and weak magnitude of semidiurnal amplitude result in a less predictable phase. As seen from Figure 3.12 (d), the phase has large variation and is stable only in the altitude range from 100 km to 110 km where the amplitude is appreciable.

The semidiurnal amplitude and phase results for the neutral wind in zonal component are shown in Figure 3.13.

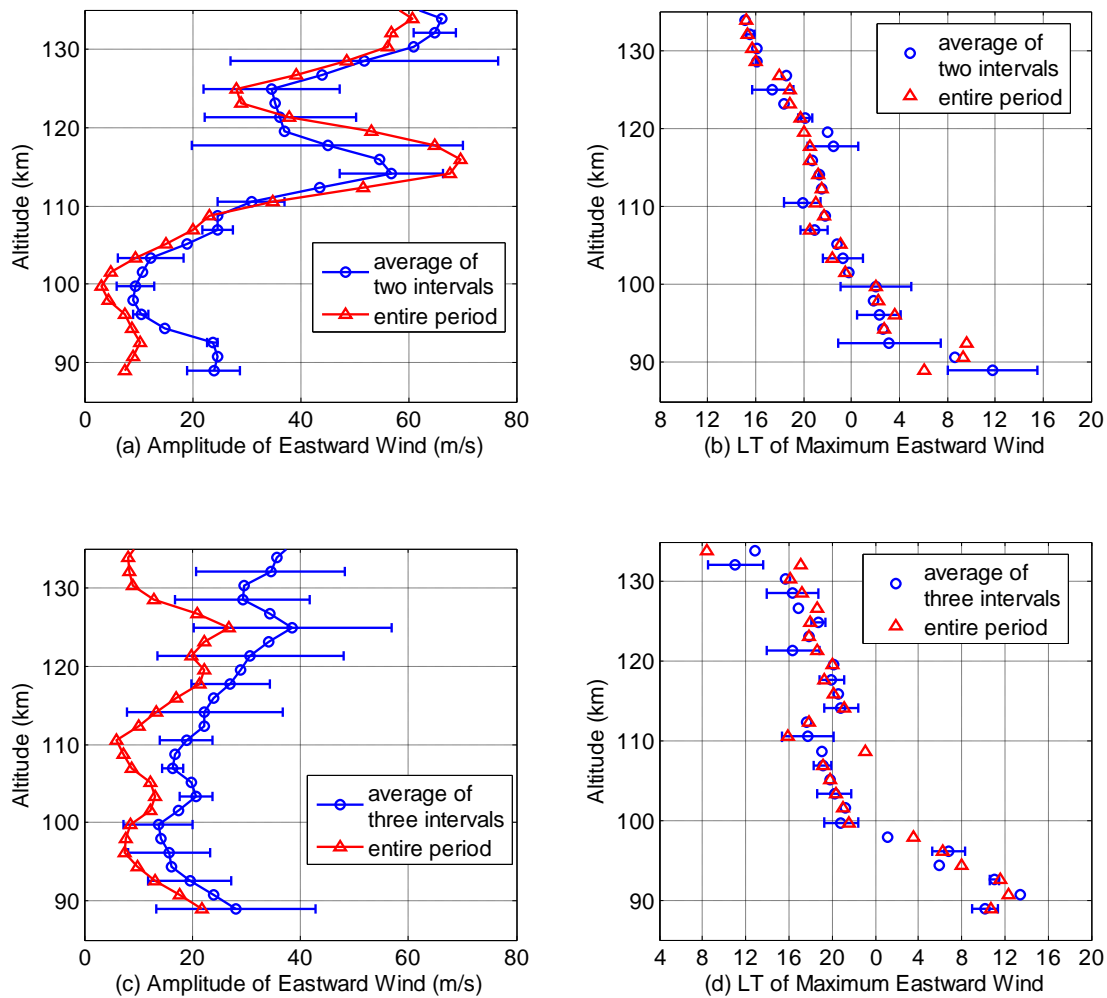


**Figure 3.13** Same as **Figure 3.9** except for semidiurnal component.

During the first sub-period, the altitude variation of semidiurnal amplitude in the zonal wind very resembles with that in the meridional wind. As shown in Figure 3.13 (a), the semidiurnal amplitude also exhibits a rapid increase in the altitude range from 100 km to 115 km with the amplitude grows from the minimum value of 3 m/s to the peak magnitude of 70 m/s. This amplitude increase shown in the zonal wind further supports that the turbopause at Arecibo in a winter time condition is about 110 km. Since the semidiurnal amplitude is prominent above 100 km, the semidiurnal phase shown in Figure 3.13 (b) is very predictable above this altitude. The vertical wavelength is determined to be 45 km. The semidiurnal amplitude in the second period, as shown in Figure 3.13 (c), is extremely attenuated compared with it in the first sub-period. The amplitude is less than 20 m/s at almost all heights. The day-to-day variation is very large above 112 km. The semidiurnal phase result during the last five days is shown in Figure 3.13 (d). Due to the weak semidiurnal amplitude during the last five days, the phase is not as consistent as it in the first sub-period. The vertical wavelength is computed about 39 km in the altitude range from 114 km to 130 km. Below 100 km, the vertical wavelength is determined as 15 km.

### **3.5 Introduction of Planetary Waves**

Large scale atmospheric planetary waves are thought to be mainly generated by dynamical and thermal effects of solar radiation and earth surface inhomogeneity in the troposphere. On the contrary to the tidal waves, the period of planetary waves is much larger than a solar day, which varies from approximate 2 days to several weeks. Periods of quasi-2, 5, 10, and 16 days planetary waves are often observed. The planetary wave can significantly influence on the background temperature, neutral winds, and distribution of ozone and it consider being responsible for the long-period atmospheric oscillation such as the quasi-biennial oscillation, and sudden stratospheric warmings [Hirota, 1980; Salby *et al.*, 1984; Canziani *et al.*, 1994; Garcia *et al.*, 2005; Pogoreltsev *et al.*, 2007; Belova *et al.*, 2009]. The investigations of planetary waves have been ongoing in both theoretical and observational ways. Salby [1981a, b] present a numerical study of the response of planetary waves in the presence of simple background wind.

Salby [1984] provided a historical overview about the planetary theory and observational support. Numerous observational studies about planetary waves have been reported via satellites [e.g., Canziani *et al.*, 1994; Garcia *et al.*, 2005], and radar techniques [e.g., Chshyolkova *et al.*, 2005; Suresh Babu *et al.*, 2011].

Since a strong quasi-2 day (40-hours) oscillation appeared in Figure 3.2 (top), this thesis focuses on the study of quasi-2 day planetary wave. The quasi-2 day wave has been studied extensively in the MLT region, and it recognized as a west propagating wave with zonal wave numbers of 3 or 4 [Suresh Babu *et al.*, 2011]. A brief introduction of early studies of quasi-2 day planetary wave is found by Suresh Babu *et al.* [2011] and references therein. However, due to the short length of ISR's consecutive observational time, only two literatures [Zhou *et al.*, 1997a; Haldoupis *et al.*, 2004] are found that studied the quasi-2 day wave using the ISR at Arecibo, and those two papers are limited at E-region. To our knowledge, this is the first time that quasi-2 day planetary is reported at F-region in a low latitude.

### 3.6 Results of Quasi-2 Day Planetary Wave

The harmonic fitting results of quasi-2 day component for the F-region meridional wind are shown in Figure 3.14.

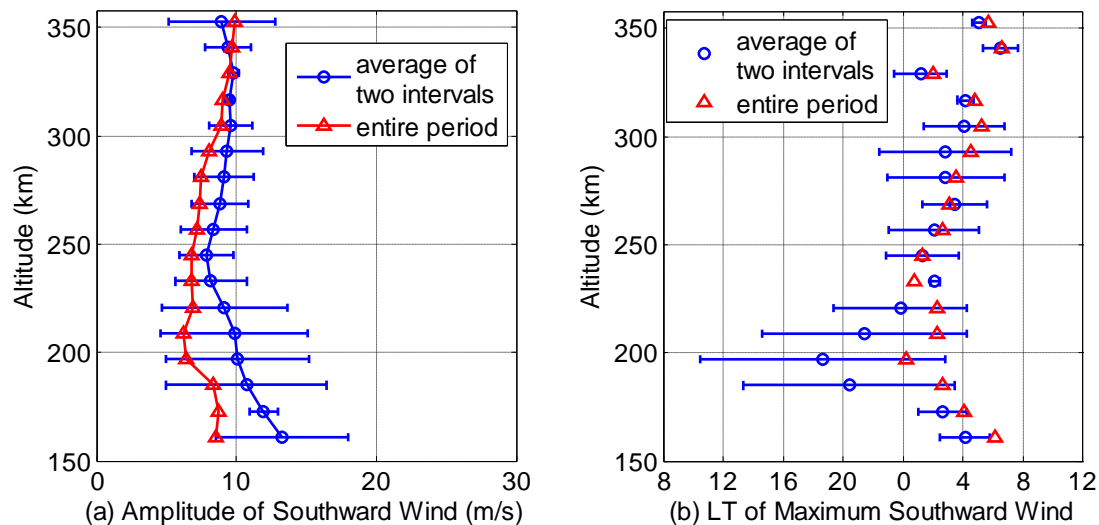


**Figure 3.14 Same as Figure 3.6 except for quasi-2 day component.**

As shown in Figure 3.14 (a), although the amplitude of the quasi-2 day wave is less than 10 m/s at all altitudes, it is comparable with that of semidiurnal tide. Day-to-day variation is large below 220 km. In Figure 3.14 (b), the phase of the quasi-2 day wave shows large discrepancy between the results derived from the entire period and averaged two subintervals in the altitude range from 180 km to 220 km. Above 220 km, the phase slope is positive, which indicates that the quasi-2 day wave propagates downward and the source region is above the altitude of interest. The vertical wavelength is estimated to be 640 km in the altitude range from 230 km to 305 km.

### **3.7 Summary and Conclusion**

Using the neutral winds deduced from the ionospheric parameters measured by the Arecibo dual beam ISR in the period of January 14-23, 2010, a comprehensive analysis of E- and F-region diurnal, semidiurnal, and quasi-2 day components are presented. The power spectral density analysis shows strong diurnal and semidiurnal harmonic oscillations in the E- and F-region heights. It also exhibits an existence of a period of approximately 40 hours planetary wave in the F-region heights. As far as we know, this is the first time that the quasi-2 day planetary wave is observed at F-region in low latitude. Based on the analysis of harmonic fitting results, the characteristics of the diurnal, semidiurnal, and quasi-2 day waves are summarized as following.

Varying from prior observational studies, the diurnal tide in the meridional wind is prominent at F-region. The observed diurnal tide in F-region is largely evanescent, which implies that it may be excited by in situ solar radiation. The results of diurnal amplitude and phase in two sub-periods are very consistent. The diurnal tide in the F-region meridional wind is very stable during nine days' observation. In E-region, diurnal tide in the meridional wind is very substantial, which supports earlier observation made by *Zhou et al.* [1997a]. During the last five days of observation, the diurnal amplitude

reaches a maximum of 70 m/s. The phases in the altitude range from 114 km to 135 km are largely constant in the first sub-period, with corresponding vertical wavelength estimated as 63 km. Below 114 km, the phase progresses linearly in both sub-periods with vertical wavelengths determined as 24 km, and 20 km, respectively. Contrary to the meridional component, diurnal tide in the zonal wind has much smaller amplitude. The day-to-day variation is very large above 120 km for both sub-periods. Below 120 km, the vertical wavelength for the second sub-period is estimated as 18 km.

In the F-region, the semidiurnal amplitude in the second sub-period is twice as large as it is in the first sub-period in the latitude range from 250 km to 310 km. In the same altitude range, the semidiurnal phases between two sub-periods differ by 180 degrees. The stronger semidiurnal oscillation observed in the second sub-period suggests that semidiurnal component gains energy from in situ absorption of solar radiation or the deposition from the dissipation of 6-, 15-, and 40-hour oscillations. In E-region, the semidiurnal tides in both meridional and zonal components are important above 110 km in the first sub-period. The semidiurnal tides show constant increase of amplitude in the altitude range from 106 km to 121 km in the meridional wind and from 100 km to 115 km in the zonal wind. The consistent amplitude increases in both components are helpful to determine the turbopause as 110 km at Arecibo in winter time. The vertical wavelengths of the meridional wind are estimated as 68 km above 112 km, and 12 km below this altitude. For the zonal wind, the vertical wavelength is determined as 45 km above 100 km. In the second sub-period, the semidiurnal amplitudes in both meridional and zonal components are reduced at above 110 km. The phases in both neutral wind components become hard to predict.

Due to the extremely dominant diurnal tide at F-region in the meridional wind, there is only a small amount of wind energy to share between the other oscillations. Although the quasi-2 day planetary wave in the meridional wind is not strong, it is comparable with the semidiurnal tide. The phase of the meridional wind in the altitude range from 230 km to 305 km suggests that the vertical wavelength is about 640 km.

# CHAPTER 4

## ANALYSIS OF HIGHER-FREQUENCY TIDAL WAVES AT ARECIBO

### 4.1 Introduction of Terdiurnal Tide

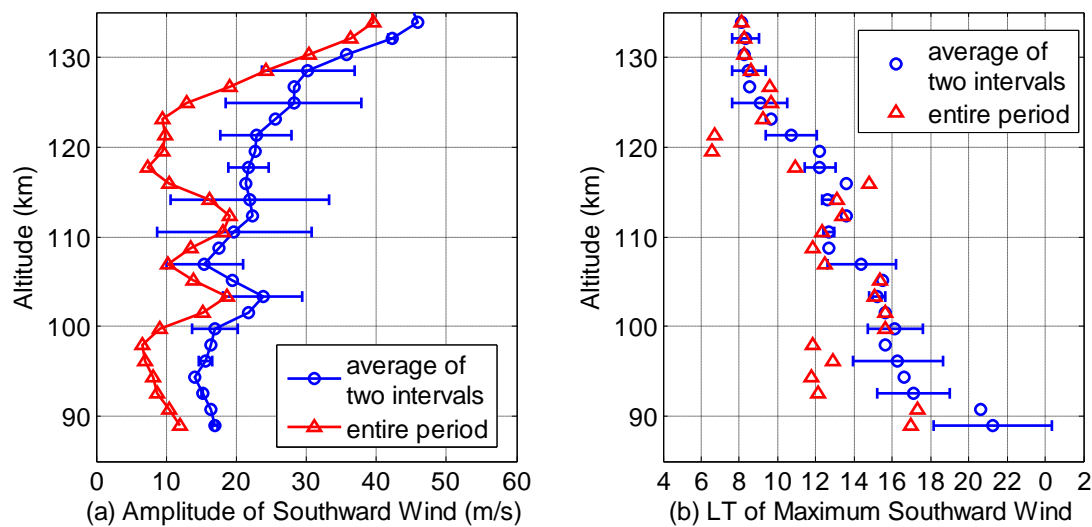
Atmospheric tides have been studied extensively both theoretically and observationally. Although most of the efforts have been focused on the diurnal and semidiurnal tides, terdiurnal tide has received increasing interests in recent years [e.g., *Du and Ward*, 2010; and references therein]. Various observational studies of terdiurnal tide by VHF meteor radars and MF radars for the MLT region are summarized by *Venkateswara Rao et al.* [2011]. Satellite observations of the migrating and nonmigrating modes and the global nature of terdiurnal tide have also been reported by *Smith* [2000] and *Forbes et al.* [2008]. In the MLT region, the amplitude of terdiurnal tide is generally smaller than but can be comparable to the diurnal or semidiurnal tide [e.g., *Zhao et al.*, 2005]. Terdiurnal tide exhibits strong latitudinal and seasonal variation. The largest amplitude occurs in late spring and early summer over the equator, in spring at low latitudes, in winter at mid-latitudes, and around autumn equinox at high latitudes [*Venkateswara Rao et al.*, 2011]. Direct solar heating, nonlinear interaction between diurnal and semidiurnal tides, and nonlinear interaction between diurnal tides and gravity waves have been suggested as the main mechanisms for the generation of terdiurnal tide by various authors [e.g., *Teitelbaum et al.*, 1989; *Miyahara and Forbes*, 1991; *Smith and Ortland*, 2001; *Huang et al.*, 2007].

Ground-based MF and meteor studies on terdiurnal tide are confined to the altitudes below 110 km and present satellite observations are limited to below 116 km. Above 116 km, ISR is the most suitable instrument to study the altitude-time dependence of the wind and temperature. Although there are numerous reports on using the ISR for the study of the diurnal and semidiurnal tides, it appears that there are only three reports containing terdiurnal tide using such a technique [*Amayenc*, 1974; *Hocke*, 1996; *Zhou et*

*al.*, 1997a]. Among the three reports, *Amayenc's and Hocke's* studies were for middle and high latitudes, respectively, while the study by *Zhou et al.* was for low latitude but limited to below 145 km. In this study, the focus is on the meridional wind at low latitude and covers the altitude range from 90 km to about 350 km. In the following, the terdiurnal tidal results are present and discussed.

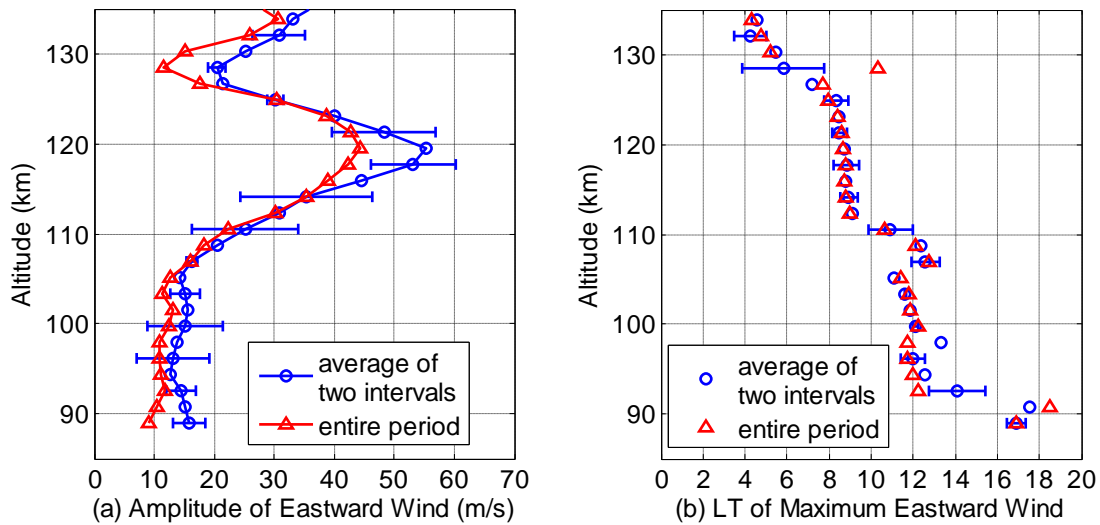
## 4.2 Results and Discussion of Terdiurnal Tide

As we can see from Figure 3.2, 3.4, and 3.5, terdiurnal tide exhibits large temporal variability in the both E- and F-regions. During the first four days of observation, terdiurnal tide in the meridional wind is weak in the F-region while it is weak in the E-region during the last five days. For the periods plotted, terdiurnal tide is among the two strongest tidal components. For the zonal component, terdiurnal tide is very strong during the first four days in the altitude from 110 km to 130 km. Although the terdiurnal tide is largely attenuated during the last five days, it still among the two strongest tidal components during the last five days in that altitude range. Figure 4.1 shows the fitting results for the meridional wind amplitude and phase of terdiurnal tide in the E-region.



**Figure 4.1** Same as Figure 3.6 except for E-region terdiurnal tide.

As shown in Figure 4.1 (a), in the E-region, amplitude grows continuously from 120 km to 135 km, where the peak amplitude occurred with a magnitude of 40 m/s. The phase in the upper peak region of 121 km to 135 km shows linear downward progression with a vertical wavelength of about 74 km. The phase in the lower peak region of 110 km to around 120 km, however, is largely stationary. The vertical wavelength is expected to increase as the wave propagates upward because of increasing dissipation [e.g., *Forbes, 1995*]. The different phase and amplitude characteristics below and above 121 km imply either a drastic change in the propagation mode or the existence of a significant terdiurnal tidal source. Below 100 km, the temporal phase variation becomes very large, resulting in a much smaller overall amplitude. The amplitude and phase results for the zonal component are shown in Figure 4.2.



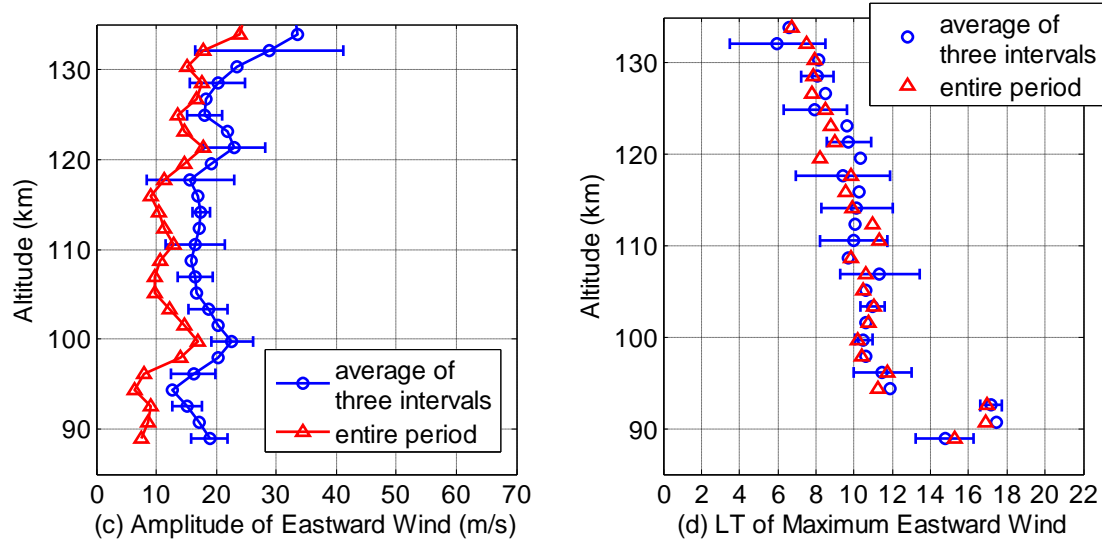


**Figure 4.2** Same as **Figure 3.9** except for terdiurnal component.

As shown in Figure 4.2 (a), the amplitude in the first four days is prominent in the altitude range from 110 km to about 130 km. The peak amplitude is 44 m/s appeared at around 120 km. The phase in the altitude range from 112 km to 127 km, and from 92 km to 105 km appears to be consistent. In both altitude ranges, the terdiurnal phases show a slow downward progression, and corresponding vertical wavelength is estimated as 100 km, and 128 km, respectively. During the last five days, the amplitude is considerably reduced in the altitude range from 110 km to 125 km compared with that in previous sub-period. The phase exhibits a downward linear progression above 95 km. The vertical wavelength is determined as 81 km.

Harmonic fitting results of terdiurnal tide in the F-region during Jan. 18-23 are shown in Figure 4.3.

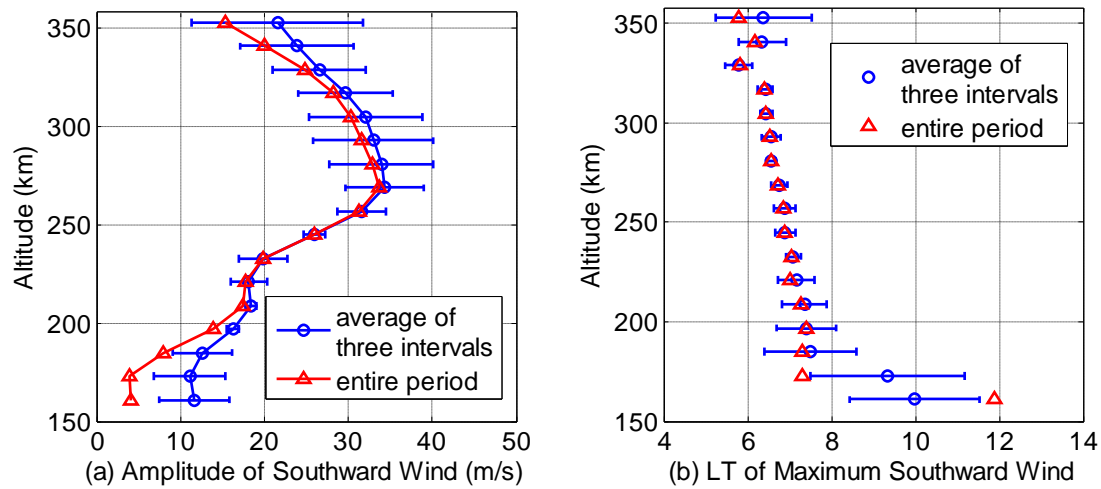


**Figure 4.3** Same as **Figure 3.7** except for terdiurnal tide.

The terdiurnal amplitude is prominent ( $> 15$  m/s) in the 200-350 km altitude range and the largest amplitude occurs at 268 km. The average from the three intervals is larger than the fitting result using the entire five days' data because phase variation within the fitting interval reduces the amplitude result. This is reflected in the phase plot as well. In the altitude range of 200 to 320 km, the temporal variability of the phase is small and the altitude variation is largely linear. The overall vertical wavelength in this region is 950 km.

Since the F-region terdiurnal tide at low latitudes has not been reported previously, the following discussion is focus on this region. As mentioned in the introduction, three mechanisms have been thought to be mainly responsible for the generation of terdiurnal tide: 1) the third harmonic of the diurnal solar heating; 2) nonlinear interaction between diurnal and semidiurnal tide; and 3) nonlinear interaction between diurnal tide and gravity waves. The third mechanism is thought to be weaker than the first two and may contribute to 5 m/s or less in the amplitude in the MLT region [Miyahara and Forbes, 1991]. Although observational result from a single location is necessarily the summation of all possible mechanisms, the importance of the 2<sup>nd</sup> mechanism has been assessed by comparing terdiurnal tide with the diurnal and semidiurnal tides [e.g., Venkateswara Rao

*et al.*, 2011 and references therein]. Non-linear interaction is regarded to be important if there is a high degree of correlation between terdiurnal tide and either of the other two tides. However, using the amplitude correlation as an indicator to demonstrate the dominance of nonlinear interaction is problematic since the solar driven mechanism may enhance all three tides at the same time, as pointed out by *Venkateswara Rao et al.* [2011]. A more critical test to delineate the two mechanisms lies in examining the phase variation.

To compare the three tidal components, the amplitude and phase variations of the diurnal, semidiurnal, and terdiurnal tides at 268 km are shown in Figure 4.4.

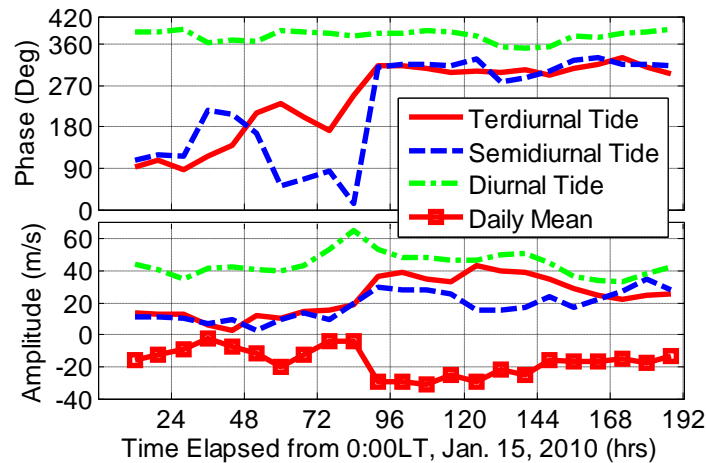


**Figure 4.4 Phase and amplitude variations of terdiurnal, semidiurnal, and diurnal tide at 268 km as a function of time. The terdiurnal, semidiurnal, and diurnal tide are represented by a solid, a dashed, and a dash-dot line, respectively. The line with square symbols in represents the mean wind averaged from 185 to 233 km. Zero degree in phase corresponds to maximum southward wind occurring at 0:00 LT.**

Each data point is obtained using a 24-hour window centered at the time indicated by the abscissa. As seen from Figure 4.4, during the first four days of observation, terdiurnal tidal amplitude is typically smaller than 10 m/s and the phase exhibits a very large temporal variation, suggesting a very weak or non-existent terdiurnal tide. During the

last five days, the amplitude is increased dramatically and remains above 30 m/s most of the time. The phase of terdiurnal tide during the last five days of observation is far more stable than the first four days. During the entire period, the diurnal tide is the strongest component. When terdiurnal tide was strong during Jan. 18-23, the amplitude of terdiurnal tide is not correlated with those of the diurnal and the semidiurnal tides even though the long term variations of the three components appear to be correlated.

To further assess the potential importance of nonlinear interaction, comparisons among the vertical wavelengths of the three tidal components are necessary. The phase of the diurnal tide is largely stationary (with a slight upward tilt) while the vertical wavelengths of the semidiurnal and terdiurnal tides are about 300 and 950 km, respectively. Those vertical wavelengths do not satisfy the nonlinear triad interaction relationship. We further note that if nonlinear interaction between diurnal and semidiurnal tides is important, it would generate a secondary diurnal tide as well. Since the terdiurnal and semidiurnal tides are rather weak during Jan. 14-18, nonlinear interaction is not expected to be strong during this time interval and the observed diurnal tide should largely be the primary component. On the other hand, if the observed terdiurnal tide during Jan. 18-23 were produced by nonlinear interaction, a secondary diurnal component would have been produced as well and the observed diurnal tide would be the superposition of the primary and the secondary components. As a result, the phase of the observed diurnal tide is expected to be different during the two periods if nonlinear interaction were important. Observation does not show any appreciable change in the phase of the diurnal tide during the entire period. Comparisons of the amplitudes, vertical wavelengths and phase variation thus do not reveal nonlinear interaction between the diurnal and semidiurnal tides as the source for terdiurnal tide observed. Further, the strong phase stability of terdiurnal tide, when its amplitude is appreciable, suggests that nonlinear interaction with gravity waves is not likely an important mechanism responsible for terdiurnal tide either.

Another issue involving the origin of terdiurnal tide is whether it is generated via in-situ thermospheric heating or it is propagated upward from below. The theoretical study by *Hagan et al.* [2001] indicates in-situ solar driven tide is largely evanescent for

diurnal and semidiurnal tides in the thermosphere. Although there is no such study on terdiurnal tide, in-situ solar driven terdiurnal tide is expected to be evanescent as well because the solar heating source in the thermosphere lacks phase progression. Terdiurnal tide shows clear phase progression in our observation. Although the phase progression is more consistent with a propagating mode, it is noted that the phase change in local time is only about one hour from 200 to 300 km. Such a small change in phase makes it hard to draw a firm conclusion on whether the observed terdiurnal tide is mainly generated in-situ or propagated from below. Further, it should be borne in mind that our observation was done at a single location. All the tides reported here are the combined effects of migrating and non-migrating components. Our discussion and conclusion pertain only to the strongest component and we cannot ascertain the observed tides are mainly migrating or non-migrating.

The F-region terdiurnal tide exhibits strong temporal variability as indicated in Figure 4.4. The relation between background wind and tidal amplitude has been studied extensively in the MLT region [e.g., *Deepa et al.*, 2008; and references therein]. *Deepa et al.* [2008] reports that the diurnal tide amplitude in the MLT region is highly impacted by the background wind in the lower region. In our observation, it appears that thermospheric terdiurnal tide is strongly affected by the mean meridional wind. In Figure 4.4, the line with square symbols represents the mean meridional wind averaged from 185 to 233 km. As seen in this figure, terdiurnal tidal amplitude and the mean wind below are well correlated. Larger daily mean southward wind corresponds to larger terdiurnal tidal amplitude. The strong daily meridional mean wind variation can be caused by planetary waves. The fact that the condition in the lower-region strongly affects the F-region terdiurnal tide is indicative that the F-region terdiurnal tide has a strong propagating component. Since tides propagate in the zonal direction, zonal mean wind directly affects tidal wave propagation. If the terdiurnal tide variability is due to zonal mean wind, it is likely strongly coupled to the meridional wind.

### 4.3 Summary and Conclusion

The power spectral density analysis and harmonic fitting results show that the amplitude of the terdiurnal tide is among the two strongest tidal components for most of the E and F-region heights. In the E-region, the terdiurnal tide in the meridional wind between the 110 km to 120 km altitude range exhibits different propagating characteristics from the regions above and below. In the zonal component, the terdiurnal tide is very strong during Jan. 14-18. The peak amplitude is 44 m/s at around 120 km.

To our knowledge, this is the first time that the terdiurnal tide has been reported in the F-region at low latitudes. Major characteristics of the F-region terdiurnal tide include:

- The terdiurnal tide shows large temporal variability in amplitude. The phase, on the other hand, shows little temporal variability when the amplitude is appreciable. The daily amplitude can change from negligible to over 40 m/s in the F-region in a matter of few days. The amplitude variation appears to be correlated with the change in the mean wind in the lower F-region.
- The vertical amplitude profile is single peaked with the peak altitude at about 270 km. The phase in the region of 180 to 320 km is largely linear. The vertical wavelength is about 950 km.
- The amplitude of the F-region terdiurnal tide is mostly smaller than that of the diurnal tide but somewhat larger than that of the semidiurnal tide.

Above study clearly indicates that the terdiurnal tide is as important as the commonly recognized diurnal and semidiurnal tides both at the E- and F-region heights. The observed characteristics suggest that nonlinear interaction is likely not important for the generation of the F-region terdiurnal tide.

## 4.4 Results and Discussion of 6-hour Tide

Several studies have been reported the existence of 6-hour tide in the middle and higher latitudes based on radar [Kovalam and Vincent, 2003; Smith et al., 2004], lidar [She et al., 2002], and airglow techniques [Sivjee and Walterscheid, 1994; Walterscheid and Sivjee, 1996, 2001]. In lower latitudes, using the Arecibo ISR, Tong et al. [1988] and Morton et al. [1993] hypothesized the existence of 6-hour tide. Zhou et al. [1997a] reported the existence of a 6-hour tide in the altitude range from 94 km to 143 km based on the observation of two winter days. The periodogram shown in Figure 3.2 (top) suggest that a 6-hour oscillation is existed during the first four days of observation (Jan. 14-18, 2010). The harmonic fitting results of 6-hour oscillation in the meridional wind are shown in Figure 4.5.

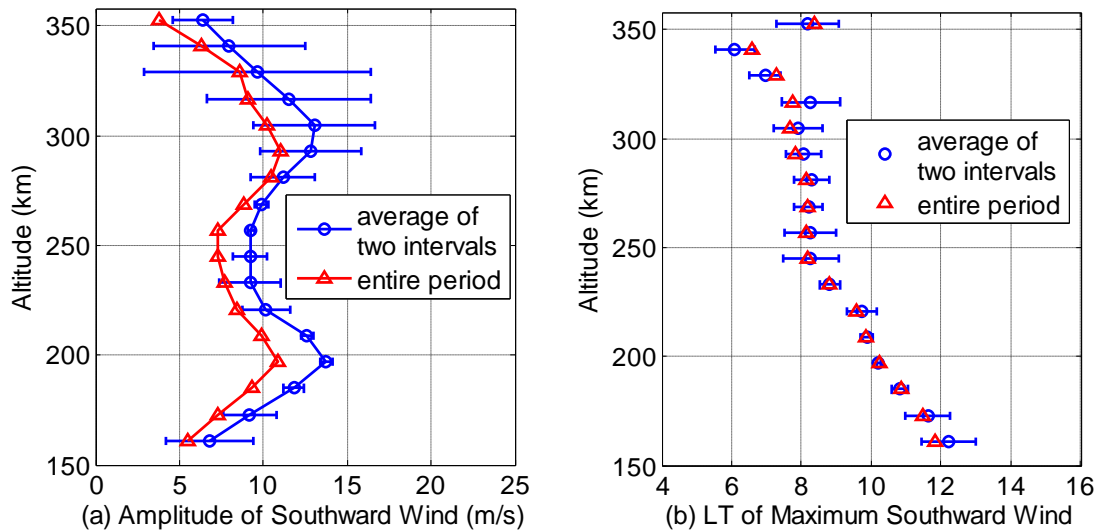


**Figure 4.5** Same as Figure 3.6 except for the 6-hour component.

As shown in Figure 4.5 (a), amplitude of 6-hour oscillation exhibits two peaks located at around 200 km and 290 km, respectively. The magnitudes for both peaks reach about 11 m/s. In the altitude range from 180 km to 280 km, the amplitude variation is very small. The phase of 6-hour component, as shown in Figure 4.5 (b), shows two distinct regions of progression. Above 245 km, the phase is largely constant. Below that altitude, the phase

exhibits linear downward progression with an estimated vertical wavelength of 126 km. The phase features may indicate that 6-hour component is a propagating tide, and its source is located at lower altitude.

However, it should be noted that observed 6-hour oscillation may not necessary be a tidal wave. It could be a gravity wave or a combination of tidal and gravity waves. The most significant difference between tidal and gravity waves is that the phase of tidal wave is coherent while the phase of gravity wave is largely irregular. Another difference is that tide is a global structure while gravity wave is a local structure. Since the data is collected from a single station, the second difference cannot be verified in this study. Two evidences showed in Figure 4.5 (b) supports that the observed 6-hour oscillation has phase coherence. Firstly, the interval-to-interval variation is very small. In addition, the phase results between entire period and averaged subintervals are very consistent. In order to further examine the phase variation of observed 6-hour oscillation, amplitude and phase variations of 6-hour component at 196 km is shown in Figure 4.6.

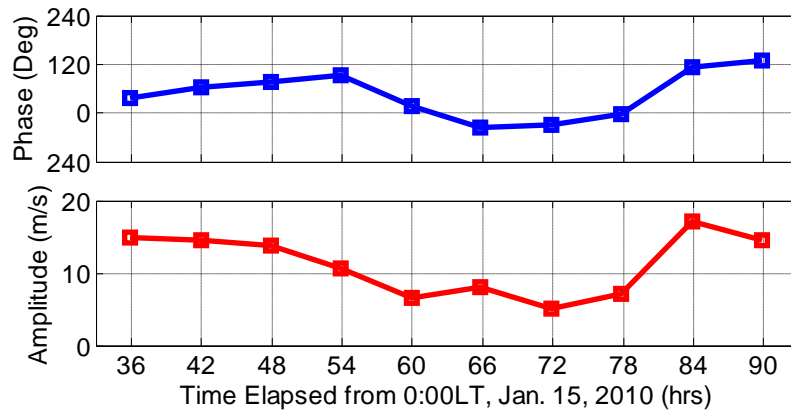


**Figure 4.6 Phase and amplitude variations of 6-hour oscillation at 196 km as a function of time. Zero degree in phase corresponds to maximum southward wind occurring at 0:00 LT.**

Like Figure 4.3, each data point is derived by using a 24-hour window. As shown in Figure 4.6, the phases of 6-hour oscillation are very coherent in the time ranges of 36-hour to 54-hour, and 60-hour to 78-hour, respectively. The strong phase coherent

observed from Figure 4.5 and 4.6 suggest that the observed 6-hour oscillation is a tidal component.

# CHAPTER 5

## MIDNIGHT IONOSPHERE COLLAPSE AT ARECIBO AND ITS RELATIONSHIP TO THE NEUTRAL WIND, ELECTRIC FIELD, AND AMBIPOLAR DIFFUSION

### 5.1 Introduction

One of the most prominent ionospheric features observed over Arecibo, Puerto Rico (18.3°N, 66.7°W) is the so called midnight collapse phenomenon. Midnight collapse is characterized by a rapid drop of F<sub>2</sub> layer peak height (HmF<sub>2</sub>) around midnight, which is often accompanied by a decrease in F-region peak concentration (NmF<sub>2</sub>). *Nelson and Cogger* [1971] have reported statistical results of midnight collapse based on 130 nights of incoherent scatter radar (ISR) data collected at Arecibo between October 1965 and June 1969. The results show that HmF<sub>2</sub> descends 50 to 100 km in 85 percent of the nights near midnight. This conspicuous phenomenon has been extensively studied using ISR [*Behnke and Harper*, 1973; *Harper*, 1979; *Macpherson et al.*, 1998; *Seker et al.*, 2009], airglow techniques [*Nelson and Cogger*, 1971; *Vlasov et al.*, 2005], and theoretical models [*Crary and Forbes*, 1986]. *Behnke and Harper* [1973], *Macpherson et al.* [1998], and *Vlasov et al.* [2005] reported the reduction and reversal of the prevailing equatorward neutral wind being the cause of the midnight collapses they observed. The reversal of meridional winds is thought to be due to the pressure bulge associated with the midnight temperature maximum [*Colerico et al.*, 1996; *Seker et al.*, 2009]. *Crary and Forbes* [1986], using numerical simulations, and *Harper* [1979], using two nights of ISR observation, attributed the collapse to the shear in the meridional wind associated with upward propagating semidiurnal tide. All the authors mentioned above suggest that the dynamic of the neutral wind above Arecibo plays a dominant role in causing the midnight collapse even though ambipolar diffusion is considered in some of the modeling studies [e.g., *Vlasov et al.*, 2005].

Generally speaking, the effect of the meridional wind appears to be stronger than that of the electric field in modifying the vertical profile of the F-region ionosphere at mid-latitudes [Vasseur, 1972], while at geomagnetic equatorial locations, electric field seems to be more important [Woodman, 1970]. Because of the unusual location of the Arecibo Observatory, 30° N geomagnetic and 18.3° N geographic, one would expect that the behavior of the ionosphere, including the midnight collapse, is controlled both by the neutral wind and electric field. In this paper, we use the Arecibo dual-beam ISR to investigate the relationship between the nighttime F-layer morphology and vertical ion motion associated with the meridional wind, electric field and ambipolar diffusion during the period of January 14-23, 2010 and December 3-5, 2002.

In the following, we present observation of the ionospheric morphology and various vertical velocities during Jan. 14-22, 2010 in Section 2. During the nine nights of observation, the behaviors of the first four nights (Jan. 14-17) were very different from those of the last five nights. In Section 5.3, we discuss the underlying cause(s) for the midnight collapses. We further decompose the meridional winds into various tidal components and examine their effects on midnight collapse. Results and conclusions are summarized in Section 5.5.

## **5.2 Data Presentation**

### **5.2.1 Electron Density Distribution at Arecibo**

The electron concentration during the Jan. 2010 observation is shown in Figure 5.1. The daytime HmF2 is low because of the large downward ion motion, which is typical of the winter condition [Zhou and Sulzer, 1997b; Isham et al., 2000]. For the purpose of the present study, we will focus only on the nighttime period. For all the nights, we see that HmF2 drops substantially after midnight. This is typical of the nighttime ionosphere at Arecibo, the midnight collapse.

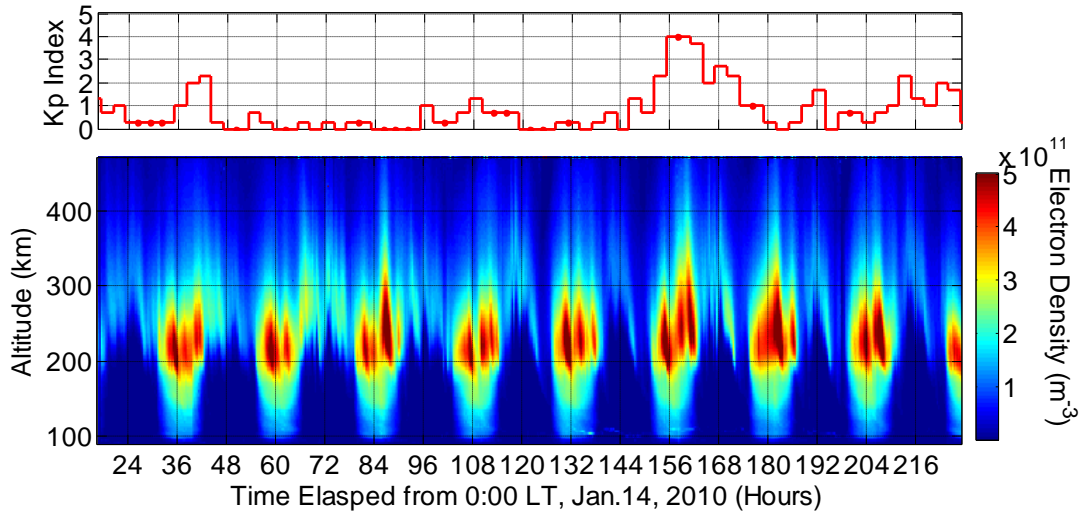


**Figure 5.1 Arecibo height-and-time electron density distribution during 16:30 LT Jan. 14 to 11:10 LT Jan. 23, 2010. The top plot shows the  $K_p$  index variation as a function of time.**

Although the ionosphere descended on all nights after midnight, the descents in the last five nights (after 108 hours) were more persistent and dramatic than the first four nights. For convenience, the night starting in the evening of Jan. 14 will be referred to as the night of Jan. 14. We will also refer to the four consecutive nights of Jan. 14-17 as the first four nights or first interval, and the five nights of Jan. 18-22 as the last five nights or the second interval. To illustrate the differences between the two intervals, we plot, in Figure 5.2(a) and (b), the daily averages of the plasma frequency for the two intervals, respectively. Plasma frequency ( $f_p$  in MHz) is related to the electron concentration ( $n_e$  in  $\text{cm}^{-3}$ ) via  $n_e = 1.24 \times 10^4 f_p^2$ .

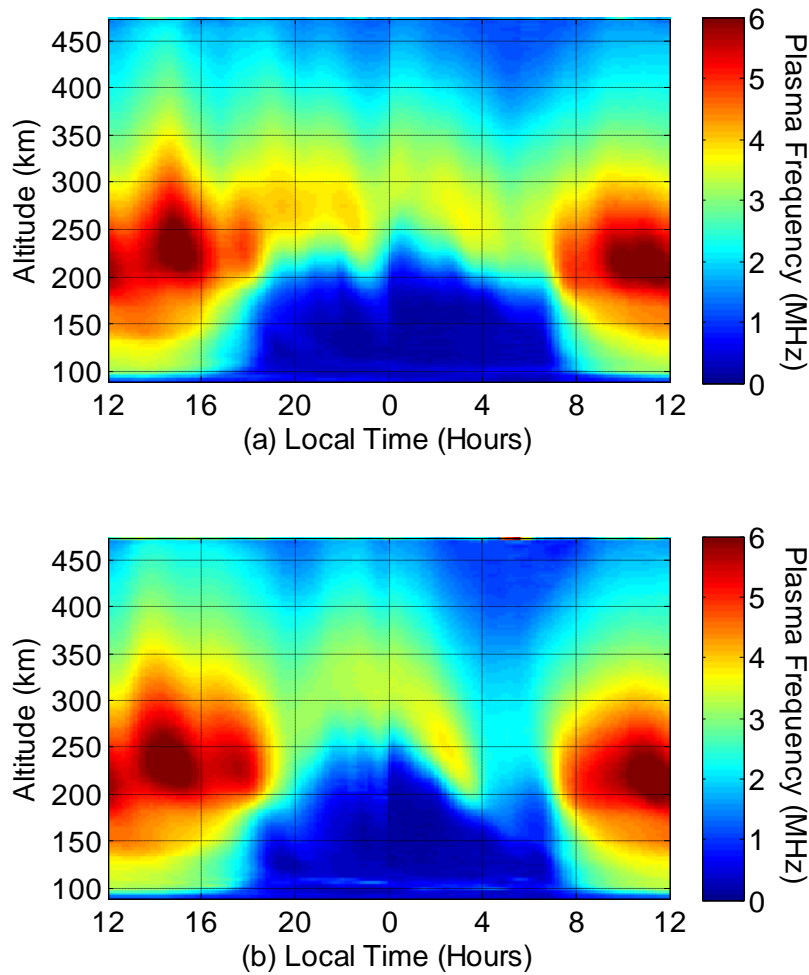


**Figure 5.2** Arecibo height-time variation of plasma frequency (MHz) averaged within the 24-hour window, (a) four days from 16:30 LT Jan. 14 to 7:23 LT Jan. 18, 2010; (b) five days from 9:55 LT Jan. 18 to 11:10 LT Jan. 23, 2010. (The radar was not operational during 7:23-9:55 LT on Jan. 18.)

Since the plasma frequency compresses the scale of variation, nighttime structure is better revealed. One difference between the two intervals, as seen from Figure 5.2, is that the ionosphere in the second interval descended much faster than in the first interval. Another difference is that the decrease in electron concentration after midnight is more pronounced in the second interval. One objective of this study is to understand the underlying causes for the differences. In the following, we will mostly focus on the average behaviors of the two intervals, instead of on the individual days. Such an

approach makes it easier to see more clearly the underlying dynamics associated with midnight collapse despite that there are considerable day-to-day variability within each interval, especially the first one.

### 5.2.2 HmF2, NmF2 and $V_z$

Because of the lack of production and the relatively slow chemical recombination above approximately 250 km, the nighttime F-region vertical electron distribution is controlled by vertical transport to a great extent. It is thus expected that the motion of HmF2 is closely related to the vertical ion drift. The nighttime variation of HmF2 and vertical ion drift (upward positive, denoted as  $V_z$ ) are shown in Figure 5.3.

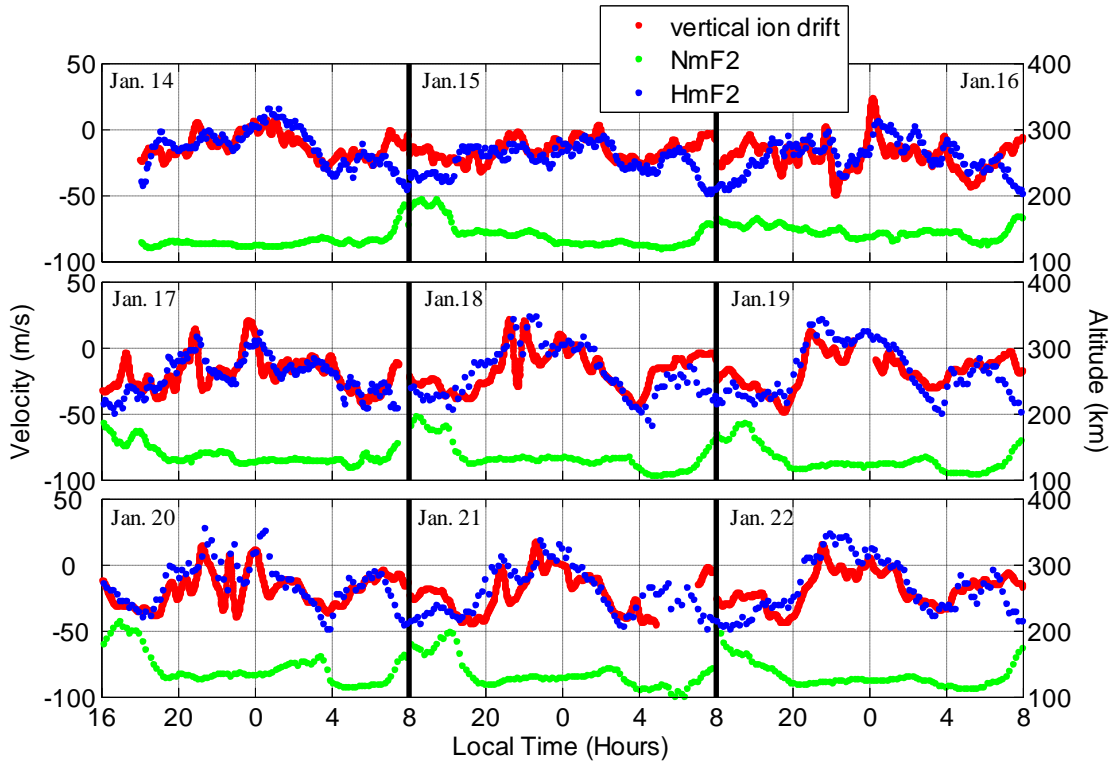


**Figure 5.3** Vertical ion drift at 268 km (red dots), HmF2 (blue dots), NmF2 (green dots) derived from the Arecibo dual-beam ISR during 16:30 LT Jan. 14 to 11:10 LT Jan. 23, 2010. In order to better examine the nighttime part, only local time ranging from 20:00 LT to 8:00 LT next day is presented. Solid black lines serve as

**demarcation of different nights. For electron density, the scale of 100-200 km on the altitude axis corresponds to  $0 - 5 \times 10^{11}$  electrons/m<sup>3</sup>.**

The electron concentration at the peak altitude of the F<sub>2</sub> layer, NmF<sub>2</sub>, is also plotted. The vertical ion drift is chosen to be at 268 km, about the average height of nighttime HmF<sub>2</sub>. As can be seen from the plot, the variation of HmF<sub>2</sub> is closely correlated to the variation of the vertical ion drift. The close correlation between  $V_z$  and HmF<sub>2</sub> breaks down at sunrise because of rapid production of ions.

One prominent feature in Figure 5.3 is the consistence of rapid descent in HmF<sub>2</sub> and the acceleration of downward vertical ion drift from Jan. 18 to 23 between 0 - 4:00 LT. For all the last five nights, large negative velocities were observed at ~4:00 LT, which coincided with the lowest HmF<sub>2</sub> value of each night. Despite the large variations in HmF<sub>2</sub> and  $V_z$  from 20:00 to 3:30 LT, the variation of NmF<sub>2</sub> remained modest and was not synchronized with those of the two other parameters. In fact, during the time interval from 20:00 to 3:00 LT, NmF<sub>2</sub> showed a slight increase irrespective of the change in HmF<sub>2</sub> during the last five nights. A sharp drop in NmF<sub>2</sub> started at ~3:30 LT and lasted to ~4:00 LT when the HmF<sub>2</sub> was at about 220 km. This indicates that chemical recombination becomes more important below 220 km. In the first four nights, the descent in HmF<sub>2</sub> after midnight does not have a consistent pattern. The sharp drop in NmF<sub>2</sub> between 3:30 to 4:00 LT seen in the last five nights was largely absent in the first four nights when the HmF<sub>2</sub> was about 250 km. During the entire observational period, the geomagnetic activity, as indicated by  $K_p$  in Figure 5.1, was low except on Jan.20, when  $K_p$  reached 4.0. Although  $V_z$  showed rapid fluctuation before midnight on Jan. 20, it is not clear whether this was related to the modest geomagnetic activity. In any event, the behaviors of HmF<sub>2</sub>, NmF<sub>2</sub>, and  $V_z$  during collapse on Jan. 20 did not show obvious deviation from the two nights before and two nights after.

In Figure 5.4, we plot the daily averaged HmF<sub>2</sub>,  $V_z$  and peak electron concentration NmF<sub>2</sub> for the two intervals as defined above. The vertical ion velocity presented in Figure 5.4 is at the altitude of HmF<sub>2</sub>.

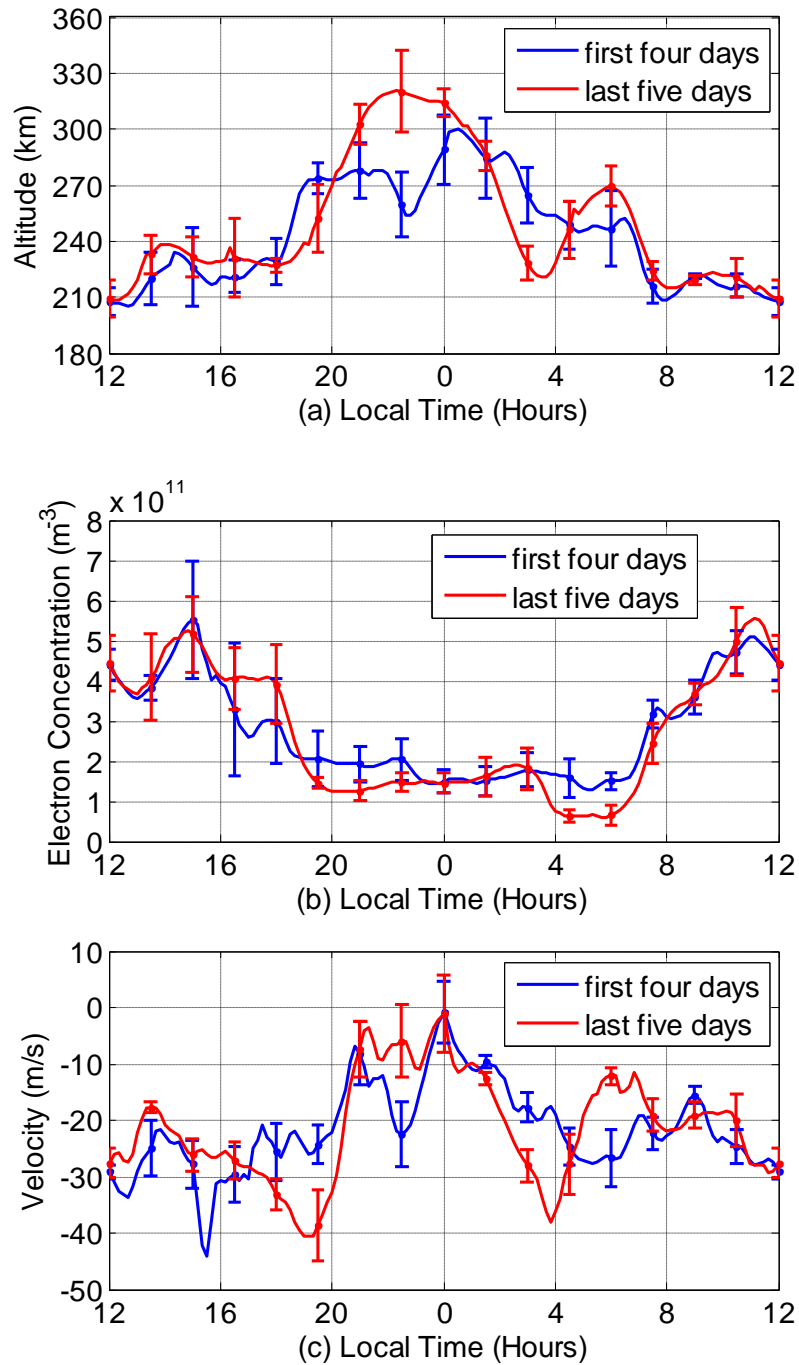


**Figure 5.4 Average HmF2 (a), NmF2 (b) and VzF2 (c) for the nights of Jan. 14-17 (blue) and Jan. 18-22 (red). The error bars are the day-to-day variation during the averaging period.**

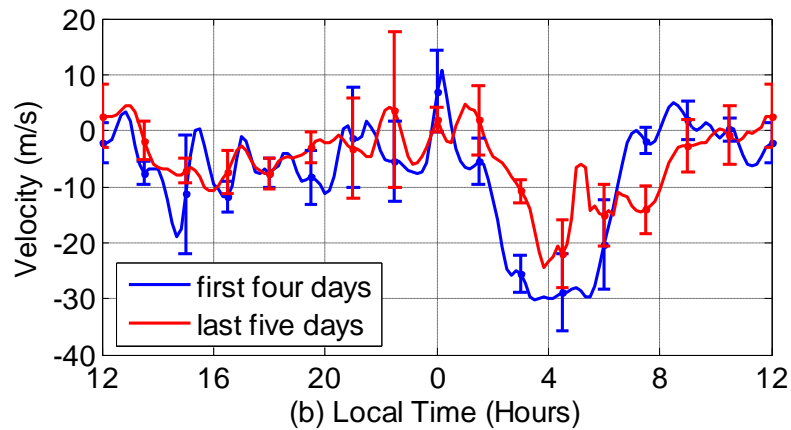
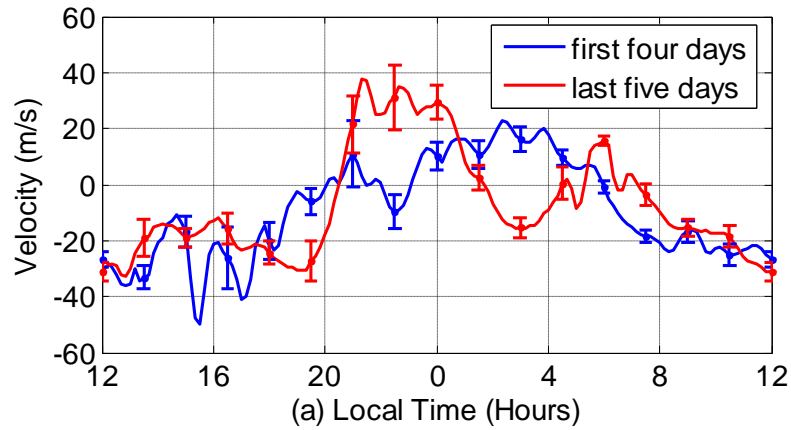
In Figure 5.4(a), we see that rapid drops of HmF<sub>2</sub> could occur before midnight but the total extent of these drops was less than 50 km after averaging 4-5 nights. The averaged HmF<sub>2</sub> dropped persistently from about midnight to 4:00 LT in both intervals. This midnight collapse is our main focus here. During the more prominent collapse of the second interval, HmF<sub>2</sub> descended at a steep rate of 30 km/hour (~8 m/s) from midnight until 4:00 LT to a very low altitude of about 215 km. This descent was accompanied by a constant downward acceleration of ~9 m/s/hr. It is interesting to note that the linear relationship between the apparent velocity of HmF<sub>2</sub> and the acceleration of downward vertical velocity applies to a fairly large altitude range from 215 km to 315 km. Although HmF<sub>2</sub> in both intervals shows a fast drop at 7:00 LT, this is because of the sunrise effect, as can be seen in Figure 5.2 and will not receive further attention.

The HmF<sub>2</sub> variations during the midnight collapse period are consistent with the vertical ion velocities of the two intervals. Other than the fact that the vertical ion velocity was more negative during the more severe collapse in the second interval, there was also a significant difference in ion velocity between the two intervals before midnight. The magnitude of the downward ion drift during the second interval before midnight was far smaller than that during the first interval. Since the ionosphere during the second interval was not pressed downward as hard as during the first before midnight, this was consistent with a higher HmF<sub>2</sub> during the second interval. As discussed in the next section, the HmF<sub>2</sub> prior to the collapse plays a key role on the extent of the collapse. Although our focus here is on HmF<sub>2</sub>, it is of interest to note that NmF<sub>2</sub> increases from midnight to 3:00 LT despite that HmF<sub>2</sub> falls sharply in the second interval. This indicates that a large amount of electrons are transported downward from the plasmasphere. A more detailed discussion on the downward transport of electrons along the plasma tube is discussed by *Vlasov et al.* [2005].

### 5.2.3 Components of Vertical Motion

As seen from above, the acceleration of downward vertical ion drift around midnight coincides with the initiation of the midnight collapse. The vertical ion motion

can be considered to be composed of perpendicular ( $V_{pn}$ ) and parallel ( $V_{ap}$ ) to the geomagnetic field ( $\mathbf{B}$ ) components. The eastward electric field is responsible for  $V_{pn}$  via the  $\mathbf{E} \times \mathbf{B}$  mechanism. The vertical component due to electric field,  $V_{z_{pn}}$ , is  $V_{pn} \cos I$ , about  $0.7V_{pn}$  at Arecibo. The parallel to  $\mathbf{B}$  component is due to both meridional wind and ambipolar diffusion. The vertical ion drift due to meridional wind,  $V_{z_{us}}$ , is  $U_s \sin(2I)/2$ , about  $0.5U_s$  at Arecibo, where  $U_s$  is the southward wind. In Figure 5.5, we plot the averaged vertical ion drifts due to neutral wind, electric field, and ambipolar diffusion. The vertical velocities shown in Figure 5.5 are at the F-region peak altitude as in Figure 5.4.



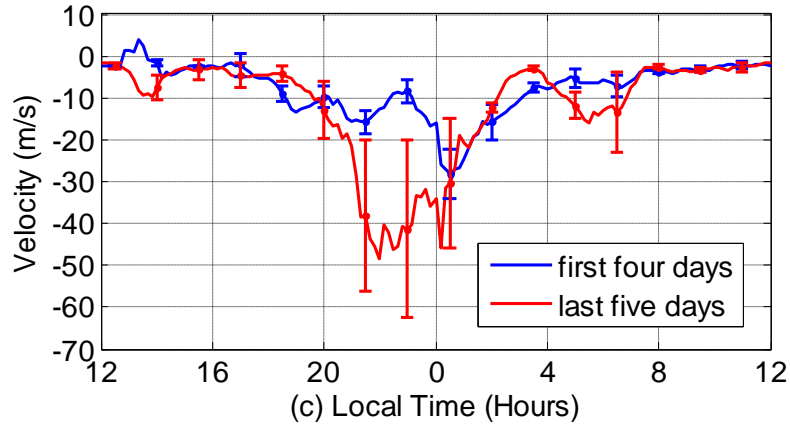


**Figure 5.5 Average  $V_{z_{us}}$  (a),  $V_{z_{pn}}$  (b) and  $V_{z_d}$  (c) for the nights of Jan. 14-17 (blue) and Jan. 18-22 (red). All the component vertical velocities are presented at HmF2 altitudes.**

During the nighttime, the vertical ion drifts due to meridional wind of the two periods showed opposite trends, as seen from Figure 5.5(a). In the first interval,  $V_{z_{us}}$  had a small amplitude prior to 23:00 LT and became upward (corresponding to an equatorward neutral wind) afterward with the largest amplitude occurring at 2:00 LT. During the second interval, the meridional wind induced vertical drift showed a much larger fluctuation.  $V_{z_{us}}$  was persistently large at about 30 m/s between 21:00 - 1:00 LT prior to the collapse. Persistent downward acceleration lasted from midnight to 3:00 LT.

For the vertical drift induced by the electric field, the largest difference between the two intervals occurred after midnight during the collapse period as shown in Figure 5.5(b). The very large downward velocity due to the electric field in the first interval was able to overcome the upward velocity resulted from the meridional wind. However, since the overall downward ion velocity was not very large in the first interval, the corresponding midnight collapse was modest.

The ambipolar diffusion velocity at the F-region peak, as shown in Figure 5.5(c) is largely dictated by the plasma scale height term, because the gradient of the electron density is zero at HmF<sub>2</sub> and the gradients of electron and ion temperatures are small. For

this reason, the vertical projection of the ambipolar diffusion velocity,  $V_{z,d}$ , is always negative (downward). The larger downward drift in the first interval before midnight corresponds to a higher HmF<sub>2</sub>, as shown in Figure 5.4(a).

## 5.3 Discussion

### 5.3.1 What mechanism is most responsible for the midnight collapse?

The direct cause of nighttime change in HmF<sub>2</sub> is due to vertical transport. The most consistent downward motion throughout the night, as seen from Figure 5.5, is due to ambipolar diffusion. If there is no contribution from the electric field and neutral wind, the neutral state of the ionosphere is to move downward as a result of the ambipolar diffusion. However, because of faster chemistry at lower altitude, HmF<sub>2</sub> will cease to go downward at a certain altitude due to just ambipolar diffusion. For the Jan. 2010 observation, we see that the diffusion-chemistry equilibrium HmF<sub>2</sub> height is about 275 km. This is observed at 21:00 LT during the first interval when the summation of  $V_{z,us}$  and  $V_{z,pn}$  is approximately zero. Although diffusion can move the ionosphere, it can only do so when the diffusion-chemistry equilibrium is broken by other mechanisms. For a constant  $V_{z,us}+V_{z,pn}$ , a new equilibrium HmF<sub>2</sub> will be established. As seen from Figure 5.3 and 5.4, the apparent motion of HmF<sub>2</sub> generally correlates very well with the time derivative of  $V_z$  ( $dV_z/dt$ ), instead of  $V_z$ . This indicates that a new equilibrium height is reached within a short period of time.

Midnight collapse occurred during all the nine nights of observations at various degrees. In the first four nights, the descent of HmF<sub>2</sub> between midnight and 1:30 LT was driven by diffusion. During this period, the neutral wind pushed the ions upward while the electric field pushed the ions downward with a relatively small magnitude. Between 1:30 and 4:00 LT,  $V_{z,pn}$ , reaching a very large amplitude at -30 m/s, played the dominant role to push down the ionosphere despite that the meridional wind still acted to push up the ionosphere. During the last five days, the initial descent from midnight to about 1:00 LT was provided by ambipolar diffusion as before. After the initial descent, the electric field played a reduced role in pushing down the ions compared to the first interval. It was

the neutral wind that was drastically different from the first four days. Instead of acting to push up the ionosphere as in the first four days, it joined force with the electric field to push down the ions. The collapse of the ionosphere was more severe due to both electric field and neutral wind acting in concert to push down the ions.

Although the large downward velocity drove HmF2 to a very low altitude in the second interval, another important reason for the severe collapse lies in the initial high HmF2 before midnight. The more severe collapse during the latter period of Jan. 18-22 was much facilitated by the upward drift provided by the meridional wind before midnight. The upward lift primed the ionosphere to a higher altitude, giving more room for the ionosphere to fall. If the ionosphere were situated at a very low altitude, drastic downward ion motion would not change the HmF<sub>2</sub> appreciably (but would change the NmF2 significantly) because of larger chemical loss rate at lower altitudes.

From the above, we can summarize the process of midnight collapse into three stages. The first stage is preconditioning. The higher the ionosphere is prior to collapse, the more likely a severe collapse will occur. Neutral wind is most important for preconditioning during Jan. 18-22. The second stage is the initial descent. Ambipolar diffusion is most important during the initial descent because the ionosphere is typically high at the start of collapse. The third stage is the sustained descent. Electric field is the more consistent force for sustained descent during the entire period of Jan. 14-22. The most severe collapse, however, occurs when the meridional wind works in phase with electric field to push the ions downward.

### **5.3.2 Which tidal components are most important for midnight collapse?**

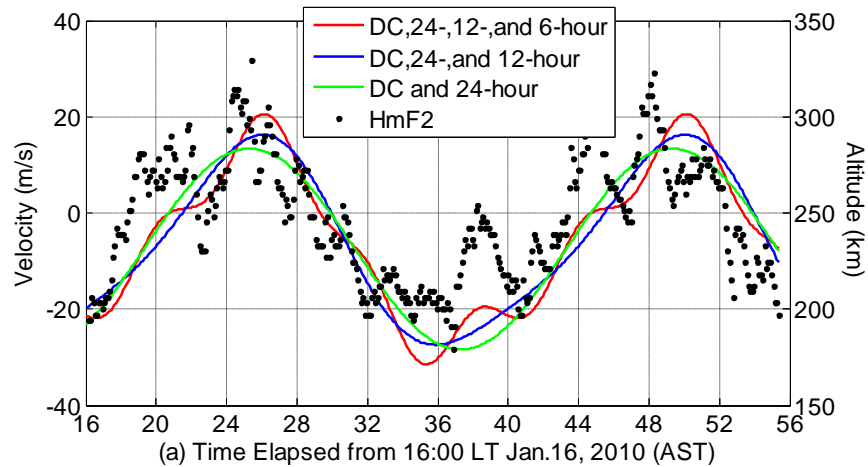
Previous studies [e.g., *Behnke and Harper, 1973; Macpherson et al., 1998; Vlasov et al., 2005*] have shown the reversal or the abatement of the meridional wind around midnight is the cause of the midnight collapse. *Harper [1979]* and *Crary and Forbes [1986]* further identified the semidiurnal tide as the most important component. To examine which tidal component is most important in our observation, we fit the meridional wind with the three strongest tidal components during the first four and last

five days. The amplitude and phase results at 268 km are summarized in Table 5.1. The strongest component is the diurnal tide while the semidiurnal tide is the weakest during both intervals. The most significant difference between the two periods lies in the terdiurnal and quad-diurnal tides.

**Table 5.1 Amplitude and phase results of 24-, 12-, and 6-hour components in the meridional wind during Jan. 14-18, 2010, and 24-, 12-, and 8-hour components during Jan. 18-23, 2010 at 268 km, respectively.**

	January 14-18, 2010		January 18-23, 2010	
	Amplitude (m/s)	Phase (LT)	Amplitude (m/s)	Phase (LT)
24-hour	41.7	1.3	45.3	1.1
12-hour	7.7	3.1	21.7	10.4
8-hour	-	-	33.1	6.7
6-hour	8.7	2.2	-	-

In Figure 5.6, we plot the reconstructed vertical ion drift induced by the meridional wind using various components and compare them with HmF2 for both intervals. We show only two nights so that the fine structures can be more easily seen.



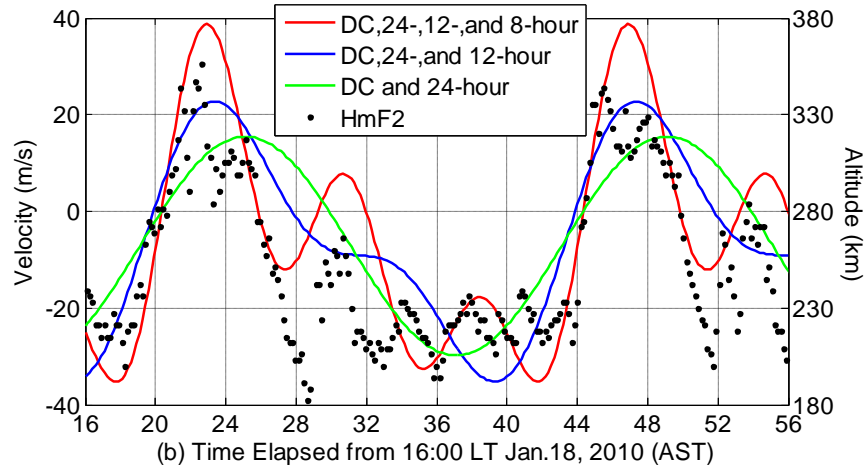


**Figure 5.6 (a) Constructed meridional winds at 268 km during 16:00 LT Jan. 16 to 07:23 LT Jan. 18, 2010, use dc, 24-, 12-, and 6-hour components shown in red curve, dc, 24-, and 12-hour components shown in blue curve, and dc and 24-hour components shown in green curve, respectively. HmF2 is represented by black dots. (b) Same as (a) except for the period of 16:00 LT Jan. 18 to 8:00 LT Jan. 20, 2010, and using 8-hour instead of 6-hour component.**

The diurnal tide, having the largest amplitude of all the tidal components, anchors the overall trend that the equatorward wind is maximized around midnight. The large amplitude and the phase of the diurnal tide determine that the ionosphere will likely be pushed high around midnight. This is the same for both intervals. Diurnal tide's preconditioning of the ionosphere is likely the most important reason for the frequent occurrence of nighttime collapses observed at Arecibo.

What accounts for the interval-to-interval variability and the quick drop in HmF2, however, are the higher-frequency tides. During the first four days, modification due to semidiurnal and quad-diurnal tides to the neutral wind has only a small effect. As a result, the wind pattern is largely dictated by the diurnal tide. Because of its long period, the diurnal tide can only slowly change the equatorward wind after midnight. During the second interval, both semidiurnal and terdiurnal tides are appreciable. Their phases are such that they act in concert with the diurnal tide to maximize the equatorward wind

around midnight. Terdiurnal tide drives the meridional wind pole-ward (ions downward) very quickly because of its short period. Although it is amazing to see that the three tidal components work in a “team-effort” to have the right structure to cause the severe collapse, terdiurnal tide is the most important reason for the difference between the first and second intervals. With the electric field relatively weak during the second interval, we see that the variation of HmF<sub>2</sub> correlates with the tidal wind very well during night. A detailed study on the terdiurnal tide for the Jan. 14-23 period can be found in *Gong and Zhou* [2011].

### 5.3.3 Considerations from other periods

During Jan. 18-22, 2010, we see that meridional wind is largest in the southward direction around midnight. It plays an essential role in lifting up the ionosphere before the collapse and helping to push down the ions during the collapse. Although similar neutral wind pattern is reported in several other studies [e.g., *Harpur*, 1979; *Crary and Forbes*, 1986], we caution the reader that such a wind pattern is not a prerequisite for midnight collapse. The vertical ion drift due to electric field can have a similar effect. The collapse during Jan. 14-17 was largely due to the effect of electric field although moderate preconditioning was mostly provided by the meridional wind.

In Figure 5.7, we plot HmF<sub>2</sub>, total vertical ion drift velocities at 293 km, and NmF<sub>2</sub> for Dec. 3-5, 2002 while component vertical velocities are plotted in Figure 5.8.

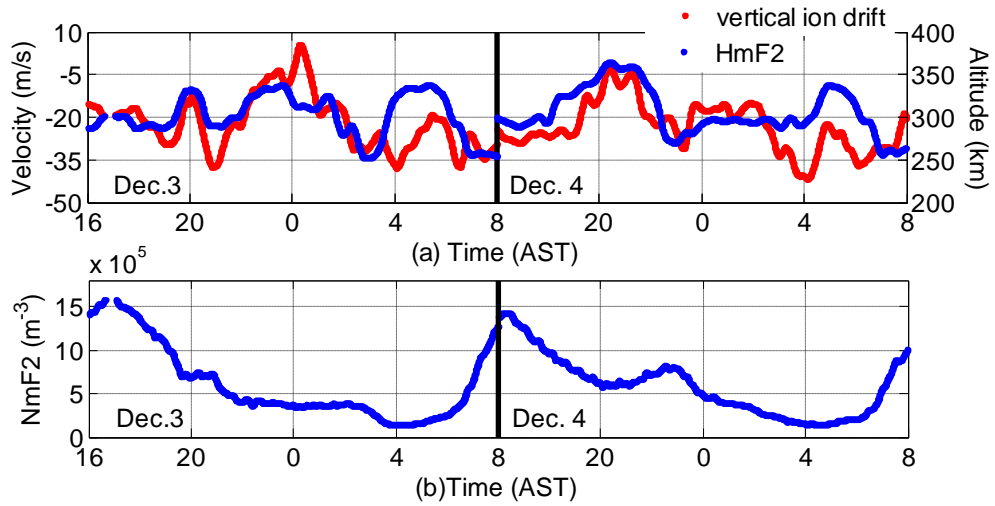


**Figure 5.7 (a)** Same as Figure 5.3 except for the period of 12:00 LT Dec. 3 to 12:00 LT Dec. 5, 2002, and vertical ion drift is at an altitude of 293 km. **(b)** NmF2 during 12:00 LT Dec. 3 to 12:00 LT Dec. 5, 2002.

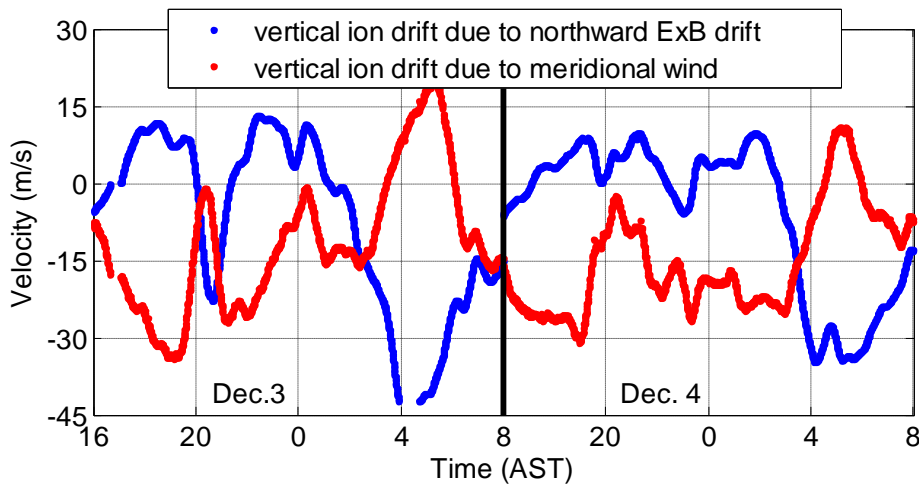


**Figure 5.8** Ion vertical drift contributed from perpendicular northward ion drift (blue dots), and meridional wind (red dots) at 293 km in the period of 12:00 LT Dec. 3 to 12:00 LT Dec. 5, 2002. In order to better examine the nighttime part, only a local time range from 20:00 LT to next day 8:00 LT are presented. Solid black lines are served as demarcation of different nights.

HmF<sub>2</sub> dropped from 320 km to 250 km from 1:30 to 3:00 LT on Dec. 3. On this night, it was the electric field that pushed the ionosphere to a high altitude prior to the collapse. The electric field switched direction at 1:30 LT and then pushed the ions downward at a speed of 20 m/s. Vertical drift due to the meridional wind was negative before the collapse, which made it a less important factor in preconditioning the ionosphere. It is interesting to see that after 3:00 LT, the electric field pushed the ions downward at a very fast speed while the neutral wind provided the upward lift to prevent the ionosphere from collapsing further. The anti-correlation phenomenon between  $V_{pn}$  and  $V_{ap}$ , reflected here as between  $V_{z_{pn}}$  and  $V_{z_{us}}$ , was first observed by *Behnke* [1970] and a discussion on this phenomenon is found in *Kelly* [2009].

We note that HmF<sub>2</sub> started to move upward at ~3:00 LT on Dec. 3 despite that the vertical ion drift was downward (caused by large electric field) with a rather large amplitude. This discrepancy between the physical motion of the ions and the apparent motion of HmF<sub>2</sub> is due to the larger chemical loss at lower altitude. At around 3:00 LT, the ions at HmF<sub>2</sub> were transported downward at a very fast rate such that its concentration became lower than that at higher altitudes in a short period of time. As a result, a new HmF<sub>2</sub> emerged at a higher altitude. When one studies the “ionospheric rise” [e.g., *Nelson and Cogger*, 1971], one needs to bear in mind that a “rise” is not necessarily due to the physical motion of the ions. It may just be a morphological change due to heavy chemical loss at lower altitudes. When this happens, NmF<sub>2</sub> decreases, as seen at about 3:00 LT in both Figure 5.7(b) and in Figure 5.4(b).

Another long-duration observation during the winter time occurred in Jan. 1993 and was reported by *Zhou and Sulzer* [1997b]. Although the downward velocities during the two Januaries are very similar from midnight to 4:00 LT, the drop in HmF<sub>2</sub> was merely 30 km in Jan. 1993 (Figure 6(a) of *Zhou and Sulzer*, 1997b). The small drop in Jan. 1993 was likely associated with the fact that vertical ion velocity was consistently very negative (~ -18 m/s) before midnight. Because of the constant negative velocity, the ionosphere did not get a chance to be uplifted for collapse to occur. Another night without a midnight collapse is Dec. 4, 2002 in Figure 5.7. Despite that the vertical ion drift was very negative after midnight to 4:00 LT, there was no drop in HmF<sub>2</sub>. The lack

of midnight collapse on this night was again associated with the fact that the ionosphere was not preconditioned high. Conversely, at 21:00 and 4:00 LT on Dec. 4, 2002, collapses happened because of preconditioning. Thus, we see that merely driving the ions downward at a large downward velocity or acceleration is not sufficient and preconditioning HmF<sub>2</sub> to a high altitude is essential for the occurrence of significant collapses.

## 5.4 Summary and Conclusion

Using the Arecibo dual-beam ISR techniques, we have obtained the electron concentration and line-of-sight velocities, and then deduced the F-region ion vector drifts and meridional wind for January 14-22, 2010. During the nine nights of observation, the first four nights (Jan 14-17) exhibited moderate collapse in HmF<sub>2</sub> and the last five nights (Jan. 18-22) showed consistently severe collapses. We have also examined the collapses during Dec. 3-4, 2002. The observations show, not surprisingly, that the change in HmF<sub>2</sub> is closely tied to the physical motion of the ions. All nighttime collapses were accompanied by large downward velocity acceleration. However, large downward velocity or acceleration does not necessarily generate collapses. HmF<sub>2</sub> need to be elevated first before the occurrence of moderate to severe collapses. In fact, HmF<sub>2</sub> can rise even when  $V_z$  is as negative as -15 m/s.

In general, the nighttime collapse can be considered to consist of three stages. The first stage is the preconditioning of the ionosphere to a high altitude. This can be accomplished by either the meridional wind and/or the electric field. The second stage is the initial descent which is dominated by ambipolar diffusion because of the relatively high HmF<sub>2</sub>. During this stage, the combined effect of neutral wind and electric field in pushing up the ions has started to diminish. The third stage is the sustained descent, during which the ions are forced downward by the neutral wind and/or the electric field. The most severe collapses, as during Jan. 18-22, 2010, occurred when electric field and neutral wind pushed the ions in the same direction, upward for preconditioning, downward during the sustained descent stage. Moderate collapses, as during Jan. 14-17,

2010, occurred when one mechanism dominated the opposing effect of the other mechanism. Our analysis here thus suggests that neutral wind, electric field, and ambipolar diffusion all play a role in contributing to the nighttime ionosphere collapse while previous studies only regarded neutral wind as the cause.

Tidal analysis of the meridional wind shows that diurnal tide is the most dominant and consistent tidal modes during January 14-22, 2010. The phase of the diurnal tide was such that the maximum equatorward wind occurs shortly after midnight. The semidiurnal and terdiurnal tides showed large interval-to-interval variability. During Jan. 18-22, 2010, both terdiurnal and semidiurnal tides were appreciable with the amplitude of the former somewhat bigger than the latter. Perhaps more important for midnight collapse, the wind directions of both terdiurnal and semidiurnal around midnight were largely the same as the diurnal tide. The phase alignment of the three tidal components around midnight maximized the effect of the meridional wind for preconditioning. Because of its shorter period, the terdiurnal tide was most effective in causing the rapid drop in  $HmF_2$  during collapse.

# CHAPTER 6

## CONCLUSIONS AND FUTURE STUDIES

### 6.1 Conclusions

This thesis primarily presents studies on two related topics of atmospheric dynamics and ionospheric physics. One is a study of tidal and quasi-2 day planetary waves in an altitude range from 90 km to 350 km above Arecibo during January 14-23, 2010. The second one is an investigation of a prominent phenomenon observed above Arecibo during Jan. 14-22 in 2010, i.e., midnight collapse, a rapid drop of the F-layer peak height around midnight. The data used in this thesis is based on two periods of observations made by the Arecibo incoherent scatter radar during January 14-23, 2010, and December 3-5, 2002.

The nine days of data from Jan. 14-23, 2010 are broken into two sub-periods, first four days (Jan. 14-18) and last five days (Jan. 18-23). For each sub-period, based on the periodogram, harmonic fitting is applied to extract strong tidal components. In order to investigate the short term variability of tidal components, each sub-period is divided into 2 or 3 sub-intervals. One of the most distinctive findings is that contrary to previous studies [*Harper* 1979, 1981], the diurnal tide dominates the semidiurnal tide as the most important tidal component above 110 km. In the F-region, the peak amplitude of diurnal tide is 45 m/s, and in the E-region that value is 70 m/s at around 120 km. Compared with the diurnal tide, semidiurnal tide is much smaller in the F-region. The peak amplitudes of semidiurnal tide for F- and E-region are 22 m/s, and 62 m/s, respectively. In the F-region, the diurnal tide is very prominent and stable throughout the nine day observation, while the semidiurnal tide is strong in the second sub-period but weak in the first sub-period. The diurnal tide is largely evanescent, which suggests it may be excited by in situ solar radiation [*Hagan et al.*, 2001]. In the E-region, diurnal tide in the meridional wind is very strong and consistent between two sub-periods. The vertical wavelength is estimated as 63 km for the second sub-period in the altitude range from 114 km to 135 km. Below 114 km, the vertical wavelengths are computed to be 24 km and 20 km for two the respective

sub-periods. Diurnal tide in the zonal wind is less prominent than it is in the meridional wind. The interval-to-interval variation is very large above 120 km for both sub-periods. Due to large variation, vertical wavelength can only be estimated in the second sub-period as 18 km below an altitude of 120 km. The semidiurnal tides in both meridional and zonal components are observed as substantial only in the first sub-period. The semidiurnal tides in both components show continuous amplitude increase in the altitude range from 106 km to 115 km. This amplitude behavior is helpful in determining that the turbopause at Arecibo in winter condition is around 110 km. This conclusion is further supported by an earlier observation [Zhou *et al.*, 1997a]. The vertical wavelengths for the meridional component are computed as 68 km above 112 km, and 12 km below this altitude. For the zonal component, the vertical wavelength is estimated to be 45 km above 100 km. Since the amplitudes are significantly reduced in the second sub-period for both components, the vertical wavelengths are difficult to determine.

Since this is the first time a terdiurnal tide has been observed in the F-region at a low latitude station, much effort is devoted to discuss the terdiurnal tide. The terdiurnal tide is observed to be prominent at E-region heights in the first four days and at the F-region heights in the last five days. The terdiurnal tide is among the two strongest tidal components in both regions. The vertical wavelength of the terdiurnal tide in the meridional wind is about 74 km, and 950 km, for the altitude range of 121 km to 135 km, and 180 km to 320 km, respectively. For the zonal component, the vertical wavelength is around 128 km for the altitude range of 92 km to 105 km, and around 100 km for the altitude range of 112 km to 127 km during the first four days. In the period of the last five days, the vertical wavelength is about 81 km above 95 km. The F-region terdiurnal tide amplitude is found to be well correlated with the background meridional wind in the lower F-region. Our analysis does not reveal any evidence that non-linear interaction between diurnal and semidiurnal tides is important for the F-region terdiurnal tide.

Although this is also the first time 6-hour tide and quasi-2 day planetary wave have been reported in the F-region at low latitude, unlike the terdiurnal tide, the amplitude of 6-hour tide and quasi-2 day planetary are much weaker. The amplitude of 6-hour tide exhibits two peaks and the peak magnitude is about 11 m/s for both peaks. The

6-hour tidal phase is very consistent. Above 245 km, the phase is largely constant, and below that altitude, the phase progresses downward linearly with a vertical wavelength determined to be 126 km. For the quasi-2 day planetary, the peak amplitude is about 8 m/s. The vertical wavelength is computed to be 640 km in the altitude range from 230 km to 305 km.

The “midnight collapse”, a large drop in the F-layer peak height (HmF2) around midnight, was observed at Arecibo during Jan. 14-22, 2010. During the nine nights of observations, the first four nights (Jan. 14-17) exhibited modest drops in HmF2 while the last five nights (Jan. 18-22) showed more severe drops. We examined the roles played by the neutral wind, electric field, and ambipolar diffusion in driving the vertical ion motion. The collapse process can be classified into three stages: preconditioning, initial descent, and sustained descent. Severe collapses occur when HmF2 is preconditioned high prior to the collapse. Ambipolar diffusion is most important during the initial descent. Neutral wind and electric field are responsible to sustain the collapse. During Jan. 18-22, HmF2 was pushed high by the neutral wind before the collapse started. The neutral wind and electric field were in phase during the sustained severe collapse. The diurnal tide of the meridional wind provided the general condition for the collapses. The terdiurnal tide was the most important factor in the difference between the two sub-periods in our observation. Previous studies largely emphasized meridional wind being the dominant mechanism causing midnight collapse. Our study suggests that electric field and ambipolar diffusion also play an important role with the former being the most dominant factor in some cases.

## **6.2 Future Studies**

The observational data used in this thesis is merely derived from a single station located at low latitude, Arecibo Observatory, Puerto Rico (18.3 N, 66.7 W), using a single instrument, incoherent scatter radar, during two winter periods, January 14-23, 2010, and December 3-5, 2002, respectively. The features of tidal and quasi-2 day planetary waves reported in this thesis are only confined at low latitude in winter time.

The investigation results of Arecibo midnight collapse are limited in winter season. Therefore, in order to overcome the limitations of current study, some directions of future research that can be pursued include:

1. Studying seasonal differences of tidal and planetary waves by using the Arecibo ISR data from all four seasons.
2. Investigating latitudinal differences of tidal and planetary waves by using observational data obtained from ISR facilities located at other latitudes, such as Millstone Hill Observatory (42.6° N) and the Sondrestrom Research Facilities (67° N).
3. Using satellite techniques to analyze tidal waves from a global perspective. Migrating and non-migrating tides can be resolved from satellite data, because the information of longitudinal distribution is available.
4. Examining seasonal differences of Arecibo midnight collapse. Investigating the roles of neutral wind, electric field, and ambipolar diffusion played in the other seasons.

## BIBLIOGRAPHY

- Amayenc, P. (1974), Tidal oscillations of the meridional neutral wind at midlatitudes, *Radio Sci.*, 9, 281-293.
- Aponte, N., M. J. Nicolls, S. A. Gonzalez, M. P. Sulzer, M. C. Kelley, E. Robles, and C. A. Tepley (2005), Instantaneous electric field measurements and derived neutral winds at Arecibo, *Geophys. Res. Lett.*, 32, L12107.
- Bauer, P., K. D. Cole, and G. Lejeune (1976), Field aligned electric currents and their measurement by the incoherent backscatter technique, *Planet. Space Sci.*, 24(5), 479–485.
- Bekefi, G. (1966), *Radiation Processes In Plasmas*, New York: Wiley, Chap 8.
- Behnke, R., A. (1970), Vector measurements of the ion transport velocity with application to the F-region dynamics, *Ph.D thesis*, Rice University, Houston, TX.
- Behnke, R. A., and S. Ganguly (1986), First direct ground-based measurements of electron drift in the ionospheric F region, *J. Geophys. Res.*, 91(A9), 10,178– 10,182.
- Behnke, R. A., and R. M. Harper (1973), Vector measurements of F region ion transport at Arecibo, *J. Geophys. Res.*, 78, 8222.
- Breit, G., and M. Tuve (1925), A radio method for estimating the height of the ionosphere conducting layer, *Nature*, vol. 116, p. 357.
- Breit, G., and M. Tuve (1926), A test of the existence of the conducting layer, *Phys. Rev.*, vol. 28, pp. 554-573.
- Bowles, K. L. (1958), Observations of vertical incidence scatter from the ionosphere at 41 Mc/s, *Phys. Rev. Letters*, 1, 454.
- Buneman O. (1962), Scattering of radiation by the fluctuations in a nonequilibrium plasma, *J. Geophys. Res.*, 67, 2050-2053.

- Buonsanto, M. J., and O. G. Witasse (1999), An updated climatology of thermospheric neutral winds and F region ion drifts above Millstone Hill, *J. Geophys. Res.*, 104, 24,675–24,687.
- Canziani, P. O., J. R. Holton, E. F. Fishbein, L. Froidevaux, and J. W. Waters (1994), Equatorial Kelvin waves: A UARS MLS view, *J. Atmos. Sci.*, 51, 3053–3076.
- Carter, L. N. and J. M. Forbes (1999), Global transport and localized layering of metallic ions in the upper atmosphere, *Ann. Geophys.*, 17, 190–209.
- Chapman, S., and R. S. Lindzen (1970), *Atmospheric Tides*, 201 pp., D. Reidel, Norwell, Mass.
- Chshyolkova, T., A. H. Manson, and C. E. Meek (2005), Climatology of the quasi two - day wave over Saskatoon (52 °N, 107 °W): 14 years of MF radar observations, *Adv. Space Res.*, 35, 2011 – 2016, doi:10.1016/j.asr.2005.03.040.
- Colerico, M. J., M. Mendillo, D. Nottingham, J. Baumgardner, J. Meriwether, J. Mirick, B.W. Reinisch, J. L. Scali, C. G. Fesen, and M. A. Biondi (1996), Coordinated measurements of F region dynamic related to the thermospheric midnight temperature maximum, *J. Geophys. Res.*, 101, 26,783–26,793, doi:10.1029/96JA02337.
- Crary, D. J., and J. M. Forbes (1986), The dynamic ionosphere over Arecibo: A theoretical investigation, *J. Geophys. Res.*, 91, 249–258.
- Deepa V, G. Ramkumar, T. M. Antonia, and K. K. Kumar (2008), Meteor wind radar observations of tidal amplitudes over a low-latitude station Trivandrum (8.51 °N, 77 °E): Interannual variability and the effect of background wind on diurnal tidal amplitudes. *J. Atmos. Solar-Terr. Phys.*, 70, 2005–2013.
- Du, J. and W. E. Ward (2010), Terdiurnal tide in the extended Canadian Middle Atmospheric Model (CMAM), *J. Geophys. Res.*, 115, D24106, doi:10.1029/2010JD014479.
- Dungey, J. W. (1956), The influence of the geomagnetic field on turbulence in the ionosphere, *J. Atmos. and Terr. Phys.*, 8, 39-42.

- Farley, D. T. (1966), A theory of incoherent scattering of radio waves by a plasma, 4, the effect of unequal ion and electron temperatures, *J. Geophys. Res.*, 71, 4091.
- Forbes, J. M. (1982a), Atmospheric tides, I, Model description and results for the solar diurnal component, *J. Geophys. Res.*, 87, 5222-5240.
- Forbes, J. M. (1982b), Atmospheric tides, II, Solar and lunar semidiurnal components, *J. Geophys. Res.*, 87, 5241-5252.
- Forbes, J. M. (1995), Tidal and planetary waves, in *The Upper Mesosphere and Lower Thermosphere: A Review of Experiment and Theory*, *Geophys. Monogr. Ser.*, vol. 87, edited by R. M. Johnson and T. L. Killeen, pp. 67 - 87, AGU, Washington, D. C.
- Forbes, J. M., X. Zhang, S. Palo, J. Russell, C. J. Mertens, and M. Mlynczak (2008), Tidal variability in the ionospheric dynamo region, *J. Geophys. Res.*, 113, A02310, doi:10.1029/2007JA012737.
- Garcia, R. R., R. Lieberman, J. M. Russell, and K. G. Mlynczak (2005), Large-Scale Waves in the Mesosphere and Lower Thermosphere Observed by SABER, *J. Atmos. Sci.*, 62, 4384-4399.
- Gong, Y., and Q. Zhou (2011), Incoherent scatter radar study of the terdiurnal tide in the E- and F-region heights at Arecibo, *Geophys. Res. Lett.*, 38, L15101, doi:10.1029/2011GL048318.
- Gordon, W. E. (1958), Incoherent scattering of radio waves by free electrons with applications to space exploration by radar, *Proc. IRE*, 46, 1824.
- Hagan, M. E., and J. M. Forbes (2002), Migrating and nonmigrating tides in the middle and upper atmosphere excited by tropospheric latent heat release, *J. Geophys. Res.*, 107(D24), 4754, doi:10.1029/2001JD001236.
- Hagan, M. E., J. M. Forbes, and F. Vial (1995), On modeling migrating solar tides, *Geophys. Res. Lett.*, 22, 893-896.

- Hagan, M. E., and R. G. Roble (2001), Modeling diurnal tidal variability with the National Center for Atmospheric Research thermosphere-ionosphere - mesosphere electrodynamics general circulation model, *J. Geophys. Res.*, 106(A11), 24,869 – 24,882.
- Hagan, M. E., R. G. Roble, and J. Hackney (2001), Migrating thermospheric tides, *J. Geophys. Res.*, 106, A7, 12,739-12,752.
- Hagfors, T., and R. A. Behnke (1974), Measurements of three-dimensional plasma velocities at the Arecibo Observatory, *Radio Sci.*, 9, 89– 93.
- Hagfors, T., and M. Lehtinen (1981), Electron temperature derived from incoherent scatter radar observation of the plasma line frequency, *J. Geophys. Res.*, 86(A1), 119– 124.
- Haldoupis, C., D. Pancheva, and N. J. Mitchell (2004), A study of tidal and planetary wave periodicities present in midlatitude sporadic E layers, *J. Geophys. Res.*, 109, A02302, doi:10.1029/2003JA010253.
- Harper, R. M. (1977), Tidal winds in the 100- to 200-km region at Arecibo, *J. Geophys. Res.*, 84, 22, 3243–3248.
- Harper, R. M. (1979), A semidiurnal tide in the meridional wind at F region heights at low latitudes, *J. Geophys. Res.*, 84, (A2), 411–415.
- Harper, R. M. (1981), Some results on mean tidal structure and day-to-day variability over Arecibo, *J. Atmos. Terr. Phys.*, 43, 255-262.
- Harper, R. M., R. H. Wand, C. J. Zamlutti, and D. T. Farley (1976), E region ion drifts and winds from incoherent scatter measurements at Arecibo, *J. Geophys. Res.*, 81, 25- 35.
- Hirota, I. (1978), Equatorial waves in the upper stratosphere and mesosphere in relation to the semiannual oscillation of the zonal wind, *J. Atmos. Sci.*, 35, 714–722.

- Hocke, K. (1996), Tidal variations in the high-latitude E- and F-region observed by EISCAT, *Ann. Geophys.*, 14, 201-210.
- Huang, C. M., S. D. Zhang, and F. Yi (2007), A numerical study on amplitude characteristics of the terdiurnal tide excited by nonlinear interaction between the diurnal and semidiurnal tides, *Earth Planets Space*, 59, 183–191.
- Huang, F. T., and C. A. Reber (2003), Seasonal behavior of the semidiurnal and diurnal tides, and mean flows at 95 km, based on measurements from the High Resolution Doppler Imager (HRDI) on the Upper Atmosphere Research Satellite (UARS), *J. Geophys. Res.*, 108(D12), 4360.
- Iimura, H., D. C. Fritts, Q. Wu, W. R. Skinner, and S. E. Palo (2010), Nonmigrating semidiurnal tide over the Arctic determined from TIMED Doppler Interferometer wind observations, *J. Geophys. Res.*, 115, D06109.
- Ioannidis, G., and D. T. Farley (1972), Incoherent scatter observations at Arecibo using compressed pulses, *Radio Sci.*, 7, 766.
- Isham, B., C. A. Tepley, M. P. Sulzer, Q. H. Zhou, M. C. Kelley, J. S. Friedman, and S. A. Gonzalez (2000), Upper atmospheric observations at the Arecibo Observatory: Examples obtained using new capabilities, *J. Geophys. Res.*, 105, 18,609-18,637, doi:10.1029/1999JA900315.
- Kelley, M. C. (2009), *The Earth's Ionosphere: Plasma Physics and Electrodynamics*, 2nd edition, Elsevier, London.
- Kovalam, S., and R. A. Vincent (2003), Intradiurnal wind variations in the midlatitude and high-latitude mesosphere and lower thermosphere, *J. Geophys. Res.*, 108(D4), 4135, doi:10.1029/2002JD002500.
- Lau, E. M., S. K. Avery, J. P. Avery, S. E. Palo, and N. A. Makarov (2006), Tidal analysis of meridional winds at the South Pole using a VHF interferometric meteor radar, *J. Geophys. Res.*, 111, D16108, doi:10.1029/2005JD006734.

- Li, T., C. Y. She, H.-L. Liu, J. Yue, T. Nakamura, D. A. Krueger, Q. Wu, X. Dou, and S. Wang (2009), Observation of local tidal variability and instability, along with dissipation of diurnal tidal harmonics in the mesopause region over Fort Collins, Colorado (41<sup>0</sup>N, 105<sup>0</sup>W), *J. Geophys. Res.*, 114, D06106, doi:10.1029/2008JD011089.
- Lomb, N. R. (1976), Least-square frequency analysis of unequally spaced data, *Astrophys. Space. Sci.*, 39, 447-662.
- Lu, X., A. Z. Liu, J. Oberheide, Q. Wu, T. Li, Z. Li, G. R. Swenson, and S. J. Franke (2011), Seasonal variability of the diurnal tide in the mesosphere and lower thermosphere over Maui, Hawaii (20.7 °N, 156.3 °W), *J. Geophys. Res.*, 116, D17103, doi:10.1029/2011JD015599.
- Macleod, M. A. (1965), Sporadic E theory. I. Collision-Geomagnetic Equilibrium, *J. Atmo. Sci.*, 23, 96.
- Macpherson, B., S. A. Gonzalez, G. J. Bailey, R. J. Moffett, and M. P. Sulzer (1998), The effects of meridional neutral winds on the O<sup>+</sup>-H<sup>+</sup> transition altitude over Arecibo, *J. Geophys. Res.*, 103, 29,183–29,198.
- Mathews, J. D. (1976), Measurements of diurnal tides in the 80- to 100- km altitude range at Arecibo, *J. Geophys. Res.*, 81, 4671.
- Mathews, J. D. (1986), Incoherent scatter radar probing of the 60-100 km atmosphere and ionosphere, *IEEE Trans. Geoscience Remote Sensing*, GE-24, 765.
- Mathews, J. D. (1998), Sporadic E: current views and recent progress, *Journal of Atmospheric and Solar-Terrestrial Physics*, 60, 413-435.
- Mathews, J. D. and F. S. Bekey (1979), Upper atmosphere tides and the vertical motion ionospheric sporadic layers at Arecibo, *J. Geophys. Res.*, 84, 2743.
- Miyahara, S., and J. M. Forbes (1991), Interactions between gravity waves and the diurnal tide in the mesosphere and lower thermosphere, *J. Meteorol. Soc. Jpn.*, 69, 523–531.

- Morton, Y. T., J. D. Mathews, and Q. Zhou (1993), Further evidence for a 6-h tide above Arecibo, *J. Atmos. Terr. Phys.*, 55, 459-465.
- Nelson, G. J., and L. L. Cogger (1971), Dynamical behavior of the nighttime ionosphere at Arecibo, *J. Atmos. Terr. Phys.*, 33, 1711.
- Nicolls, M. J., M. P. Sulzer, N. Aponte, and S. A. González (2006), High resolution electron temperature measurements using the plasma line asymmetry, *Geophys. Res. Lett.*, 33, L18107, doi:10.1029/2006GL027222.
- Philbrick, C. R., R. S. Narcisi, R. E. Good, H. S. Hoffman, T. J. Keneshea, M. A. Macleod, S. P. Zimmerman and B. W. Reinisch (1973), The ALADDIN experiment – Part II, composition, *Space Research XIII*, 89.
- Press, W. H., S. A. Teukolsky, W. T. Vetterling, and B. P. Flannery (1992), *Numerical Recipes*, Cambridge Univ. Press, New York.
- Richards, M. A. (2005), *Fundamentals of Radar Signal Processing*, McGraw-Hill.
- Scargle, J. D. (1982), Studies in astronomical time series analysis, II, Statistical aspects of spectral analysis of unevenly spaced data, *Astrophys. J.*, 263, 835-853.
- Salby, M. L. (1981a), Rossby normal modes in nonuniform background configuration, I, Simple field, *J. Atmos. Sci.*, 38, 1803-1826.
- Salby, M. L. (1981b), Rossby normal modes in nonuniform background configurations, II, Equinox and solstice conditions, *J. Atmos. Sci.*, 38, 1827-1840.
- Salby, M. L. (1984), Survey of planetary - scale travelling waves: The state of theory and observations, *Rev. Geophys.*, 22, 209 - 236, doi:10.1029/RG022i002p00209.
- Schunk, R. W., and A. F. Nagy (2000), *Ionospheres Physics, Plasma Physics, and Chemistry*, Cambridge Univ. Press, New York.
- Seker, I., D. J. Livneh, and J. D. Mathews (2009), A 3-D empirical model of F region Medium-Scale Travelling Ionospheric Disturbance bands using incoherent scatter

- radar and all-sky imaging at Arecibo, *J. Geophys. Res.*, 114, A06302, doi:10.1029/2008JA014019.
- She, C. Y., S. Chen, B. P. Williams, Z. Hu, D. A. Krueger, and M. A. Hagan (2002), Tides in the mesopause region over Fort Collins, Colorado (41<sup>0</sup>N, 105<sup>0</sup>W) based on lidar temperature observations covering full diurnal cycles, *J. Geophys. Res.*, 107(D18), 4350, doi:10.1029/2001JD001189.
- She, C. Y., et al. (2004), Tidal perturbations and variability in mesopause region over Fort Collins, CO (41N, 105W): Continuous multi-day temperature and wind lidar observations, *Geophys. Res. Lett.*, 31, L24111, doi:10.1029/2004GL021165.
- Sherman, J. P., and C. Y. She (2006), Seasonal variation of mesopause region wind shears, convective and dynamic instabilities above Fort Collins, CO: A statistical study, *J. Atmos. Sol. Terr. Phys.*, 68, 1061– 1074, doi:10.1016/j.jastp.2006.01.011.
- Showen, R. L. (1979), The spectral measurement of plasma lines, *Radio Sci.*, 14(3), 503– 508.
- Sivjee, G. G., and R. L. Walterscheid (1994), Six-hour zonally symmetric tidal oscillations of the winter mesopause over the South Pole station, *Planet. Space Sci.*, 42, 447– 453.
- Smith, A. K. (2000), Structure of the terdiurnal tide at 95 km, *Geophys. Res. Lett.*, 27(2), 177– 180.
- Smith, A. K., and D. A. Ortland (2001), Modeling and Analysis of the Structure and Generation of the Terdiurnal Tide, *J. Atmos. Sci.*, 58, 3116-3134.
- Smith, A. K., D. V. Pancheva, and N. J. Mitchell (2004), Observations and modeling of the 6-hour tide in the upper mesosphere, *J. Geophys. Res.*, 109, D10105, doi:10.1029/2003JD004421.
- Suresh Babu, V., K. Kishore Kumar, S. R. John, K. V. Subrahmanyam, and G. Ramkumar (2011), Meteor radar observations of short - term variability of quasi 2 day waves and their interaction with tides and planetary waves in the mesosphere-lower

- thermosphere region over Thumba (8.5°N, 77°E), *J. Geophys. Res.*, 116, D16121, doi:10.1029/2010JD015390.
- Sulzer, M. P. (1986), A radar technique for high range resolution incoherent scatter autocorrelation function measurements utilizing the full average power of klystron radars, *Radio Sci.*, 21, 1033–1040.
- Sulzer, M. P. (1988), Aeronomy data-taking programs at Arecibo Observatory.
- Sulzer, M. P., N. Aponte, and S. A. Gonzalez (2005), Application of linear regularization methods to Arecibo vector velocities, *J. Geophys. Res.*, 110, A10305, doi:10.1029/2005JA011042.
- Teitelbaum, H., F. Vial, A. H. Manson, R. Giraldez, and M. Massebeuf (1989), Nonlinear interaction between the diurnal and semidiurnal tides: Terdiurnal and diurnal secondary waves, *J. Atmos. Terr. Phys.*, 51, 627–634.
- Thayaparan, T., and W. K. Hocking (2002), A long-term comparison of winds and tides measured at London, Canada (43°N, 81°W) by co-located MF and meteor radars during 1994 – 1999, *J. Atmos. Terr. Phys.*, 64, 931–946.
- Tong Y., J. D. Mathews, and W. P. Ying (1988), An upper E region quarter diurnal tide at Arecibo?, *J. Geophys. Res.*, 93, 10047-10051.
- Vasseur, G. (1972), Dynamics of the F-region observed with Thompson Scatter, 1, Atmospheric circulation and neutral winds, *J. Atmos. Terr. Phys.*, 20, 353.
- Venkateswara Rao, N., T. Tsuda, S. Gurubaran, Y. Miyoshi, and H. Fujiwara (2011), On the occurrence and variability of the terdiurnal tide in the equatorial mesosphere and lower thermosphere and a comparison with the Kyushu-GCM, *J. Geophys. Res.*, 116, D02117, doi:10.1029/2010JD014529.
- Vlasov, M. N., M. J. Nicolls, M. C. Kelley, S. M. Smith, N. Aponte, and S. A. Gonzalez (2005), Modelling of airglow and ionospheric parameters at Arecibo during quiet and disturbed periods in October 2002, *J. Geophys. Res.*, 110, A07303, doi:10.1029/2005JA011074.

- Walterscheid, R. L., and G. G. Sivjee (1996), Very high frequency tides observed in the airglow over Eureka (80 °), *Geophys. Res. Lett.*, 23, 3651–3654.
- Walterscheid, R. L., and G. G. Sivjee (2001), Zonally symmetric oscillations observed in the airglow from South Pole station, *J. Geophys. Res.*, 106, 3645–3654.
- Whitehead, J. D. (1961), The formation of the Sporadic E layer in the temperate zones, *J. Atmos and Terr. Phys.*, 20, 49.
- Woodman, R. F., Vertical drifts and east-west electric fields at the magnetic equator, *J. Geophys. Res.*, 75, 6249, 1970.
- Wu, Q., D. A. Ortland, T. L. Killeen, R. G. Roble, M. E. Hagan, H.-L. Liu, S. C. Solomon, J. Xu, W. R. Skinner, and R. J. Niciejewski (2008a), Global distribution and interannual variations of mesospheric and lower thermospheric neutral wind diurnal tide: 1. Migrating tide, *J. Geophys. Res.*, 113, A05308, doi:10.1029/2007JA012542.
- Wu, Q., et al. (2008a), Global distribution and interannual variations of mesospheric and lower thermospheric neutral wind diurnal tide: 1. Migrating tide, *J. Geophys. Res.*, 113, A05308, doi:10.1029/2007JA012542.
- Wu, Q., D. A. Ortland, T. L. Killeen, R. G. Roble, M. E. Hagan, H.-L. Liu, S. C. Solomon, J. Xu, W. R. Skinner, and R. J. Niciejewski (2008b), Global distribution and interannual variations of mesospheric and lower thermospheric neutral wind diurnal tide: 2. Nonmigrating tide, *J. Geophys. Res.*, 113, A05309, doi:10.1029/2007JA012543.
- Xu, J., A. K. Smith, H. - L. Liu, W. Yuan, Q. Wu, G. Jiang, M. G. Mlynczak, J. M. Russell, and S. J. Franke (2009), Seasonal and quasi - biennial variations in the migrating diurnal tide observed by Thermosphere, Ionosphere, Mesosphere, Energetics and Dynamics (TIMED), *J. Geophys. Res.*, 114, D13107, doi:10.1029/2008JD011298.

- Yngvesson, K. O., and F. W. Perkins (1968), Radar Thomson scatter studies of photoelectrons in the ionosphere and Landau damping, *J. Geophys. Res.*, 73(1), 97–110.
- Zhao, G., L. Liu, B. Ning, W. Wan, and J. Xiong (2005), The terdiurnal tide in the mesosphere and lower thermosphere over Wuhan (30°N, 114°E), *Earth Planets Space*, 57, 393–398.
- Zhou, Q. H. (1991), A joint study of the lower ionosphere by radar, lidar, and spectrometer, *Ph.D. thesis*, The Pennsylvania State University, Department of Electrical and Computer Engineering.
- Zhou, Q. H., M. P. Sulzer, and C. A. Tepley (1997a), An analysis of tidal and planetary waves in the neutral winds and temperature observed at low-latitude E region heights, *J. Geophys. Res.*, 102, 11491-11505.
- Zhou, Q. H., M. P. Sulzer, C. A. Tepley, C. G. Fesen, R. G. Robie, and M. C. Kelley (1997b), Neutral winds and temperature in the tropical mesosphere and lower thermosphere during January 1993: Observation and comparison with TIME-GCM results, *J. Geophys. Res.*, 102, 11,507-11,519.
- Zhou Q. H., and M. P. Sulzer (1997c), Incoherent scatter radar observations of the F-region ionosphere at Arecibo during January 1993, *J. Atmo. Solar-Terr. Phys.*, 59, 2213-2229.
- Zhou, Q. H., J. Friedman, S. Raizada, C., Tepley, and Y. T. Morton (2005), Morphology of nighttime ion, potassium and sodium layers in the meteor zone above Arecibo, *J. Atmos. Solar-Terr. Phys.*, 67, 1245, doi:10.1016/j.jastp.2005.06.013.
- Zhou, Q. H., S. Raizada, C. Tepley, and J. Plane (2008), Seasonal and diurnal variation of electron and iron densities at the meteor heights above Arecibo, *J. Atmos. Solar-Terr. Phys.*, 70, 49, doi:10.1016/j.jastp.2007.09.012.

Zhou, Q. H., Y. T. Morton, C. M. Huang, N. Aponte, M. Sulzer, and S. Gonza'lez (2011),  
Incoherent scatter radar observation of E-region vertical electric field at Arecibo,  
*Geophys. Res. Lett.*, 38, L01101, doi:10.1029/2010GL045549.